AN ABSTRACT OF THE THESIS OF

Robert G. Friedel for the degree of Master of Science in Geography presented on December 1, 2006
Title: A Mathematical Transformation of Multi-angular Remote Sensing Data for the Study of Vegetation Change

Abstract approved:

_____

Anne W. Nolin

Vegetation change is an important factor affecting the global carbon cycle, land-atmosphere interaction, and terrestrial ecology. The study of vegetation change on a global scale can be used to evaluate the impact of global climate change on terrestrial ecosystems. Satellite remote sensing can monitor vegetation change at the global scale, providing continuous samples of radiation reflected by vegetated surfaces with a temporal resolution of days. The MISR instrument offers the potential to sample the specular anisotropy of the Earth from up to 9 angles. Characterization of the specular anisotropy of vegetated surfaces on a global scale will provide information on the physical characteristics of vegetation affecting anisotropy not available from nadir-view only remote sensing.

The objective of this study is to develop a Principal Components Analysis (PCA) transformation of multi-angular measurements of the Earth's surface acquired by the MISR instrument, to examine the feasibility of quantifying the structural characteristics of different vegetation communities at a global scale. This transformation will be applied to a time-series analysis of the Kalmioposis Wilderness in the Siskiyou National Forest in Southwestern Oregon to better understand the changes in spectral and angular reflectance of a forest stand during re-growth after a stand-replacing disturbance.

A sample encompassing a full phenologic cycle, of the red bands only from MISR cameras Ca – Cf, at scaled surface reflectance, provided the template on which PCA was performed. The sample of MISR data was created using imagery collected from 2001 – 2005 to provide a wide variety of vegetation and soils reflectance over a

phenologic cycle. Sample data was rotated to the principal components as the new axes using the coefficients of rotation from an un-standardized PCA. Samples were evaluated at various latitudes, differing topography, and varying vegetation density and land cover to determine the properties of the scene controlling the range and magnitude of the principal components. Principal component 1 was found to have high negative correlation to NDVI. Principal component 2 was found to have high positive correlation to both the solar zenith angle and the relative azimuth angle between the MISR sensor and the path of incident radiation. Principal component 3 could not be correlated to any available metric, although evidence suggests that component 3 may carry useful information.

The PCA transformation proved useful at relating the changes in vegetation after a fire at the Biscuit Complex. The changes in the BRDF as sampled by MISR were expressed through the principal components, but these changes could not be directly related to changing structural characteristics of the vegetation. The goal of assessing structural characteristics of vegetation through the PCA transformation to a single metric of vegetation structure was unsuccessful.

The PCA transformation of the MISR sample successfully yielded a transformation where different classes of vegetation occupied distinct and unique regions of PCA space. The first two principal components were successfully correlated to measurable and definable metrics of vegetation and solar illumination. The third principal component, for which a correlation could not be found, was suggestive of carrying unique information and merits further investigation.

The transformation of multi-angular red band reflectance as presented in this study may prove to be a valuable method of estimating biomass at a global scale. With principal components correlated to measures of biomass in NDVI and to the shadowing of the ground through the angle of solar illumination, the PCA relates characteristics of vegetated scenes in a minimum of bands.

A Mathematical Transformation of Multi-angular Remote Sensing Data for the Study of Vegetation Change

by
Robert G. Friedel

A THESIS

submitted to

Oregon State University

in partial fulfillment of
the requirements for the
degree of

Master of Science

Presented December 1, 2006
Commencement June 2007

Master of Science thesis of Robert G. Friedel presented on December 1, 2006

APPROVED:

Major Professor, representing Geography

Chair of the Department of Geosciences

Dean of the Graduate School

I understand that my thesis will become part of the permanent collection of Oregon State University libraries. My signature below authorizes release of my thesis to any reader upon request.

Robert G. Friedel, Author

ACKNOWLEDGEMENTS

Foremost, I would like to thank Dr. Anne Nolin for taking me in as her student, providing invaluable guidance and encouragement, and for showing infinite patience with me in all regards. A special thanks to my parents for being supportive of my idea to leave the professional world to try academia once again.

To my committee members Dr. Warren Cohen and Dr. A. Jon Kimerling, I would like to extend my thanks and appreciation for their support and guidance. A further thanks to Dr. K for looking after me my first term at OSU and getting me on track towards a degree. I would also like to thank Dr. Aaron Wolf for once helping me out when he didn't have to; it was appreciated.

I would like to thank my girlfriend Emily for putting-up with me throughout this whole process, for keeping me fed and clothed during the last few months, and for listening to me prattle on about my research for hours and hours. I would like to thank as a whole the entire Geography class that began this experience with me in the autumn of 2003, and everyone who called the Igloo home at one time or another. You guys made the experience something special. I cannot imagine having gone through this with any other group of people.

This project was a long journey, supported by too many friends and colleagues for me to individually thank all of you in so short a space as this. If I have known you in the last three years, chances are you deserve personal recognition for playing a part in the odyssey that was graduate school. It has been my sincerest pleasure knowing you.

TABLE OF CONTENTS

TABLE OF CONTENTS (Continued)

LIST OF FIGURES

LIST OF FIGURES (Continued)

LIST OF FIGURES (Continued)

LIST OF FIGURES (Continued)

LIST OF FIGURES (Continued)

LIST OF FIGURES (Continued)

LIST OF APPENDIX FIGURES

LIST OF APPENDIX FIGURES (Continued)

LIST OF APPENDIX FIGURES (Continued)

LIST OF APPENDIX FIGURES (Continued)

LIST OF APPENDIX FIGURES (Continued)

LIST OF APPENDIX FIGURES (Continued)

LIST OF TABLES

LIST OF APPENDIX TABLES

A Mathematical Transformation of Multi-angular Remote Sensing Data for the Study of Vegetation Change

INTRODUCTION

Human-induced and natural vegetation changes are important in terms of global carbon cycle, land-atmosphere interactions, and terrestrial ecology. Details about carbon cycle dynamics and the monitoring and assessment of the spatial and temporal variability in Biosphere-Atmosphere-CO_2 exchange is important because of the link between carbon cycle dynamics and climate change as well as other Earth system processes (Schimel 1995). The study of vegetation change on a global scale can be used to derive baseline reference data to evaluate the impact of global climate change on terrestrial ecosystems (Garbulsky and Paruelo 2004) in order to understand human impacts on biosphere-atmosphere-hydrosphere interactions. Satellite-based remote sensing platforms can greatly facilitate the monitoring of vegetation change on a global scale by providing temporally contiguous, multi-spectral and multi-angular samples of radiation reflected and emitted by the Earth.

The use of multi-spectral remote sensing instruments to monitor global vegetation has a lineage going back to the 1970's with instruments such as the Landsat **M**ulti**s**pectral **S**canner (MSS). It is only very recently, with instruments such as the **Pol**arization and **D**irectionality of the **E**arth's **R**eflectances (POLDER) sensor on the French / Japanese satellite ADEOS, the **A**dvanced **S**paceborne **T**hermal **E**mission and **R**eflection Radiometer (ASTER) sensor on the NASA EOS TERRA satellite, and especially the Multi-angle Imaging SpectroRadiometer (MISR), also on TERRA, that satellite remote sensing platforms can sample the angular reflectance as well as the spectral reflectance of the Earth's surface. While single-view-angle (SVA) multi-spectral measurements provide information on the spectral signature of the vegetated canopy, multi-view-angle (MVA) measurements provide information on surface heterogeneity, canopy closure, and the sub-canopy structure of vegetation by sampling surface anisotropy from multiple angles. Structural characteristics are determined by the species of vegetation and the distribution and orientation of 3D

scatterers such as branches, stems, and leaves in the three-dimensional space of the canopy (Kimes 2006).

The objective of this study is to develop a principal components transformation of multi-angle, multi-spectral measurements of the Earth's surface, acquired by the MISR instrument, to assess the possible vegetation information presented in the transformed data space. The principal components will be correlated to available metrics describing physical properties of the scenes. Principal components and transformed data space are then be used to examine the structural dynamics of vegetation after a burn. Principal Components Analysis (PCA) of a multi-band remotely sensed image will result in a set of theoretically uncorrelated, orthogonal components aligned with the band axes that correspond primarily or exclusively with a particular physical scene characteristic, and being viewed "head-on" so that almost all of the variation of the data structure will be visible (Crist 1983; Crist and Kauth 1986)

Terminology

BRDF – Bidirectional Reflectance Distribution Function

- A theoretical description describing the scattering of a parallel beam of radiation from one direction in the hemisphere to another (Schaepman-Strub et al., 2006).

f PAR – Fraction of Photosynthetically Active Radiation

- The fraction of photosynthetically active radiation absorbed by a plant canopy.

BRF – Bidirectional Reflectance Factor:

- The ratio of radiant flux from a surface as illuminated from a single source and viewed from a single view geometry against the radiant flux reflected by a, theoretically perfect, diffusely reflecting surface under identical illumination and viewing geometry (Schaepman-Strub et al., 2006).

HDRF – Hemispherical-directional Reflectance Factor:

- The ratio of radiant flux from a surface as illuminated from a diffuse source (white sky) and viewed from a single view geometry against the radiant flux reflected by a, theoretically perfect, diffusely reflecting surface under identical illumination and viewing geometry (Schaepman-Strub et al., 2006).

Radiance:

- A physical property of energy: The radiant flux per unit solid angle leaving an extended source in a given direction per unit of projected source area in that direction. Measured in ($Wm^{-2}\ sr^{-1}$) (Jensen 2000).

TOA – Top of the Atmosphere

- At-sensor radiance calculated without correcting for atmospheric interference.

EMS – Electromagnetic Spectrum

BACKGROUND AND PREVIOUS WORK

To assess and monitor vegetation change on a global scale, remote sensing by satellite provides a much more viable option than field collection of spectral data. Field measurement of vegetation spectral signatures is limiting in that it requires broad-scale extrapolation to the landscape level (Asner et al., 1998), tends to be locationally and temporally dependent (Asner 1998), and is simply very time consuming to collect (Perry and Lautenschlager 1984). Satellite remote sensing platforms, with their ability to provide coverage of the entire Earth, posses significant potential for monitoring vegetation dynamics over large areas (Myneni et al., 1997; Running et al., 2000). Temporally continuous, multi-spectral imagery possible with satellite remote sensing can be used to assess human-induced and natural vegetation change and carbon cycle dynamics. By providing global coverage of vegetation change, a key component of global carbon cycle, remote sensing creates a bridge between this global measurement of the carbon cycle and local and landscape atmospheric research (Asner et al., 1998).

The ability of the MISR sensor to sample surface anisotropy from nine angles within seven minutes represents a considerable improvement over characterization of surface anisotropy using composites from wide field-of-view single camera instruments. Characterizing the anisotropy of the Earth's surface will enhance the capability of derived measurements of physical systems from satellite measurements (Pinty et al., 2002) and will translate into better and more accurate measurements of the Fraction of Photosynthetically Active Radiation (f PAR) (Gobron et al., 2002) and better estimations of shortwave hemispherical reflectance (Kimes and Sellers 1985). Products derived from the MISR instrument may offer significant improvement in characterization of the angular reflectance of vegetation.

Multiple View Angles and the Specular Anisotropy of Vegetation

All surfaces, natural and man-made, scatter incident radiation anisotropically as described by the **B**i-directional **R**eflectance **D**istribution **F**unction (BRDF)

(Nicodemus et al., 1977; Russel et al., 1997; Pinty et al., 2002; Schaepman-Strub et al., 2006). The shape and magnitude of the BRDF is controlled by the composition, density, optical properties, and geometric structure of the canopy and is indicative of canopy structure and of the underlying ground (Widlowski et al., 2001; Pinty et al., 2002; Zhang et al., 2002).

Vegetated surfaces are 3-D constructs, with the below-canopy structure, substrate albedo and BRDF, and canopy characteristics as much of a factor on the anisotropy of reflectance as the canopy itself (Asner et al., 1998). At a fine scale, the sub-canopy structural attributes are the primary factor controlling canopy spectral reflectance. The orientation of the leaves, stems, the presence of standing litter, and the size of the trunk are the important factors in the canopy radiation environment (Ni et al., 1997; Asner 1998). At the landscape level, however, as many disparate vegetation communities become aggregated to a single pixel, the relative ground cover and the spatial distribution of vegetation largely determines the shape and magnitude of the BRDF (Asner et al., 1998).

Single-view-angle remote sensing platforms can fail to adequately capture the shape of the BRDF and are therefore not able to provide information on the structure of vegetation controlling the shape and magnitude of the BRDF. Using multiple view angles to sample the BRDF of a vegetated surface may lead to a more accurate characterization of surface anisotropy than is possible with SVA remote sensing platforms.

Multiple view angles are a necessary component of surface anisotropy measurements from a remote sensing platform (Diner et al., 1999). While the ability to detect structural signatures in Bidirectional Reflectance Factor (BRF) samples is directly dependent upon the spatial resolution of the sample (Pinty et al., 2002), recent work has demonstrated that multi-angle remote sensing measurements can provide unique information on forest cover density and structure (Widlowski et al., 2001; Pinty et al., 2002; Braswell et al., 2003; Nolin 2004). With the ability to assess surface anisotropy from multiple angles, MVA sensors such as POLDER, ASTER, and MISR can improve upon current methods of remote sensing of vegetation (Pinty

et al., 2002). Angular measurements of reflected radiation, combined with multi-spectral measurements, can provide information about the structure and photosynthetic activity of vegetation (Pinty et al., 2002), and of canopy structural parameters and ecological parameter estimates at local to global scales (Asner et al., 1998; Diner et al., 1999).

The inclusion of multi-angle data when inverting 3-D optical models will also lead to improved recovery of forest parameters (Kimes et al., 2002). Ni et al., (Ni et al., 1999) found in preliminary studies that the patterns of variance in the bi-directional reflectance over discontinuous canopies can be related to the physical properties of the canopies. A model of surface anisotropy measurements acquired by MISR will offer improved ability to understand and compare the structural characteristics of vegetated landscapes on a global scale.

MISR is uniquely capable of sampling the angular distribution of energy reflected by the Earth's surface (Asner et al., 1998). A major benefit of MISR for the sampling of surface anisotropy over wide field-of-view (FOV) scanners such as the **Mod**erate Resolution **I**maging **S**pectroradiometer (MODIS) or ASTER; is that with wide FOV scanners, the angular signatures of targets are a composite of multi-temporal scenes using statistical assumptions that may not apply to all scenes (Diner et al., 1999), with atmospheric and surface conditions that are not constant across time (Zhang et al., 2002). The angular signatures captured by MISR are obtained without multi-temporal compositing; of scenes that are, with the exception of clouds and wind driven reflectance changes, more-or-less physically static over the seven minutes required to capture a scene from its nine cameras (Diner et al., 1999). This enables MISR to assess the anisotropy of the Earth's surface at the global scale and to further our understanding of the structure of plant canopies (Xavier and Galvao 2005) citing (Martonchik et al., 1998; Gobron et al., 2000; Gobron et al., 2002). A model or metric describing the spectral and angular characteristics of vegetation as captured by MISR would greatly facilitate the interpretation of the variations in surface anisotropy of various landscapes.

Models to Interpret Remote Sensing Imagery

All approaches to the interpretation of remotely sensed imagery use models as a foundation (Gobron et al., 2000). These models can be explicit, e.g. Radiative Transfer Models, or implicit, e.g. Vegetation Indices. One of the simplest and most common methods of quantifying vegetation coverage and health, and assessing vegetation change is through vegetation indices.

Many remote sensing derived vegetation indices are formed from linear combinations of reflectance which reduce multi-channel satellite data to a single number, providing a metric for comparing vegetation estimates across different sensors (Perry and Lautenschlager 1984). These vegetation indices provide a more direct association between signal response and physical processes on the ground, and highlight the information of greatest interest (Crist et al., 1986). These metrics also provide a method to compare the scenes of disparate sensors. As is the case with most multi-spectral SVA sensors, if the spectral bands are not statistically independent, the derived vegetation index will not be able to best represent the full dynamic range of variability in multi-spectral observations of vegetation (Jackson 1983). Additionally, vegetation indices derived from SVA remote sensing platforms cannot resolve the spatial and temporal changes in plant structural characteristics (Diner et al., 1999). Principal Component Analysis of the multiple spectral bands and camera angles provided by MISR provides a means of de-correlating the multiple bands and angles to assess the unique properties of the information present.

Data Visualization in N-Dimensional Space

Classes of vegetation share certain fundamental physical properties such as leaf pigments, stems, and the cellular structure of leaves. The result of these shared physical and chemical properties is that most species of vegetation have roughly similar, but still unique, spectral reflectance curves (Crist and Kauth 1986). Because different species of vegetation have unique spectral reflectance curves, the spectral response of a vegetated scene projected into multi-dimensional space will not appear as a shapeless cloud of points, but will be concentrated in certain portions of the data

space, with a predictable and definable structure, as governed by the classes of vegetation and the physical properties of the scene (Crist and Kauth 1986).

For any given multi-spectral sensor with more than two bands, the structures present in the data are related to physical characteristics of the scene, but the correlation between bands causes the data to be skewed and not aligned with any pair of band axes when viewed in multi-dimensional space (Crist and Kauth 1986).

Principal Components Analysis of MISR imagery would provide a means of reducing the multi-spectral and multi-angular information to a fewer number of components that account for nearly all of the information present. A PCA of MISR would also provide a means to correlate the new axis to specific physical properties of a scene.

Principal Components

Originally developed by Karl Pearson (1901) and Harold Hotelling (1933), PCA is an ordination technique that projects a cloud of points into a space of fewer dimensions, creating new orthogonal axes maximizing the variance (Gauch 1982). PCA of multi-spectral satellite imagery is a linear transformation that transforms all of the variance of the original 'n' bands of data by compressing the variance of the 'n' bands into a set of 'x' uncorrelated new variables (components) equal to the number of input bands (Jenson and Waltz 1979). The resulting new axes are statistically orthogonal to each other, where each new axis (component) accounts for the maximum amount of variance in the original dataset, less than the previous component (Davis 1973; Gauch 1982; Chavez 1989; Carr 2002). PCA effectively reduces the dimensionality of the dataset (Crist and Cicone 1984; Crist and Cicone 1984a; Chavez 1989). While the theoretical foundation of PCA is the preservation of all of the original variance of the input dataset in a set of new orthogonal axes; in multi-band remotely sensed imagery the lower order components account for very little of the original variance and can often be discarded as noise (Jenson and Waltz 1979).

METHODOLOGY

Instrument Description

The MISR instrument is onboard NASA's EOS TERRA satellite. The TERRA satellite is in a sun-synchronous, polar-descending orbit at 98.3°, crossing the equator at 10:30 a.m. (local time) every day. TERRA completes the Pole-to-Pole trip in 99 minutes, giving the MISR sensor global coverage in 9 days, and dividing the Earth into 233 distinct MISR "Paths". A MISR Path is the descending polar trajectory. For any given Path, a MISR orbit is defined as the swath of land captured by the sensor along that Path, at that date, from the North to the South Pole. Each orbit is divided into 180 blocks, each block having the dimensions of approximately 141 kilometers along-track and 563 kilometers cross-track.

Table 1. MISR Instrument Specifications (Diner et al., 1998)

Camera Angles	+/- 70.5º (Df & Da); +/- 60.0º (Cf & Ca); +/- 45.6º (Bf & Ba); +/- 26.1º (Af & Aa); 0º (Nadir)
Spectral Bands	448 nm (blue); 558 nm (green); 672 nm (red); 866 nm (NIR)
Spatial Resolution	275 meter (Nadir & all off-nadir red bands) 1.1 kilometer (blue, green, Near-IR off-nadir bands)
Quantization	14 bits, square-root encoded to 12 bits
Swath Width	360 kilometers (common overlap of all 9 cameras)

MISR Datasets

The MISR Level 1B2 Global Mode Terrain Radiance product (MI1B2T) was selected for this study. The MI1B2T product is terrain-projected, Top of Atmosphere (TOA) radiance. The radiance values have been preprocessed to compensate for focal plane scattering and to account for the different spectral sensitivity of the detector elements for each band and camera (MISRa 2006). This MI1B2T product was selected over using the raw signal counts because the conversion of digital number to radiance can remove issues stemming from the minute differences between input

bands (Singh and Harrision 1985), and for the aforementioned instrument correction provided by the NASA Langley Research Center (LARC).

The MISR Level 1B3 Radiometric Camera-by-camera Cloud Mask (MIRCCM) was selected as a cloud mask. The MIRCCM has a spatial resolution of 1.1 kilometers, capable of detecting clouds over land with optical depths > 0.1 (MISRb 2006). A drawback of the MIRCCM is that while it will not classify a clear pixel as being cloudy, its optical depth sometimes results in the higher altitude thin and wispy clouds being missed.

The MISR Ancillary Geographic Product (MIANCAGP) was used to extract the latitude and longitude of the MISR Paths. This information was used to georeference the MISR blocks to the MISR Sinusoidal Oblique Mercator (SOM) projection. The MISR Geometric Parameters file (MIB2GEOP) was used to extract the sensor and solar zenith and azimuth angles. This information was used to convert the TOA radiance values to TOA BRF.

Vegetation Datasets

Vegetation density at the study sites was assessed using the MODIS / Terra Vegetation Continuous Fields Yearly L3 Global 500m ISIS Grid V003 (MOD44B) product. The MODIS VCF product consists of proportional estimates of ground cover at 500 meter spatial resolution, over 1 year (MODIS-VCF 2006). The VCF product at the time of analysis included three classifications of ground cover: percent bare, percent non-tree vegetation, and percent tree cover.

The 1992 National Land Cover Dataset from the USGS Landcover Institute (LCI 2006) was used as a land cover classification guide. The 30 meter spatial resolution of the 1992 NLCD was the overriding factor in its selection over other land cover classification products. The 1992 NLCD is derived from Landsat 5 imagery collected in the early 1990's and has coverage extending across the United States. Land cover clusters for the 1992 NLCD were developed using an unsupervised clustering algorithm of leaf-on and leaf-off TM scenes on a state-by-state basis. The resultant land cover clusters were then categorized using field data and aerial

photography. The final product consists of 21 land cover classes (Appendix E Table 12)

Vegetation classes from the Oregon Gap Analysis Program (GAP) (OR-GEO 2006) were used to identify species of vegetation in the Siskiyou National Forest. The GAP classes were created in 1992 from visual interpretation of 1:250,000 Landsat MSS false-color prints. The GAP regions represent 133 primary types of vegetation, with a nominal polygon mapping size of approximately 133 hectares.

Ancillary Datasets

Digital Elevation Models (DEM) were used to evaluate topography. 1/3 arc-second DEMs from the USGS National Elevation Dataset (NED 2006) were used to derive hillshade and slope layers. Landsat ETM + from 1999 – 2002 (GLCF 2006) was used to provide higher resolution verification of the landcover than was possible with the 275 meter resolution of MISR.

Software Used

All image processing was done using custom scripts written in the Interactive Data Language (IDL). Spatial Resampling and spatial subsetting of imagery was done in RSI ENVI 4.2. A geodatabase was created through ArcGIS 9 for reprojection and alignment of spatial data for analysis. The ArcGIS Spatial Analyst was used to create the hillshade and slope layers from the DEMs.

Derivation of the PCA Coefficients of Rotation

To create a sample of varied land cover over a full phenological cycle, MISR data was spatially selected to cover multiple unique biomes, and temporally to cover plant phenology (Table 2). This sample was created to be inclusive of as many different types of vegetation as possible. Sites were selected using the Bigfoot sites (Cohen et al., 2006) as a guide. A Bigfoot site is a 5 x 5 kilometer block of land covered by a single distinct class of vegetation. A PCA was applied to the variance-covariance matrix (un-standardized PCA) of the sample.

The rotation coefficients are those used to rotate the sample data space to the principal components. The principal components themselves are derived from matrix algebra and have not themselves been rotated by any means. The coefficients of rotation derived from this PCA sample were applied to individual pixel samples to evaluate vegetation in the transformed data space.

Principal Component Analysis

The coefficients of rotation derived from sample were applied to multiple pixels to evaluate the correlation between principal components and measurable properties of the scene, the effects of topography, the effects of vegetation density / canopy closure, and an evaluation of the structural dynamics of vegetation after a burn.

Ten principal component correlation study sites, totaling 30 pixels, were selected to evaluate the correlation between the principal components and measurable physical properties of the scene (Figure 5, Table 3). Correlation study sites were selected to target specific land cover in different climatic regions of the United States. Samples were selected represent dissimilar types of vegetation, as identified by the 1992 NLCD, and at various densities and canopy closure, as determined by the MODIS VCF and Landsat ETM.

Principal component 1 (PC 1) was correlated against NDVI to determine the degree of correlation between the first principal component and a metric of vegetation. Principal component 2 (PC 2) was correlated against solar zenith angle and against the relative azimuth angle between the sensor and the angle of incident radiation to determine the degree of correlation between the second principal component and varying solar illumination.

Topography varies among sites and samples within sites. Site selection was constrained by the need to find cloud free imagery over a full phenological cycle, so it was not always possible to select areas of flat or uniform topography. To assess the influence of topography on the principal components, samples targeting western-juniper-dominated landscapes of differing topographic profiles were examined. A

single sample was selected from each of the Western Juniper correlation study sites to be at similar latitude, similar vegetation densities, sampled from the same dates / orbits, residing on different topography.

The effect of vegetation density on the principal components was compared at two sites of different land cover and soil background. The first site was of evergreen forest on the east slopes of the Cascades in west-central Oregon, an area dominated by ponderosa pine. These samples were selected from the same region as the Evergreen – A correlation study site. The second site was from the shrublands and grasslands of southern New Mexico, from the same region as the Shrubland correlation study site. To minimize the influence of differing solar and viewing geometry on the principal components, the samples at each site were selected at nearly identical latitudes, and as near to each other as possible. The evergreen samples are approximately 10 kilometers apart. The five shrubland / grassland samples are no more than 40 kilometers distant across their breadth.

A preliminary investigation into the ability of the principal components to relate the changes in vegetation after a stand-replacing disturbance was conducted for the Biscuit Fire Complex in the Siskiyou National Forest. The Biscuit Complex was selected due to the availability of local resources on the forest and the burn. One orbit prior to the Biscuit fire (June, 2001) and one orbit after the fire (June, 2003) were selected to evaluate the effects of the burn in PCA space. Assessment was done on specific pixels of varying burn intensity, on a cross-section of the burned area, and at the landscape level on the whole of the Biscuit Complex Fire.

DATA PROCESSING

MISR Subsetting and Scaling to Surface Reflectance

A MISR orbit consists of nine separate files in Hierarchical Data Format (.hdf) containing the camera radiance values with one file for each of the nine MISR cameras. Each of the nine MI1B2T files for a particular orbit was subset to the same 5-block range and combined to a single array. The 5-block mosaic of the MISR path was georeferenced to the MISR SOM projection for its respective path. The mosaic was then spatially subset to 900 samples (columns) x 2560 lines. This was done to insure complete overlap of scenes in multi-temporal compositing. It also facilitated the geometric alignment and interpolation of values when matching ancillary datasets to the MISR scenes.

The blue, green, and NIR nadir bands were removed from all cameras in the sample. The off-nadir blue, green, and NIR bands, available in Global Mode at 1.1 kilometers, were removed for want of the highest spatial resolution possible. The nadir camera blue, green, and NIR bands were removed on the supposition that the additional spectral bands at nadir were dominating the reflectance of the sample and obscuring the angular signature. Removal of the extra spectral information from the nadir camera will not affect the ability of the dataset to characterize the anisotropy of the scene. Pinty et al. (2002)(Pinty et al., 2002) found that the red band maximizes the single scattering effect, and that the heterogeneity of a landscape can be characterized by sampling the angular reflectance in the red band only of the multi-spectral sensor. This results in a red-band-sampled BRDF that is sensitive to canopy cover, tree pattern, tree distribution, and canopy gaps (Gerard and North 1997). Furthermore, in the red region of the Electromagnetic Spectrum (EMS) (650 nm) the contrast between vegetation and background soil is the greatest (Pinty et al., 2002; Chopping et al., 2004).

Additionally, the Df and Da cameras, at 70.5° fore and aft, were removed from the dataset. The distance reflected radiation must travel from the Earth's surface to the sensor at the Da and Df cameras is approximately three times greater than the

distance required to travel to the sensor at nadir. This extra travel distance through the atmosphere results in much higher levels of haze and atmospheric scattering in the image at these extreme angles and reduces the retrievable area of a scene. The Da and Df cameras are also the must susceptible to topographic shadowing by steep terrain (MISRb 2006).

After band reduction, a single five-block subset of a MISR orbit was an array of dimensions: 900 pixels x 2560 pixels (at 275 meter resolution) x 7 bands (3 red bands fore and aft at: +- 60.0°, +- 45.6°, +- 26.1°, and nadir) (Figure 1). The area covered by a single subset orbit is approximately 174,240 sq. kilometers.

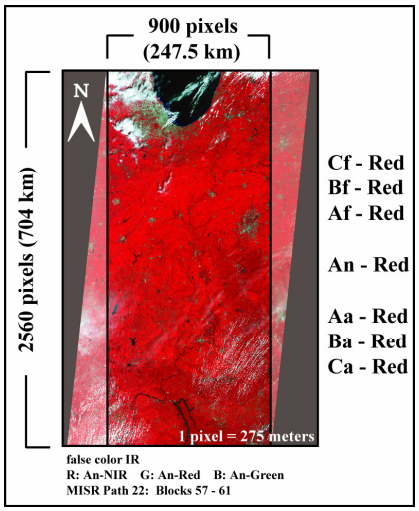

Figure 1. Example of the final spatial dimensions and spectral resolution of a processed MISR orbit

After projection and spectral and spatial subsetting, the MI1B2T radiance values were converted to TOA BRF (Equation 1). The conversion of radiance to TOA BRF normalizes much of the affect of changing illumination geometry on different scenes (Chengquan et al., 2002).

$$BRF = (\pi * R * D^2 / \Omega / \Phi) \qquad \textbf{Equation 1}$$

where, $\pi = 3.1415927$
R = camera radiance * camera scale factor
D = solar distance
Ω = solar weighted height
Φ = cos (solar zenith angle * (π / 180))

The TOA BRF was scaled to surface HDRF by dark pixel subtraction using band minimum values to correct for atmospheric interference. Dark pixel subtraction corrects for the diffuse sky irradiance by removing the non-zero value of the lowest brightness value pixel from every pixel in the image, assuming that the value at the lowest pixel is the result of additive effect of atmospheric scattering (Crippen 1987). Each block and band of MI1B2T BRF was atmospherically corrected using its respective block / band minimum value.

Masking

A cloud mask was created using the MIRCCM. Provided at 1.1 kilometer spatial resolution and resampled by Nearest Neighbor interpolation to 275 meters to match the spatial resolution of the PCA sample, only pixels flagged in the MIRCCM as being 'High Confidence Clear' were retained. A water mask was created using a series of thresholds combining the Normalized Difference Vegetation Index (NDVI) and the Normalized Difference Snow Index (NDSI); derived from the spectral bands of the nadir camera (Equation 2 and Equation 3). NDVI and NDSI are defined as:

$$\mathbf{NDVI = (\rho_{NIR} - \rho_{Red}) / (\rho_{NIR} + \rho_{Red})} \qquad \textbf{Equation 2}$$

$$\mathbf{NDSI = (\rho_{Blue} - \rho_{NIR}) / (\rho_{Blue} + \rho_{NIR})} \qquad \textbf{Equation 3}$$

where, ρ_{NIR}, ρ_{Red}, and ρ_{Blue} are MISR surface reflectance in the NIR, red, and blue channels.

Water bodies were masked using two passes of masking: First to mask the water bodies themselves, and a second pass masking the shorelines. The initial pass, masking any pixel where (NDSI > -0.15), captured most of the water in a scene as well as some snow. The second pass, masking any pixel where ((0.5 < NDVI < 0.65) and NDSI > -0.3)) captured the boundary between water and land.

Equation 1 Normalized Difference Vegetation Index

$NDVI = (_{near\text{-}IR} - _{Red}) / (_{near\text{-}IR} + _{Red})$

Similar to the water mask, a snow mask was created using thresholds of NDVI and NDSI. Pixels with values where (NDVI < 0.1 or NDSI > -0.05) were flagged as being snow covered. The snow mask encompassed most snow-covered areas, although the boundary between snow and non-snow areas was not always captured. The snow mask proved effective at eliminating most of the snow in the imagery. It had the added effect of also masking clouds missed by the MIRCCM.

Equation 2 Normalized Difference Snow Index

NDSI = (Blue – near-IR) / (Blue + near-IR)

The Water and Snow masking thresholds were tested on various orbits over every Path and are a compromise between targeted area masked vs. terrain lost due to masking. In any masked image, trace amounts of cloud, water, and snow remain.

Due to the 275 meter resolution of the MISR imagery there remains the issue of mixed land / water / cloud / snow pixels in the imagery. Some terrain, especially urban areas and near-water terrain, was included in the water and snow masking thresholds and removed from the scene. The water and snow masks also occasionally masked bright ground such as bare soil and sand.

Ancillary Data Resampling and Alignment with MISR

The 1992 NLCD and MODIS VCF were spatially resampled to match the 275 meter spatial resolution of the MI1B2T product. The 1992 NLCD was scaled up from 30 meters using nearest neighbor interpolation. The nearest neighbor interpolation was essential due to the discrete nature of the 1992 NLCD (21 classes), and the necessity to retain the same values in the resampled data. The MODIS VCF product was scaled down from 500 meters to 275 meters using cubic convolution. The cubic convolution method was chosen because it will produce a more continuous result than nearest neighbor or bilinear resampling. The drawback of this method is that the three categories of percent vegetation cover will not always sum to exactly 100%.

RESULTS

Derivation of the PCA Coefficients of Rotation

To create the sample from which to derive the PCA coefficients of rotation, a sample of land cover differing in vegetation type, height, density, spatial distribution, soil background, and phenological characteristics was created. MISR paths were selected that covered the 9 Western Hemisphere Bigfoot sites (Figure 2).

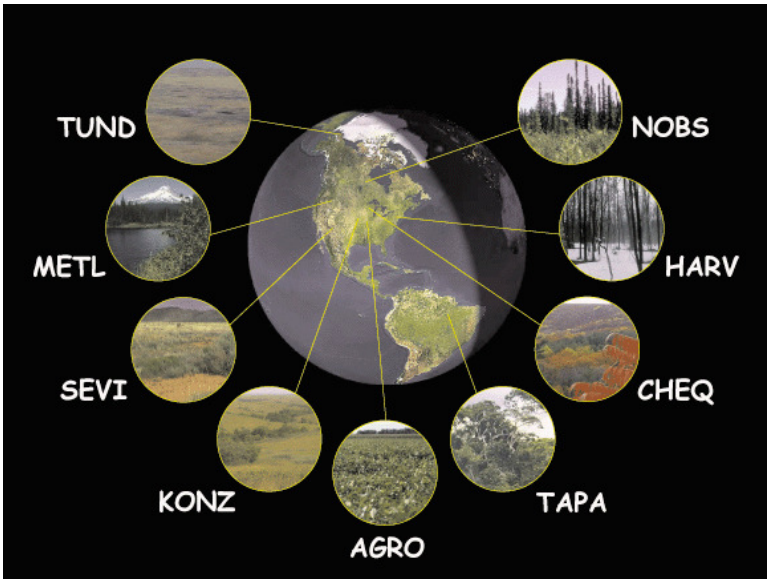

Figure 2. Bigfoot study sites (Oregon State University – Forestry Sciences Laboratory)

For each MISR Path selected, a five-block subset was selected to include the Bigfoot site and two blocks north and south of the site. Using the online MISR Browse Tool, each Path was visually screened for clouds and only those orbits where the Bigfoot site appeared to be cloud-free were tagged for download. At least one orbit for each path was desired from each month of the year to obtain a sample of vegetation in different phenological states. Orbits were selected from January 2001 – December 2005 to cover this range. After online screening for clouds, and temporal selection for phenology, the final size of the sample downloaded from LARC was:

469 5-block subset orbits, from 24 paths, from 2001 – 2005. The low resolution of the imagery available through the MISR Browse Tool, and that only the nadir camera angle was used for screening, led to many paths being tagged as having a clear Bigfoot site that were later found to be obscured by clouds.

Initially, the sample for PCA was to be comprised exclusively of the Bigfoot sites for verifiable ground cover and for the vegetation metrics available at each site. The unavoidable presence of clouds over many of the sites made this infeasible.

Following the methodology of Crist and Cicone (Crist 1983; Crist and Cicone 1984a), who built their sample for a TM Tasseled Cap transformation from field collected spectra of agricultural plots and laboratory collected soil spectra, a sample of approximately 500,000 pixels was created from the processed MI1B2T data to represent the desired variety of vegetation type and structure.

Instead of using predefined targets in the Bigfoot sites, each MISR Path was screened to identify the pixels for that Path that were cloud and snow free at each orbit regardless of where in the United States they were. Water and snow masks were not applied. From this list of possible pixels, clusters of pixels representing multiple unique land cover classifications as identified by the 1992 NLCD were chosen for the sample (Table 2). Images for each orbit and each camera were visually inspected to be cloud and snow free.

Table 2. PCA sample description. Location is given as a general reference. Samples were not taken from outside of this region. The primary vegetation class is identified, but each site is comprised of many samples of various land cover

SITE	PIXELS	LOCATION
Deciduous / mixed forest	16,055	Along the Missouri river in Iowa and Nebraska
Evergreen / mixed forest	9,699	S.W. Kentucky
Row crops / small grains	67,745	S.E. Nebraska
Pasture & Hay / row crops / small grains / natural vegetation	5,904	Most of E. Nebraska
Soils and Fallow Ground	43,979	Central Oregon
Grassland / Shrubland / herbaceous	8,898	S.E. New Mexico
Pasture & Hay	1,485	Central New Mexico
Grassland / Shrubland / transitional	298,148	S. New Mexico
Grassland / various agriculture	35,703	Eastern Kansas and Nebraska

The targeted vegetation classes were all selected to be away from visible urban centers and human settlements. Landsat ETM + from 2001 – 2003 (Global Land Cover Facility) images were used as verification that the areas selected for sampling in the MISR images matched what was described by the NLCD. The size of the sample dataset used for PCA is 487,616 pixels of a wide variety of vegetation and soil conditions, over a full calendar year.

This sample was inclusive of nearly all of the International Geosphere-Biosphere Programme (IGBP) land cover classes. All of the IGBP classes were sampled to some degree except: permanent wetland, urban / built up, and permanent snow and ice.

The principal components were derived from variance-covariance matrix (un-standardized PCA) of the PCA sample. The first component explained 93.6% of the variance in the sample, the second component 5%, and the third 0.9% (Figure 3). The first three components cumulatively explain 99.5% of the variance of the sample. The factor loading matrix (Figure 4) indicates a clear association between the first component with the total reflectance of the scene, and the second component as a contrast between for the fore and aft cameras. The coefficients of rotation are presented in Appendix Table 13. While it could not be statistically confirmed that only the first three principal components carried unique information, the fact that four lowest-order principal components cumulatively explain 0.5% of the total variance, they are most likely noise and were not examined.

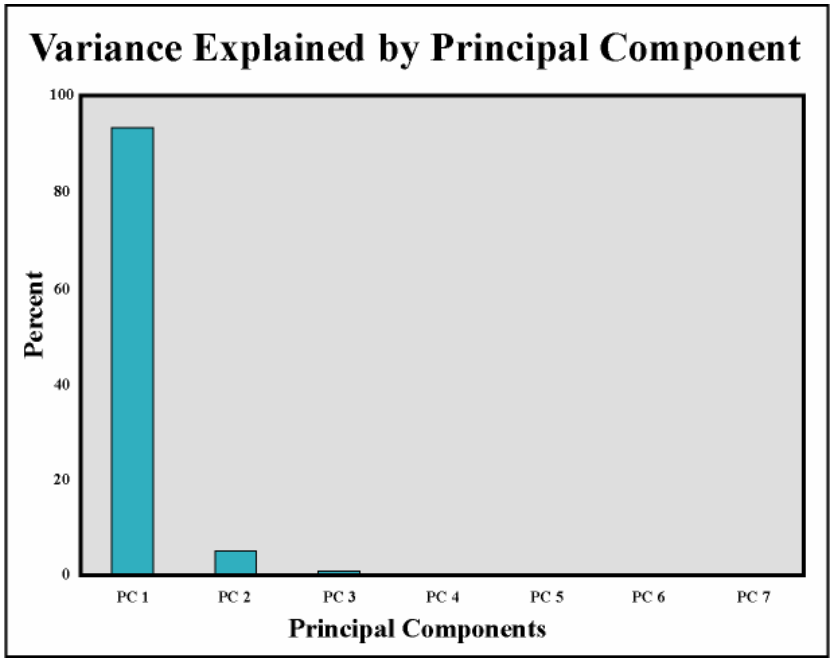

Figure 3. Percent variance explained by principal components

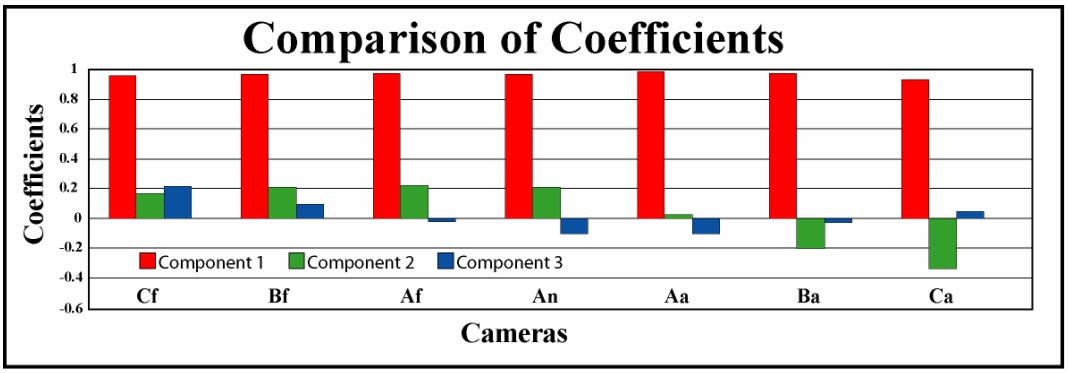

Figure 4. PCA Factor Loading Matrix

The first component, explaining ~93% of the variance, loads positively into all of the input cameras. All of the factor loadings are very high and nearly equal, with an average loading of 0.97 and a standard deviation of 0.01. This first component is the weighted sum of all of the reflectance bands.

The second component, explaining 5% of the variance, loads positively into the fore cameras (Cf, Bf, Af), nadir (An), and the first aft camera (Aa). The other two aft cameras, Ba and Ca, contain negative factor loadings. The fore and nadir cameras have similar factor loading values, averaging 0.2 with a standard deviation of 0.02. The positive loading of the first aft camera, Aa, is 89% less than the average of the other positive loadings. The negatively loaded cameras increase in magnitude away from nadir, with camera Ca loading 40% more heavily than camera Ba. With the exception of camera Aa, the second component indicates a clear contrast between forward and nadir reflectance, and aft reflectance.

The third component, explaining just less than 1% of the variance, loads positively into the Cf, Aa, and Ba cameras. All other cameras contain negative loadings. The Cf camera has the greatest weighting, approximately 70% higher than the average of the absolute value of the other cameras, and approximately twice as high as the absolute value of the next highest camera loading.

Correlation Analysis of Principal Components

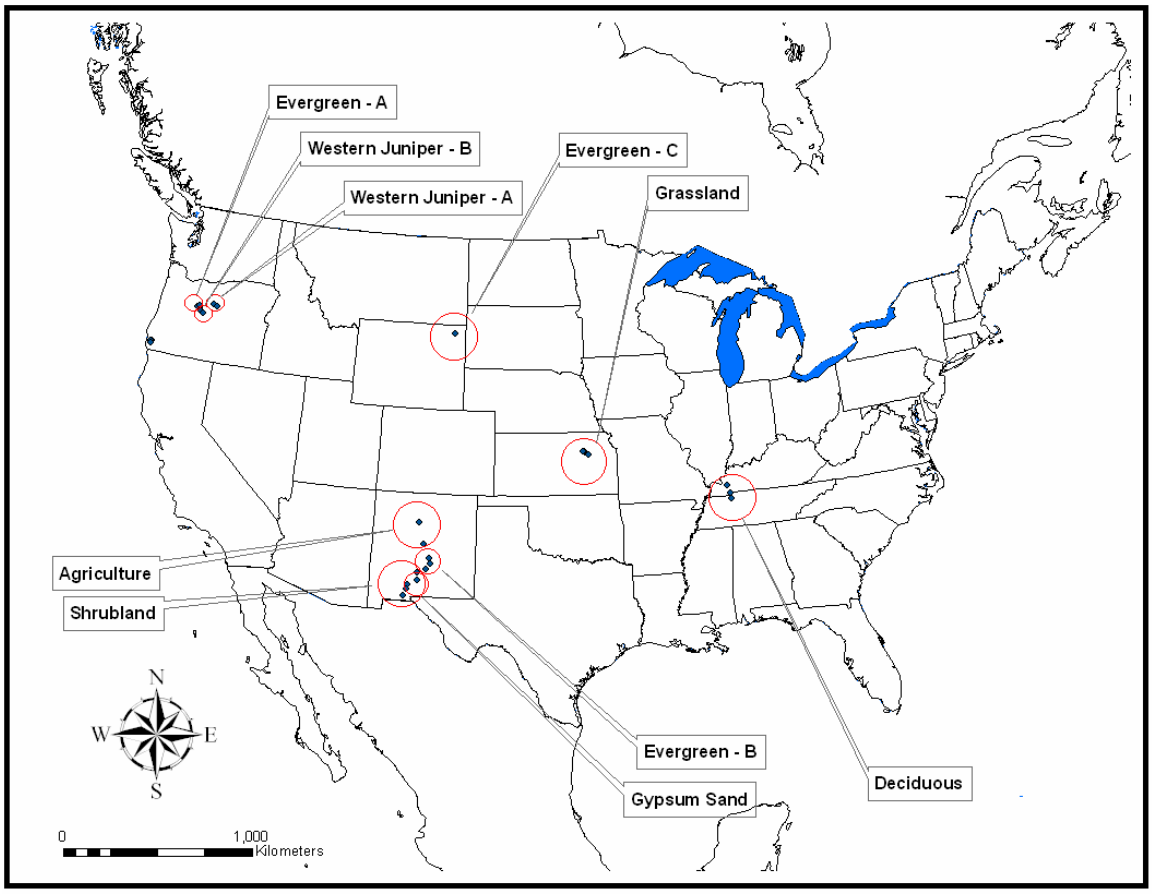

Figure 5. Site Analysis: Principal component correlation study sites

Sites to examine the correlation between principal components and metrics of vegetation and solar illumination were selected to represent different classes of vegetation at different latitudes and climatic regions (Figure 5, Table 3). Thirty pixels, from ten sites were selected across the United States were selected to examine the degree of correlation between the principal components and metrics of vegetation and illumination.

Table 3. Site Analysis: Principal component correlation study sites descriptions

SITE	SAMPLES	DESCRIPTION
Deciduous	3	Closed and patchy canopy deciduous forest
Evergreen Needleleaf - A	2	Evergreen needleleaf forest with low percentage of bare ground
Evergreen Needleleaf - B	3	Evergreen needleleaf forest with low percentage of bare ground
Evergreen Needleleaf - C	4	Evergreen needleleaf forest with moderate to high percentage of bare ground
Grassland	4	Grassland of varying percentage of bare ground with dynamic phenology
Shrubland	4	Shrubland and grassland with low dynamic phenology
Agriculture	3	Fields and central-pivot irrigation systems.
Western Juniper A	2	Western juniper dominated landscape with bright soil background on rugged topography
Western Juniper B	3	Western juniper dominated landscape with bright soil background on flat to gently undulating topography
Gypsum Sand	2	High reflectance ground devoid of vegetation

The Deciduous site was chosen to examine tall vegetation with a dynamic phenological cycle. The three Evergreen sites (A, B, C) were selected to examine different sites of evergreen vegetation due to its relatively static phenological cycle. The Evergreen – A and Evergreen – B sites were selected to sample evergreen needleleaf vegetation at different latitudes. The Evergreen – C site was selected in the hope that the shadowing cast by a large phenologically invariant feature, Devils Tower, would provide insight into the variation in the principal components. The Grassland site was selected to examine shorter vegetation with smaller trunks than the deciduous samples that also have dynamic phenological cycles. The Agriculture site was selected to examine the phenological changes in vegetation that are not directly tied to climatic conditions. The Western Juniper sites (A, B) were selected to examine evergreen shrub vegetation that has relatively static phenological cycles and

bright soil background. The Gypsum Sand site was selected to examine an area completely devoid of vegetation that has very high reflectance.

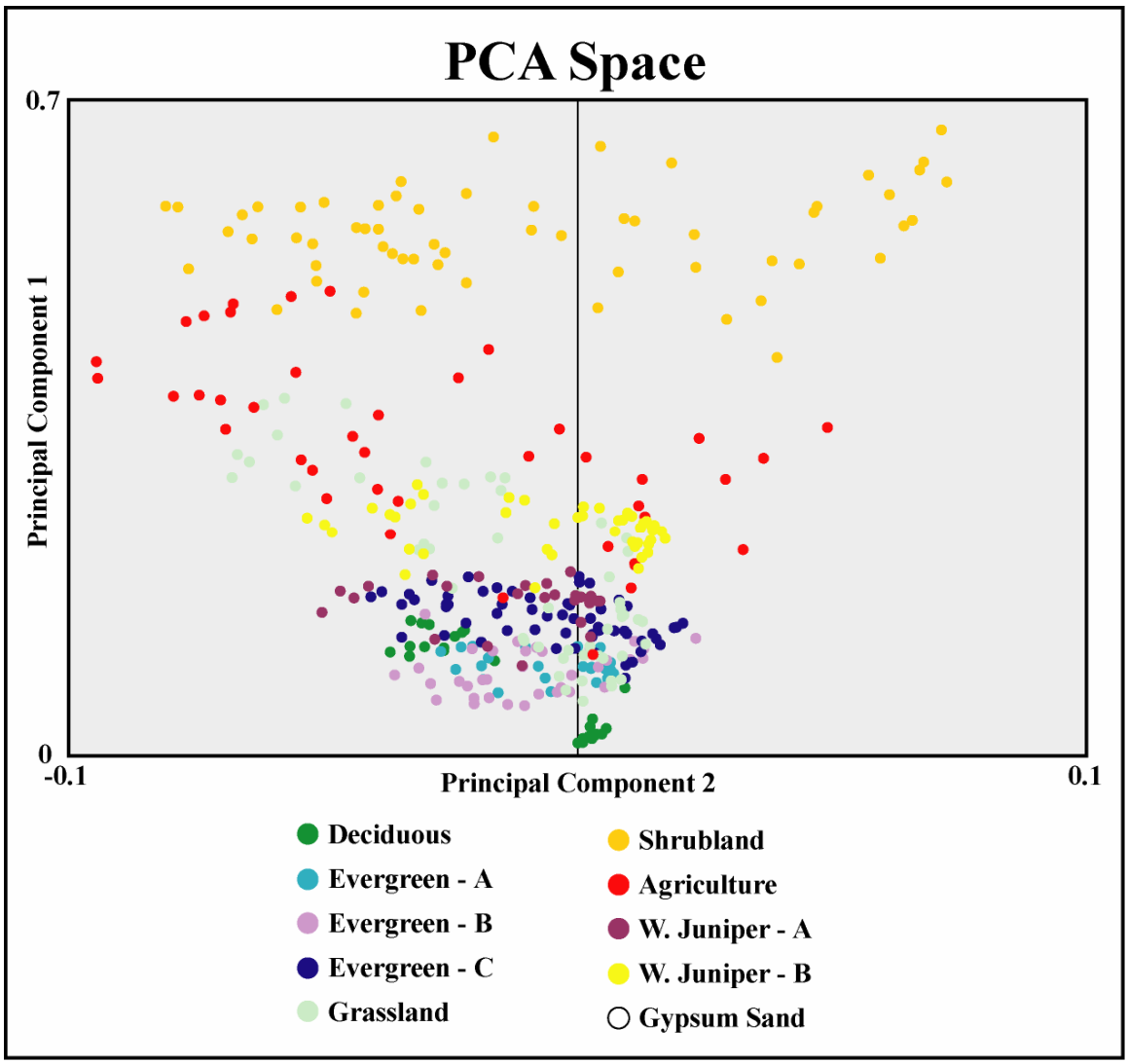

Figure 6. Site Analysis: Vegetation samples in PCA space: PC 1 and PC 2. The PCA space displays every sampled date for each vegetation sample to illustrate the phenological range of each vegetation sample in relation to the other samples

The PCA space defined by the PC 1 vs. PC 2 axes (Figure 6) shows each of the sample sites in distinct regions of the PCA space. The shape of the space defined by the vegetation samples in this dimension can be described as a cone standing on its tip - the 'M-Cone'. The tip of the cone is located at zero along the PC 1 and PC 2

axes and is nearly devoid of sample points. From this start, the vegetation classes fill up the PCA space, increasing in range positively and negatively along the PC 2 axis as the magnitude of PC 1 increases from zero. Most of the samples share the same PCA space along the PC 2 axis but not along the PC 1 axis. Samples with dynamic phenological cycles move significantly more than other samples along the PC 1 axis.

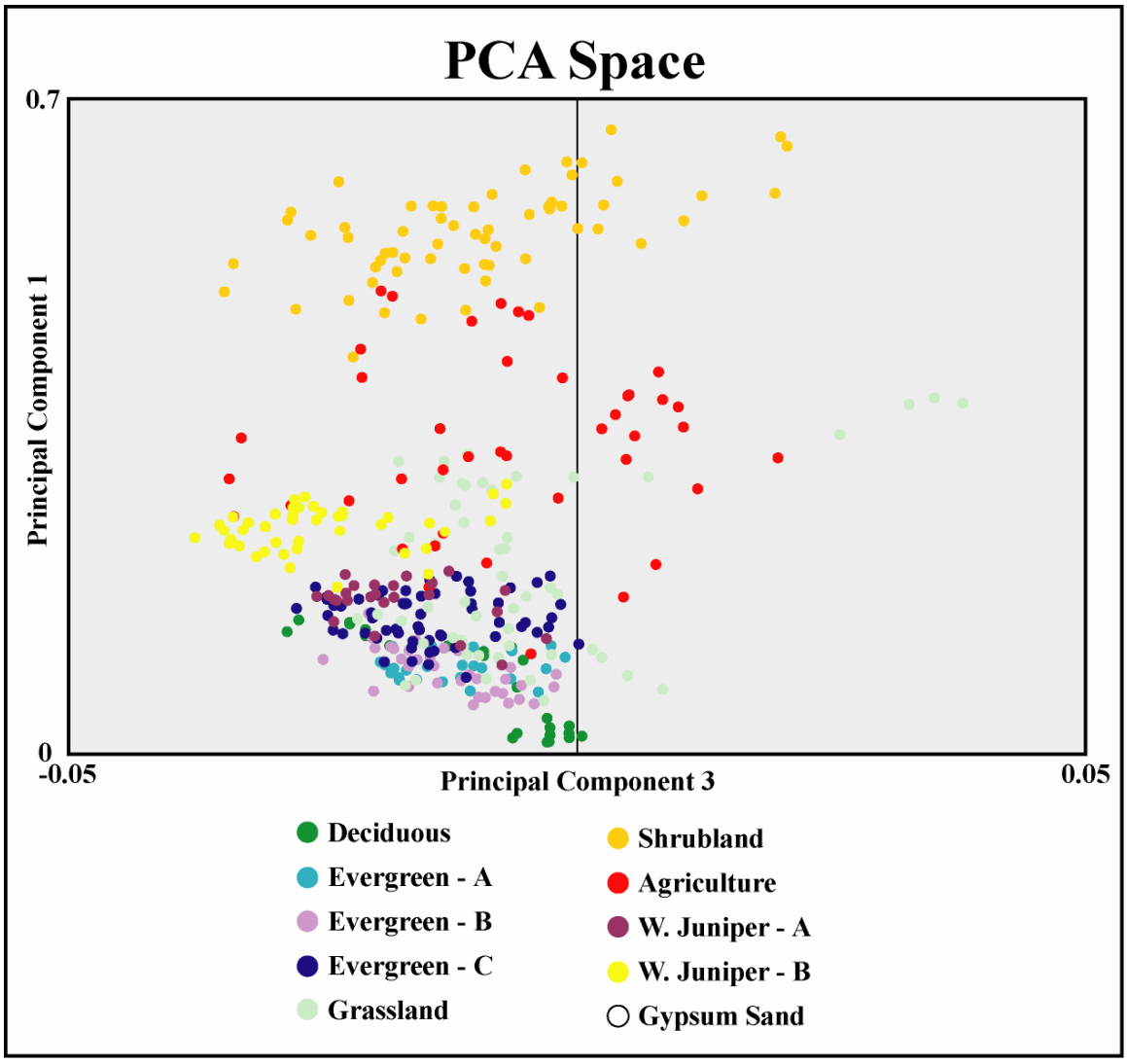

Figure 7. Site Analysis: Vegetation samples in PCA space: PC 1 and PC 3. The PCA space displays every sampled date for each vegetation sample to illustrate the phenological range of each vegetation sample in relation to the other samples

The PCA space defined by the PC 1 vs. PC 3 axes (Figure 7) is similar to the PC 1 vs. PC 2 dimension. The space is defined as a cone standing on end, with the tip at zero on both axes and spreading out positively and negatively along the PC 3 axis as PC 1 increases. Most of the sample sites exist in the negative PC 3 region of PCA space.

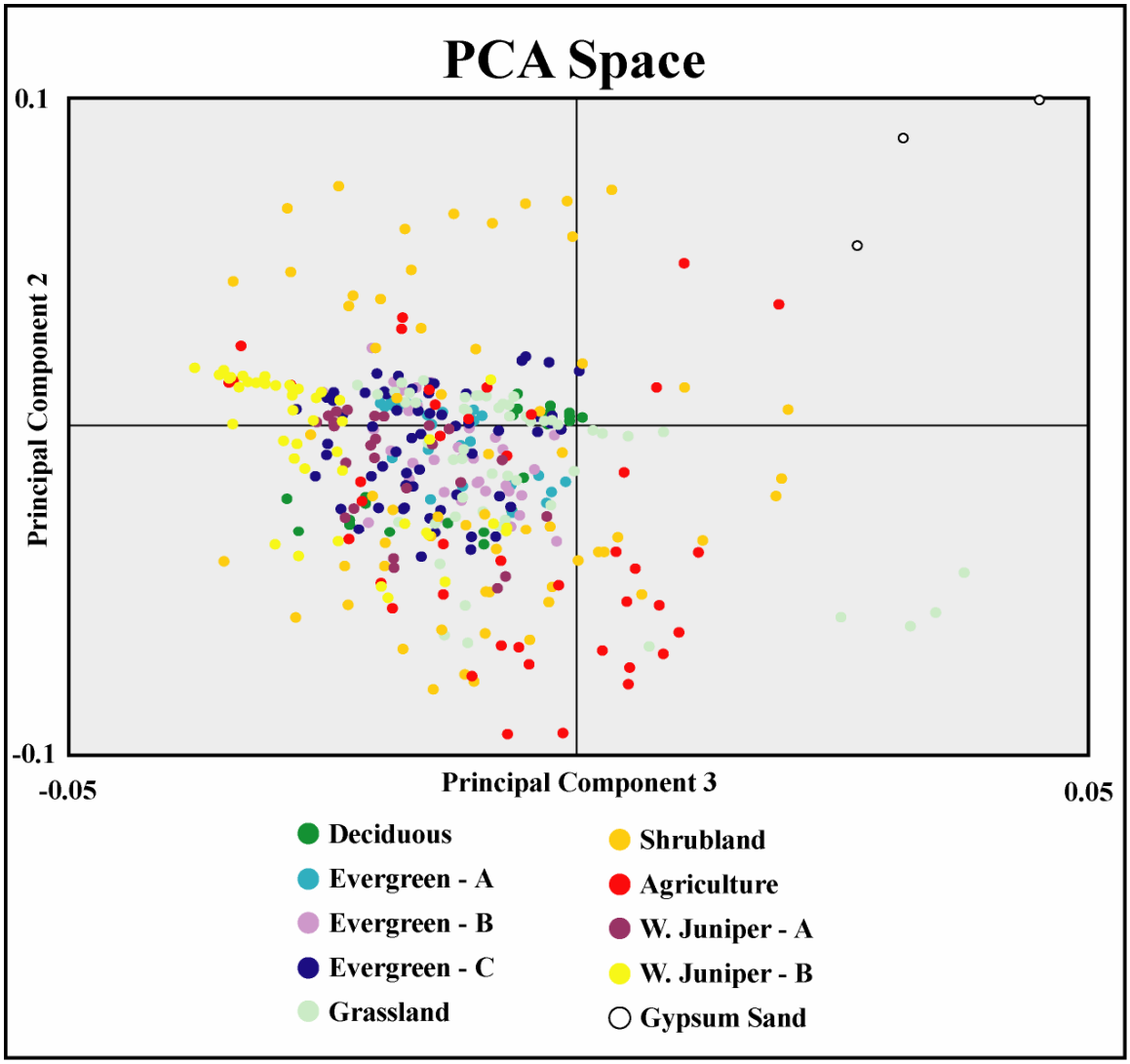

Figure 8. Site Analysis: Vegetation samples in PCA space: PC 2 and PC 3. The PCA space displays every sampled date for each vegetation sample to illustrate the phenological range of each vegetation sample in relation to the other samples

The PCA space defined by the PC 2 vs. PC3 axes (Figure 8) is much less well defined than the previous two dimensions. There is no immediately recognizable

shape or pattern to the spread of samples. There is some clustering of points in the western portion of the data space and some linear clumping of the Western Juniper sites.

Analysis of Principal Component 1

The first principal component varied spatially across samples, temporally across the dates at each sample, and had only positive values. The magnitudes and ranges for PC 1 are presented in Figure 11, reflectance magnitudes and ranges are presented in Figure 9.

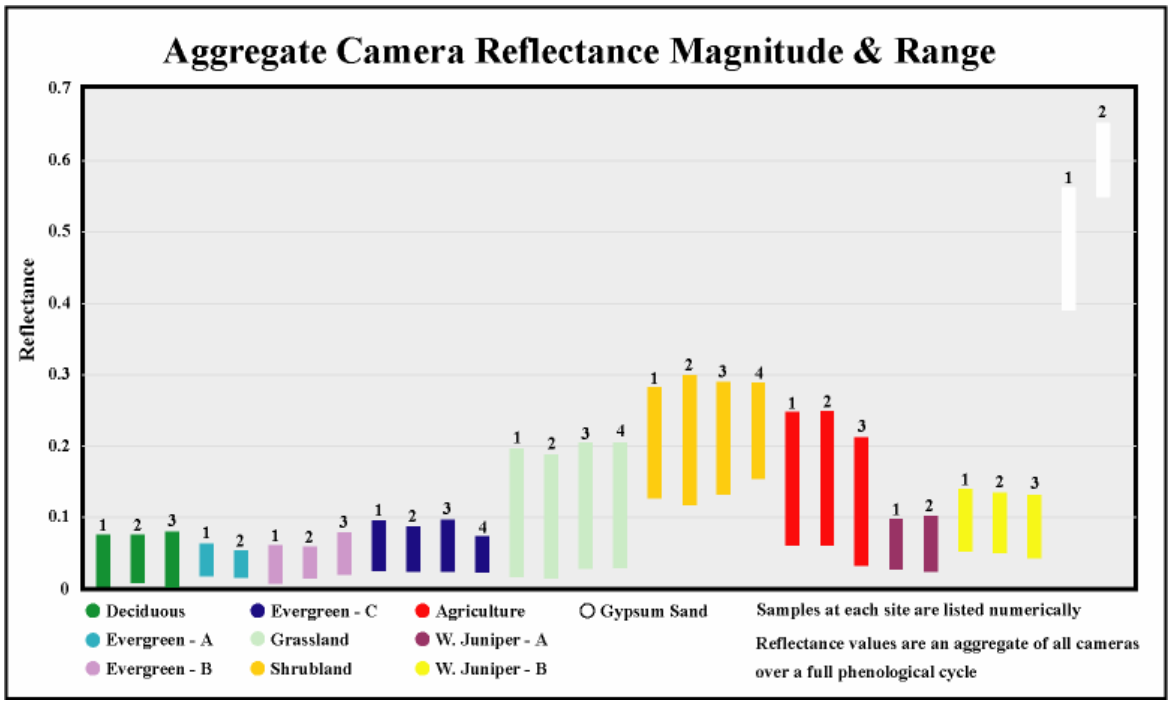

Figure 9. Site Analysis: Aggregate camera reflectance for each vegetation sample. Reflectance ranges represent the highest and lowest value of any camera across every date in the sample

The variation between samples along PC 1 (Figure 11) viewed with the variation in reflectance between samples and sites (Figure 9), shows the clear association between PC 1 value and scene albedo. This correlation of PC 1 with

albedo in reinforced by the similar temporal profiles of PC 1 and mean scene reflectance at each sample (Figure 10, Table 4).

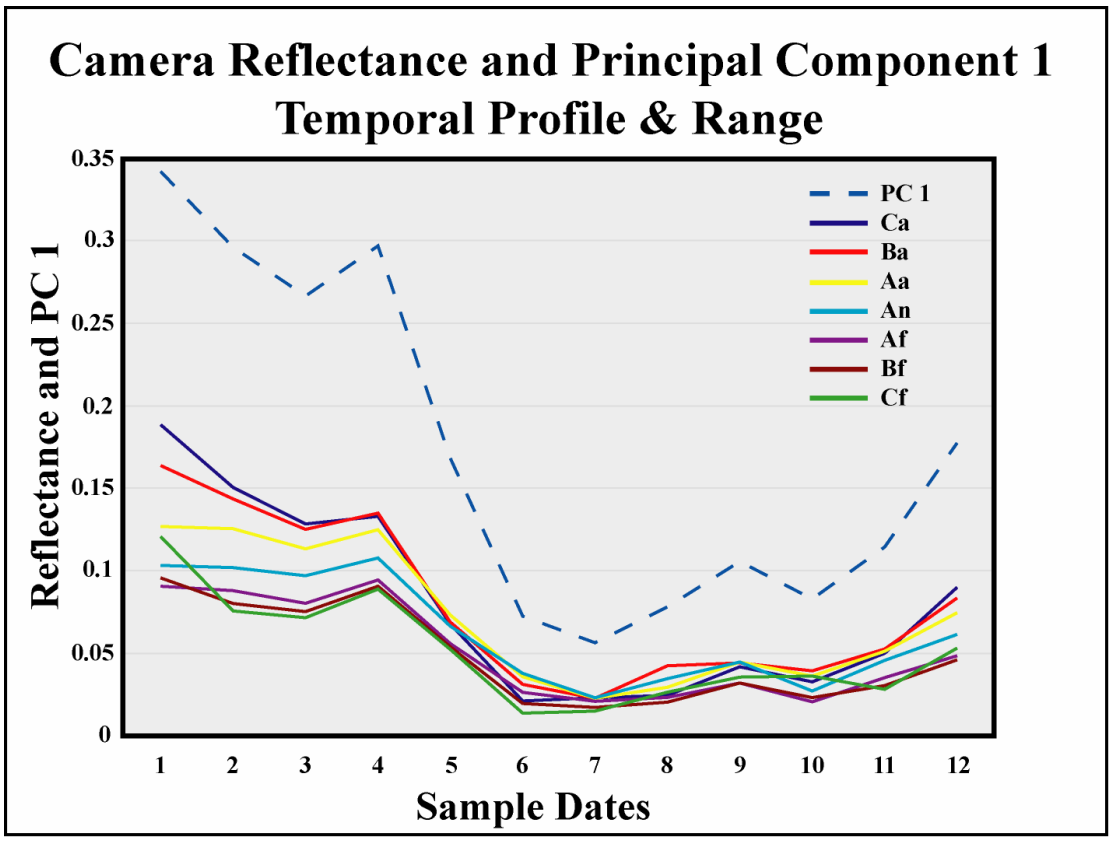

Figure 10. Site Analysis: Temporal profile - camera reflectance and principal component 1 for Grassland sample 2

Table 4. Site Analysis: Temporal profile - camera reflectance and principal component 1 for Grassland sample 2 – sample dates

SAMPLE	DATE		SAMPLE	DATE
1	January/10/2004		7	June/5/2005
2	March/1/2005		8	July/7/2005
3	March/14/2004		9	August/8/2005
4	April/2/2005		10	September/9/2005
5	April/15/2004		11	September/26/2004
6	May/20/2005		12	October/8/2004

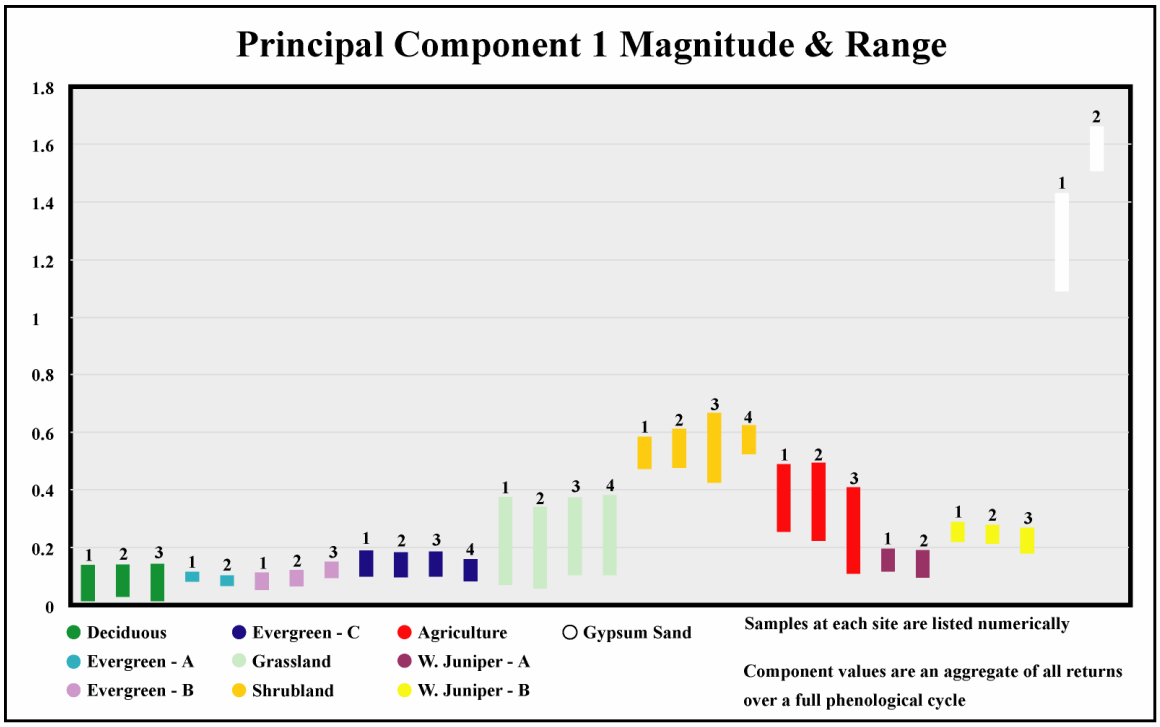

Figure 11. Site Analysis: Magnitudes and range of principal component 1 for each sample in the correlation study sites. Component ranges represent the highest and lowest returns for every date in the sample

To evaluate the relationship of PC 1 with biomass, PC 1 is examined against a measure of vegetation, the NDVI derived from the nadir camera, for each sample of the ten correlation study sites.

Examination indicated a clear inverse relationship between PC 1 and NDVI at nearly every sample. Scatter plots of PC 1 against NDVI are presented for each sample in the Appendix with the regression equations and r^2 values accompanying. PC 1 is presented as the dependent variable and NDVI as the independent variable.

Nearly all of the samples showed a moderate to high inverse correlation with NDVI. The Deciduous samples showed the highest inverse correlation between PC 1 and NDVI of any site with r^2 values of 0.99 at each of the three samples indicating near perfect inverse relationship between NDVI and PC 1. Deciduous sample 1 (Figure 12a) had the highest correlation coefficient of any sample in the study.

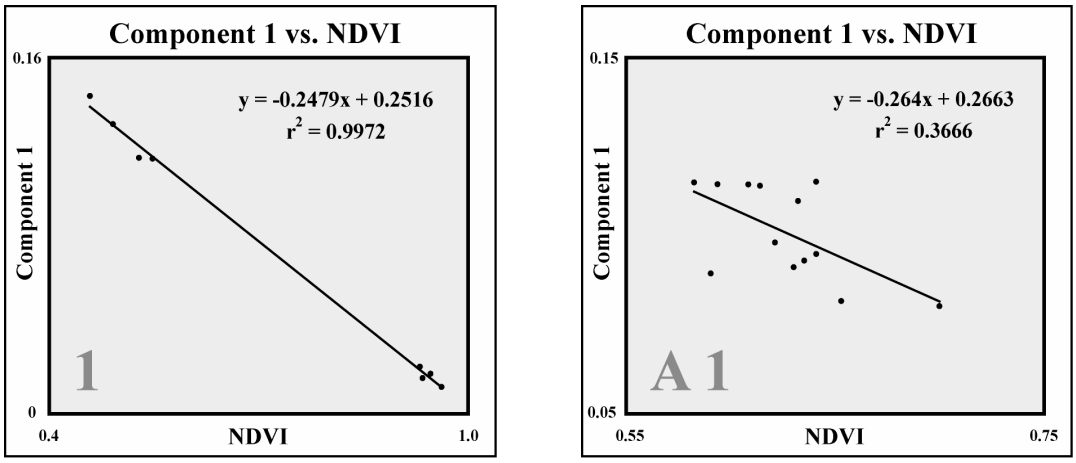

Figure 12 a / b. Site Analysis: .a The plot on the left shows the Deciduous sample 1 correlation plot of NDVI vs. principal PC 1. Deciduous sample 1 had the highest correlation coefficient of any sample from the study sites .b The plot on the right shows the Evergreen – A1 correlation plot of NDVI vs. PC 1. Evergreen A 1 had the lowest correlation coefficient of any sample from the study sites

The three Evergreen sites (A, B, C) showed varying inverse correlation between PC 1 and NDVI by site, and by samples within sites. The Evergreen - A samples had the lowest correlation coefficients as a group of any site, with r^2 values less than 0.38. Site Evergreen - B showed high inverse correlation at two of the samples with r^2 values between 0.85 and 0.89, with the third sample showing very weak inverse correlation with an r^2 value of 0.3. The Evergreen - C site showed modest inverse correlation with r^2 values ranging from 0.68 to 0.79.

The Grassland site showed a high inverse correlation between PC 1 and NDVI with r^2 values ranging from 0.87 to 0.95. An examination of Grassland sample 1 (Figure 13a) revealed a relationship between PC 1 and NDVI that did not seem linear across all the dates sampled. For the months of NDVI < 0.4, PC 1 increased much more than NDVI decreased. A 2nd Order Polynomial line was fit to the data points at each of the four samples to evaluate if the relationship between NDVI and PC 1 could be better explained than with a linear fit (Figure 13b). The 2nd Order Polynomial line did result in higher r^2 values than the linear fit at each sample, but with a marginal increase. Sample 1 showed the highest increase in correlation, with the r^2 value in

increasing just less than 4%: The r^2 values of the remaining 3 samples at the Grassland site increased by approximately 1%.

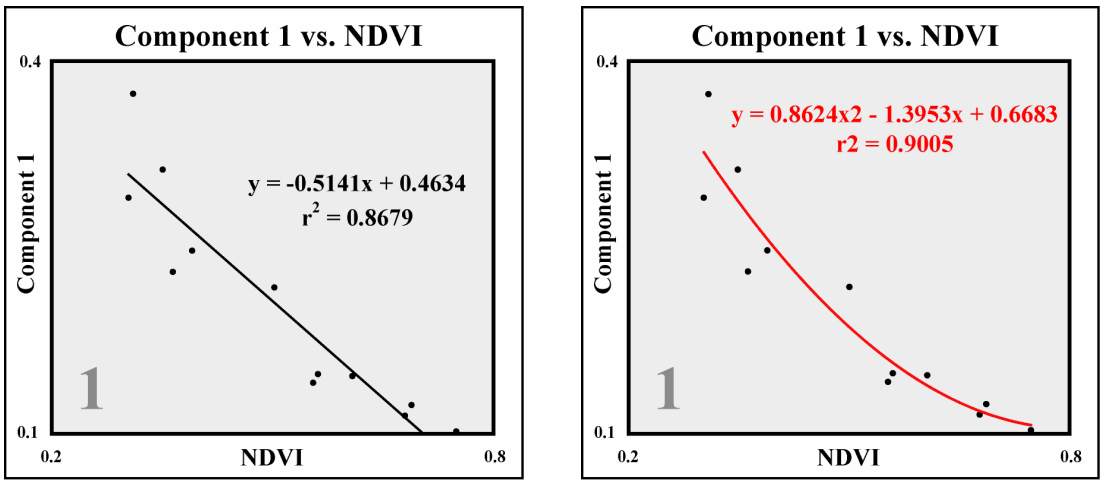

Figure 13 a / b. Site Analysis: .a The plot on the left shows the correlation plot of NDVI vs. PC 1 for Grassland sample 1 with a linear best-fit line .b The plot on the right shows the correlation plot for Grassland sample 1 with a 2nd Order Polynomial best-fit line

The Shrubland samples showed a range of inverse correlation between PC 1 and NDVI depending on the sample. The r^2 values range from a low of 0.38 and 0.54 at samples 1 and 2: to a high of 0.77 and 0.81 at samples 3 and 4.

The Agriculture sites showed a moderate to high inverse correlation between PC 1 and NDVI with r^2 values ranging from 0.87 to 0.89. Sample 2 displayed a pattern that visually appeared to have less of a linear relationship than the other samples. For the months of NDVI < ~= 0.3 the increase in PC 1 was much higher than the NDVI decrease. A 2nd Order Polynomial line was fit to sample 2 and compared against a linear fit. The 2nd Order Polynomial line resulted in a higher r^2 at sample 2 (0.91), than with the linear line (0.88). At Agriculture samples 1 and 3 the relationship between PC 1 and NDVI was decidedly linear with essentially no change in r^2 value at either site between a linear best-fit line or a 2nd Order Polynomial line.

The Western Juniper – A samples had nearly equal high inverse correlation between PC 1 and NDVI with r^2 values of 0.9. Conversely, the Western Juniper – B samples had moderately low to high inverse correlation between PC 1 and NDVI.

Sample B2 had a much lower correlation, r^2 of 0.68, than samples B1 and B3, 0.88 and 0.91 respectively.

The Gypsum Sand site showed a weak inverse correlation between PC 1 and NDVI, with very different correlations for each of the samples with r^2 values of 0.42 and 0.48.

Analysis of Principal Component 2

Examination of the magnitude and range of PC 2 (Figure 14) reveals that the primary variation between samples is in their range of values. The factor loadings of PC 2 (Figure 4) show that the second principal component is a measure of anisotropy, contrasting fore and aft camera reflectance. This variation in camera reflectance is a result of the changing direction and length of shadows affecting the reflectance of the fore and aft cameras.

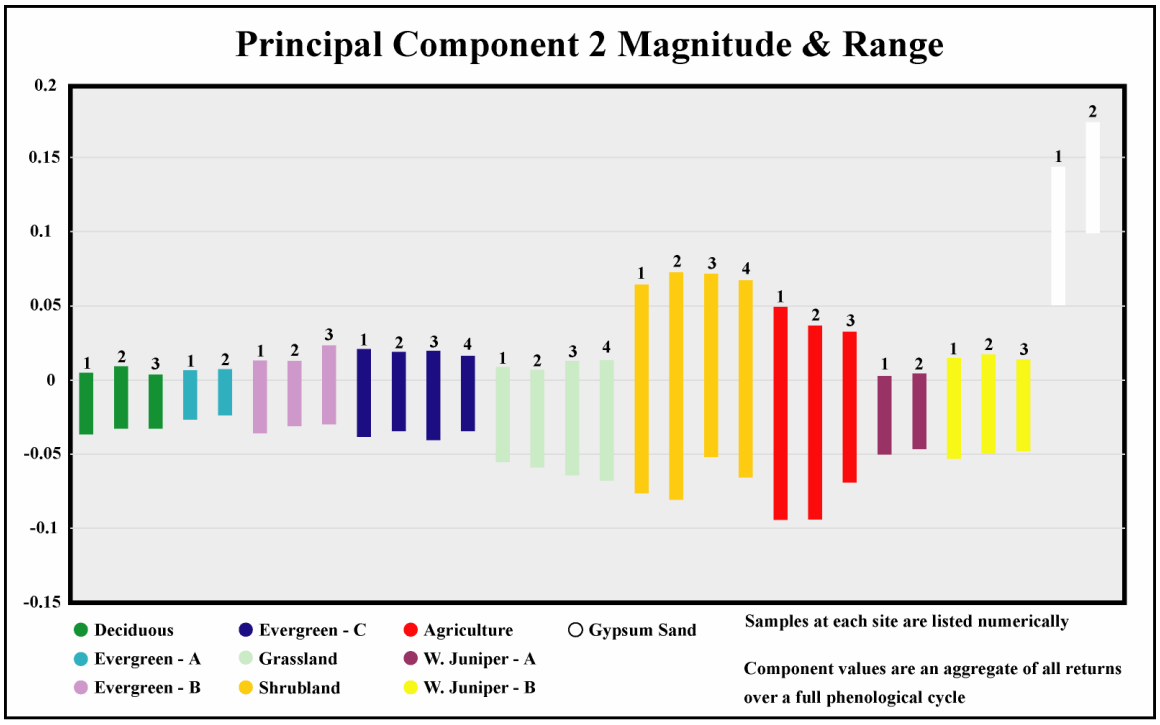

Figure 14. Site Analysis: Magnitudes and ranges of principal component 2 for each sample in the correlation study sites. Component ranges represent the highest and lowest returns for every date in the sample

Examination of the temporal change of PC 2 showed an association between PC 2 and the date of sample (Figure 15, Table 5). For each of the vegetated samples, the dates sampled closest to the Northern Hemisphere Summer Solstice (June 21st) have the highest PC 2 values, and those months closest to the Winter Solstice (December 21st) have the lowest PC 2 values. The range of value for PC 2 for the individual sample is very similar to the range of reflectance of the individual samples, relative to each other.

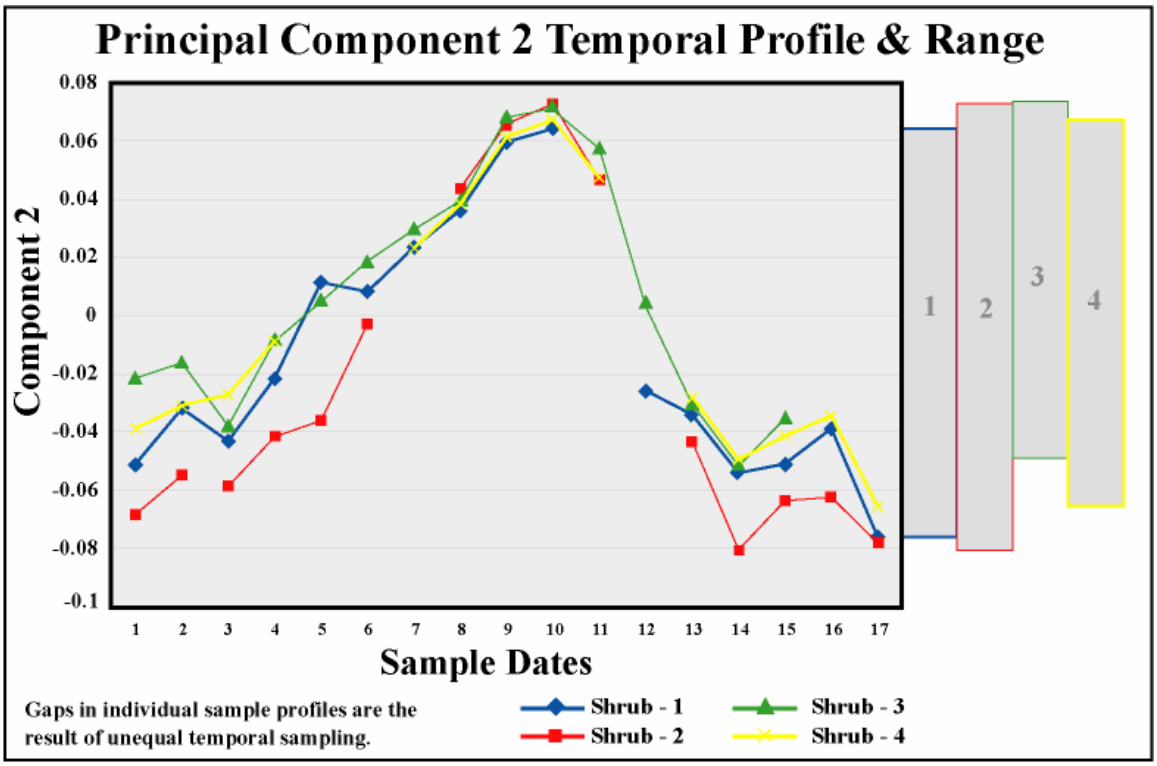

Figure 15. Site Analysis: Shrubland - Principal component 2 temporal profile for samples 1 - 4 over 17 orbits

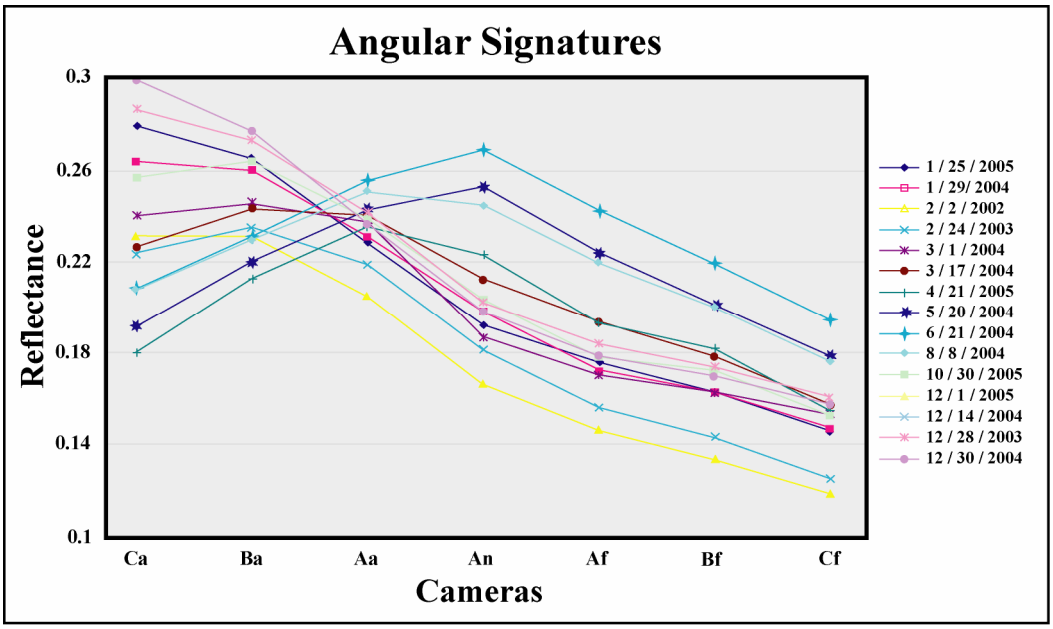

Figure 16. Site Analysis: Shrubland sample 2 - Angular signatures for samples 1

Table 5. Site Analysis: Shrubland sample 2 - Sample dates

SAMPLE	DATE		SAMPLE	DATE
1	January/15/2005		10	June/21/2004
2	January/29/2004		11	August/8/2004
3	February/2/2002		12	October/14/2005
4	February/24/2003		13	October/30/2005
5	March/1/2004		14	December/1/2005
6	March/17/2004		15	December/14/2004
7	April/5/2005		16	December/28/2003
8	April/21/2005		17	December/30/2004
9	May/20/2004			

Examination of the angular signatures of Shrubland – 2 (Figure 16) shows the relationship between the value of PC 2 and the reflectance by MISR camera. Dates sampled furthest from the summer solstice show the highest reflectance in the aft cameras and the lowest reflectance in fore cameras. As the dates sampled grow nearer the summer solstice, aft reflectance drops and fore reflectance increases. For those months nearest the summer solstice the highest reflectance is at camera Aa or nadir, decreasing nearly equally fore and aft. As PC 2 is a linear sum contrasting the aft and fore reflectance, the magnitude of PC 2 increases towards the summer solstice as the aft reflectance drops and the nadir and fore reflectance increases.

PC 2 was examined against solar zenith angle, and the relative azimuth angle between the incident solar radiation and the Ba camera to assess correlation between PC 2 and changing solar illumination. The relative solar azimuth angle is calculated as the angle between the angle of incident radiation and the Ba camera for a given orbit. The Ba camera is used because when comparing multiple orbits on a single MISR Path, the sensor azimuth angle for each camera extracted from the MIANCAGP file varied by orbit. It was desirable to use the camera azimuth angle as close to nadir as possible, and the Ba camera azimuth angles varied less over orbits than the Aa camera azimuth angles.

An examination of scatter plots of PC 2 against the solar zenith angle indicated an inverse relationship between PC 2 and the changing solar elevation. For each sample, scatter plots of PC 2 against solar zenith angle are presented in the Appendix with the regression equations and r^2 values accompanying. PC 2 is presented as the dependent variable and solar zenith angle as the independent variable. Nearly all of the samples showed moderate to very high inverse correlation with changing solar zenith angle. For most samples, r^2 values above 0.9 were found.

All of the samples at Deciduous, Evergreen - A & C, Shrubland (Figure 17a), Agriculture, and Western Juniper – A & B sites had r^2 values over 0.9. The Grassland samples had r^2 values ranging from 0.86 to 0.89.

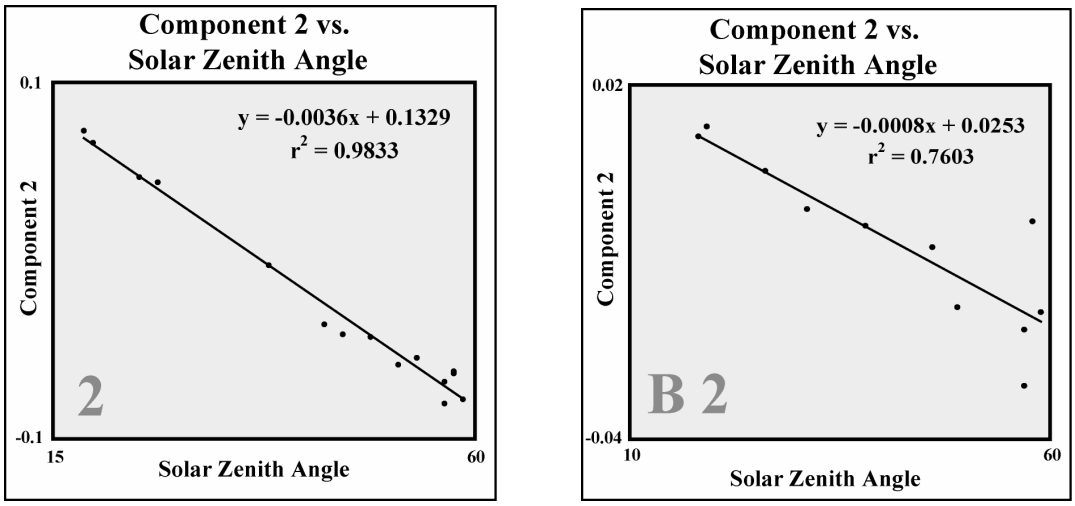

Figure 17 a / b. Site Analysis: .a The plot on the left shows the Shrubland sample 2 correlation plot of solar zenith angle vs. PC 2. Shrubland sample 2 had the highest degree of correlation of any sample .b The plot on the right shows the Evergreen – B sample 2 correlation plot of solar zenith angle vs. PC 2. Evergreen – B2 had the lowest degree of correlation of any sample

The samples at the Evergreen – B site (Figure 17b) showed lower inverse correlation than at any other vegetated site. Correlation coefficients at Evergreen – B ranged from 0.76 to 0.8. The Gypsum Sand samples varied in their amount of correlation. Sample 1, located on uneven ground, showed a weak inverse correlation between Component 2 and the solar illumination angle with an r^2 value of 0.3. Sample 2, located in sand dunes, showed a moderately high inverse correlation with an r^2 value of 0.74.

An examination of scatter plots of PC 2 against the relative azimuth angle indicated an inverse relationship between PC 2 and the relative azimuth angle. For each sample, scatter plots of PC 2 against the relative solar / sensor azimuth angle are presented in the Appendix with the regression equations and r^2 values accompanying. PC 2 is presented as the dependent variable and relative azimuth angle between sun and sensor as the independent variable.

A moderately high, to high inverse correlation existed for most samples, but with more variation in the correlation between samples than the correlation between samples for PC 2 against the solar zenith angle. Correlation coefficients for PC 2

against the relative azimuth angle were also generally lower for all samples than the correlation values for PC 2 against solar zenith angle. Typical r^2 values at samples ranged from 0.85 to 0.95.

The Grassland samples had by far the widest range of correlation coefficients of any site or sample. Grassland sample 2 has the lowest r^2 value at 0.54 (Figure 18a), followed by Sample 3 at 0.68. Sample 4 shows moderate correlation with an r^2 of 0.74. Sample 1 has the highest correlation with an r^2 value of 0.85.

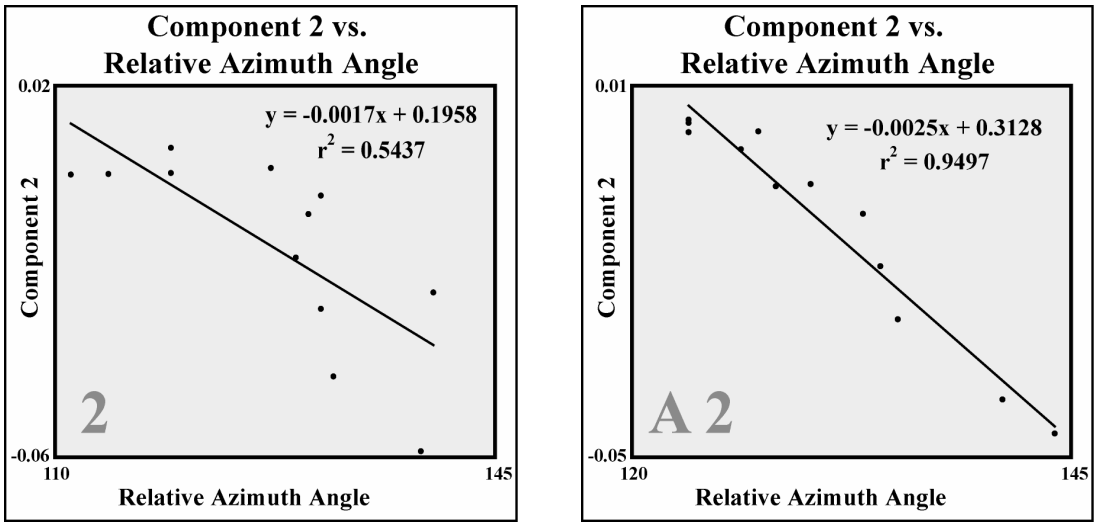

Figure 18 a / b. Site Analysis: .a The plot on the left shows the Grassland sample 2 correlation plot of relative azimuth angle vs. PC 2 .b The plot on the right shows the Western Juniper sample A2 correlation plot of relative azimuth angle vs. PC 2

The Evergreen – A and Western Juniper – A & B sites all showed the highest correlation between PC 2 and relative azimuth (Figure 18b) and also showed the least amount of variation between samples of any other site. All of the samples for sites Evergreen – A and Western Juniper – A had r^2 values of 0.95. The Western Juniper – B samples had r^2 values ranging from 0.93 to 0.94.

The Evergreen – C and Shrubland sites had inverse correlations nearly as high as for the Evergreen – A and Western Juniper sites, and showed more variation between samples at each site. The Shrubland samples had a wider range or r^2 values,

from 0.87 to 0.92 than did the Evergreen – C samples which had r^2 values ranging from 0.86 to 0.89.

The Deciduous, Evergreen - B and Agricultural sites showed high inverse correlation between PC 2 and relative azimuth, with slightly lower r^2 values and more variation between samples than for the other sites of high inverse correlation. The r^2 values of the three Deciduous samples ranged from 0.81 to 0.92. The Evergreen – B sample r^2 values ranged from 0.73 to 0.88. The Agricultural samples ranged from 0.75 to 0.8.

The Gypsum Sands site showed considerable differences in the inverse correlation between PC 2 and the relative azimuth angle. Sample 1 shows very low correlation with an r^2 value of 0.49. Sample 2 has a moderate correlation with an r^2 value of 0.75.

Analysis of Principal Component 3

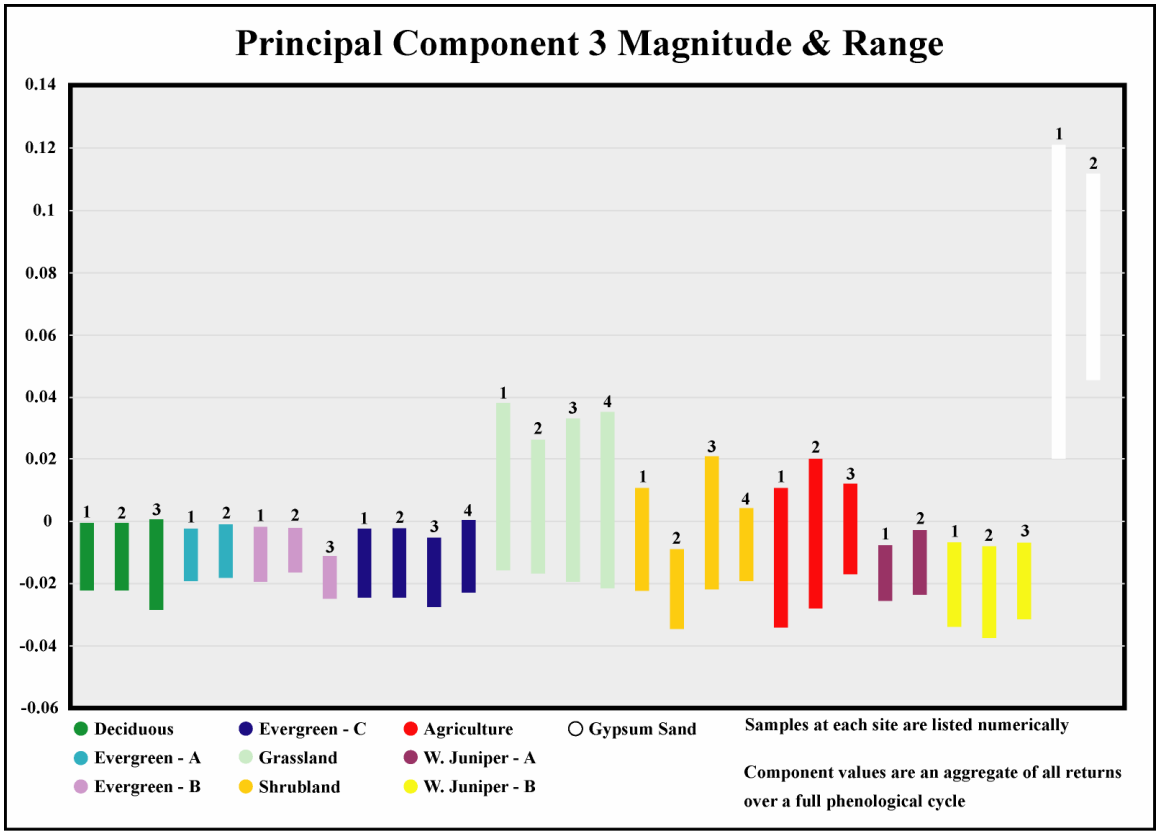

Figure 19. Site Analysis: Magnitudes and range of PC 3 for each vegetation sample. Component ranges represent the highest and lowest returns for every date in the sample

The shape of the PCA space as defined by PC 1 vs. PC 3 (Figure 7) and PC 2 vs. PC 3 (Figure 8) shows no clearly discernable pattern to the placement of points along the PC 3 axis. No correlation could be found between PC 3 and any commonly used vegetation metric. Examination of the ranges and intensity of PC 3 (Figure 19), the temporal profiles of PC 3 however, suggests intrinsic differences between the sites. The Grassland samples, for example, have the broadest range of value and the highest absolute value en masse than any other vegetated sample. All of the sites with trees have only negative PC 3 values. The Agriculture samples show similar temporal profiles with the same high intensity spike in value on May 20, 2004. Even though it explains less than 1% of the variance, PC 3 may contain useful information.

Phenology in PCA Space

The phenological cycle of vegetation is most visible in the PC 1 vs. PC 2 PCA space. The sites with the most marked seasonal changes in cover, Deciduous, Grassland, and to a less extent, Agriculture, have a shape in PCA space distinct from the sites that have less marked seasonal changes: Evergreen, Western Juniper, and Shrubland.

Examination of a Deciduous sample in the PC 1 vs. PC 2 space (Figure 20) illustrates this cycle. The months of low reflectance are the months when the canopy of a deciduous forest would be the fullest. During this leaf-on period, the chlorophyll in the leaves would be absorbing the maximum amount of red and blue light (Curran 1983). PC 1 drops, and PC 2 increases towards the solstice. Conversely, during the winter, the deciduous trees would be in a leaf-off state with more ground to reflect radiation and less leaf cover to absorb resulting in higher reflectance, with PC 1 increasing as reflectance increased and PC 2 decreasing towards the winter solstice.

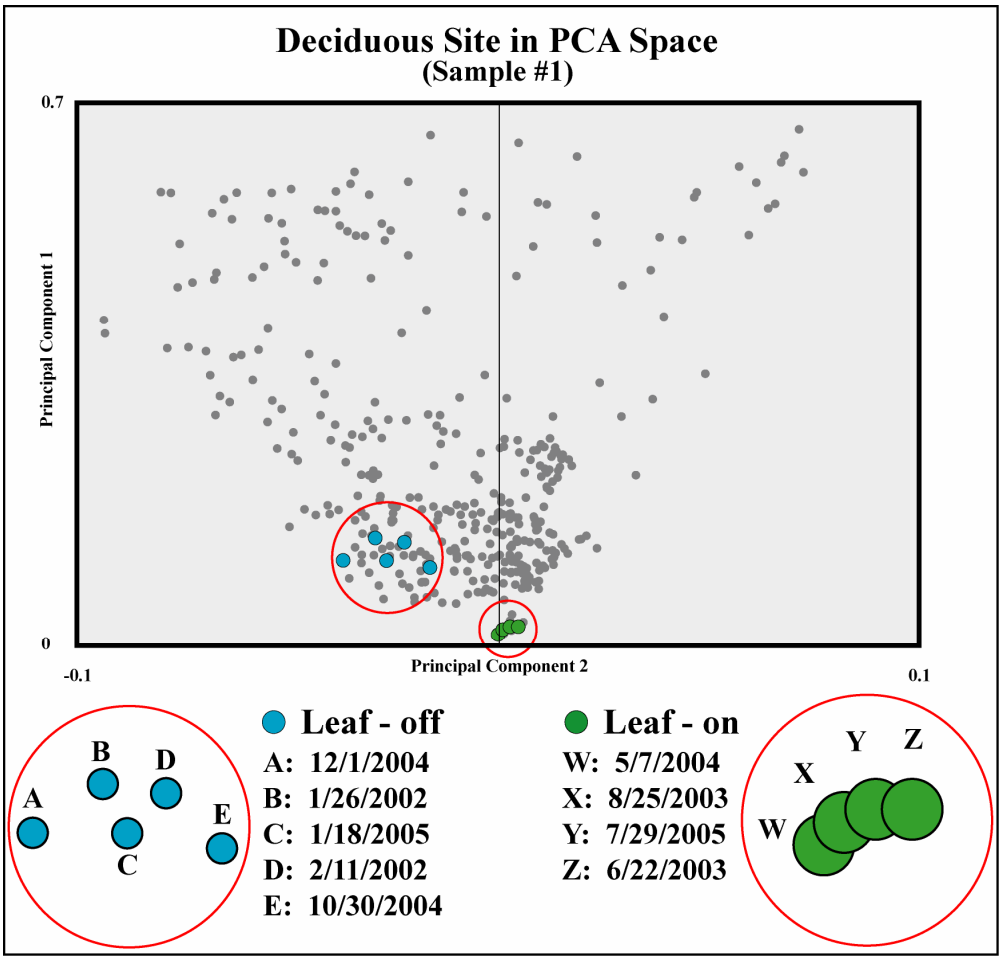

Figure 20. Phenology of Deciduous sample 1 in PC 1 vs. PC 2 space. Nine sample dates are displayed in the PCA scatter window indicating five dates of leaf-off (blue circles on the left) and four dates of leaf-on (green circles on the right)

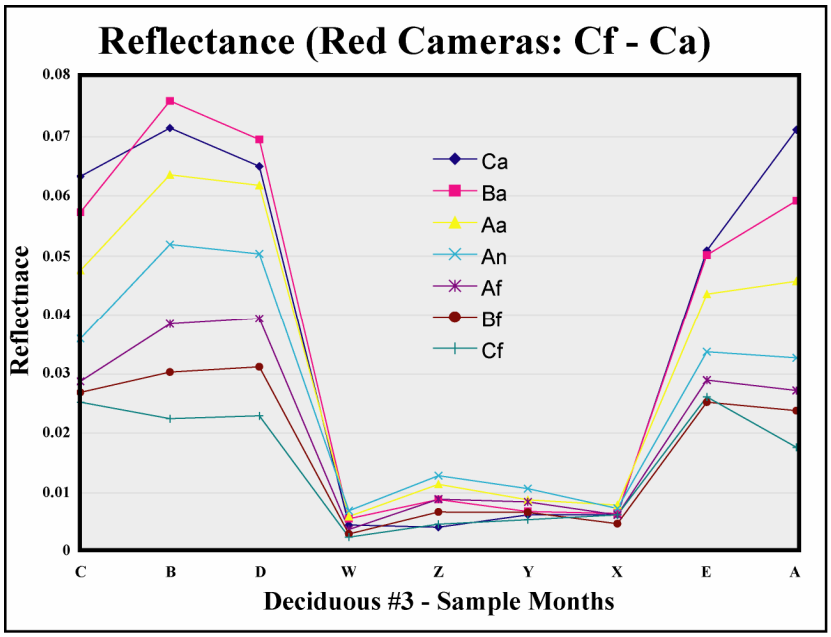

Figure 21. Site Analysis: Angular reflectance of Deciduous sample 1

For the Deciduous samples, the phenological cycle through PCA space leads to a clustering of points in either the leaf-on or leaf-off state. This is due partially to the temporal resolution of Deciduous sample 3, and to the extreme drop in reflectance during the leaf-on state of the samples (Figure 21). Dates that have very low reflectance cluster near the tip of the M-Cone space with positive PC 2 values and very low PC 1 values; these are the leaf-on dates. Dates with higher reflectance values are located in PCA space at lower PC 2 value and higher PC 1 value; these are the leaf-off dates. The value of PC 2 is tied to the solar illumination and the date of the sample, but there is a margin of error. While it was not always the case, the Deciduous Sample 1 had the highest PC 2 value on the date nearest the summer solstice (point Z, leaf-on region of figure X). This does not hold in the leaf-off points where point A has a lower PC 2 return than point D even though point A is 20 days removed from the solstice, and point D is ten. This variation is illustrative of the noise associated with principal component values.

Effects of Topography on Principal Components 1 and 2

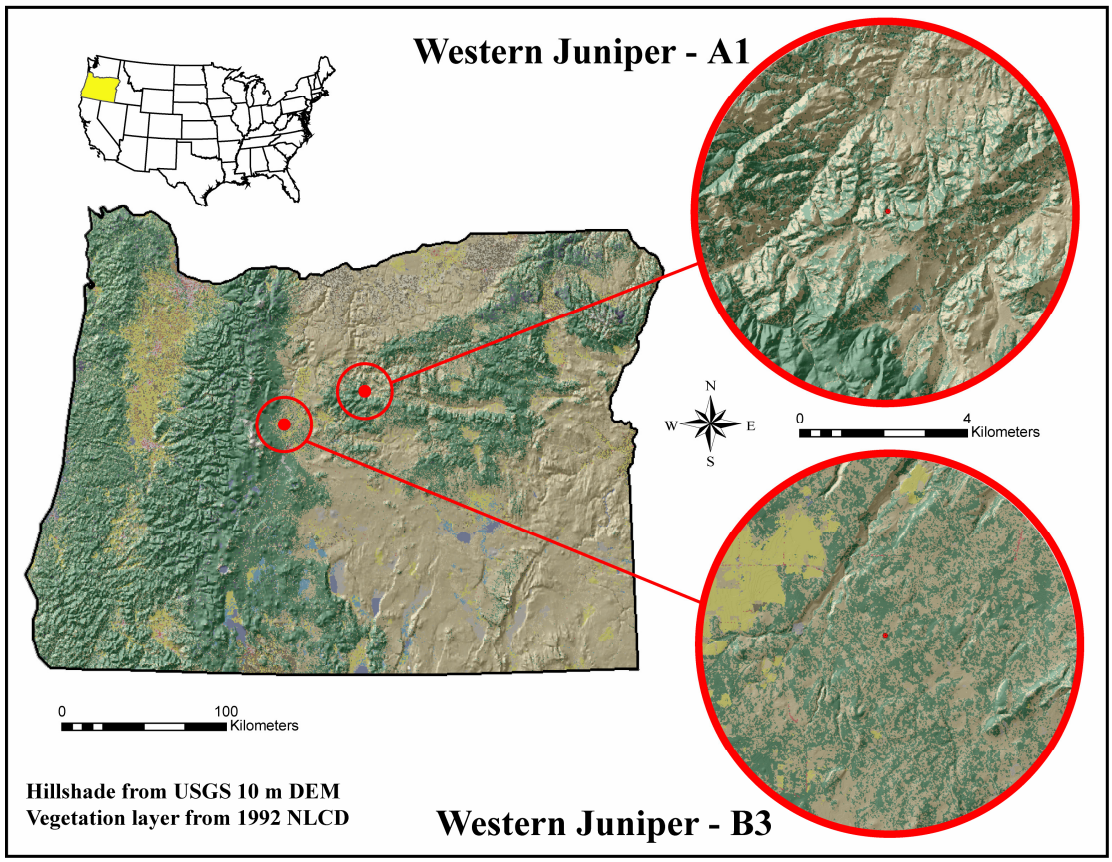

Figure 22. Effects of topography: Site overview map

Table 6. Effects of Topography: Sample dates and orbits

SITE	MONTH	ORBIT		SITE	MONTH	ORBIT
1	4/22/2004	23117		7	8/15/2005	30107
2	5/27/2005	28942		8	8/28/2004	24981
3	4/11/2004	24282		9	8/31/2005	30340
4	7/14/2005	29641		10	9/27/2003	20088
5	7/27/2005	24515		11	10/13/2003	20321
6	7/30/2005	29874				

To assess the possible effects of topography of the principal components, two samples from the Western Juniper – A and B sites in west-central Oregon were examined (Figure 22, Table 6). Sample A1 is from rugged terrain, and B3 is from flat terrain. The two samples are located approximately 90 kilometers apart. The samples were selected from the Western Juniper sites because these sites offered a very long temporal sample, is dominated by phenologically invariant vegetation – western juniper, had similar percentages of land cover (Table 7) and offered topographically different profiles.

Table 7. Effects of Topography: MODIS VCF estimates of vegetation cover

Western Juniper	% Tree	% Non-tree	% Bare
A1	19	54	27
B3	18	58	24

An examination of a 10-m (1/3 Arc Second) DEM derived slope grid of each site showed the Juniper – A1 sample to be on fairly rugged terrain with slopes of approximately 25 degrees and the Juniper – B3 sample to be on relatively flat, undulating terrain, with slopes of less than 5 degrees. To temporally match each site to the same dates of acquisition, August 10th, 2003 was removed from A1 and March 8th, 2005, June 12th, 2005, and September 29th, 2004 were removed from B3.

The temporal profile of mean reflectance is similar between A1 and B3, with B3 having a consistently higher reflectance than A1, but a similar range (Figure 23). The difference in the range of mean reflectance at each site is less than 1%. However, the range of value covered by the reflectance of all cameras for each date is very different between samples (Figure 9). The range of reflectance when all camera reflectance is accounted for is 27% greater at B3 than at A1.

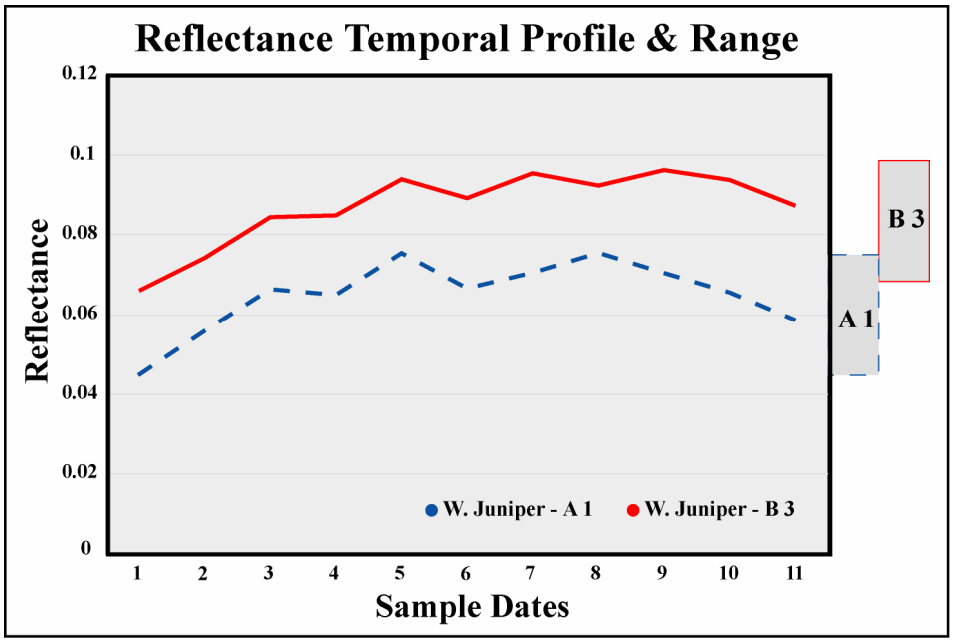

Figure 23. Effects of topography: Aggregate reflectance temporal profile for samples A1 and B3 over 11 orbits

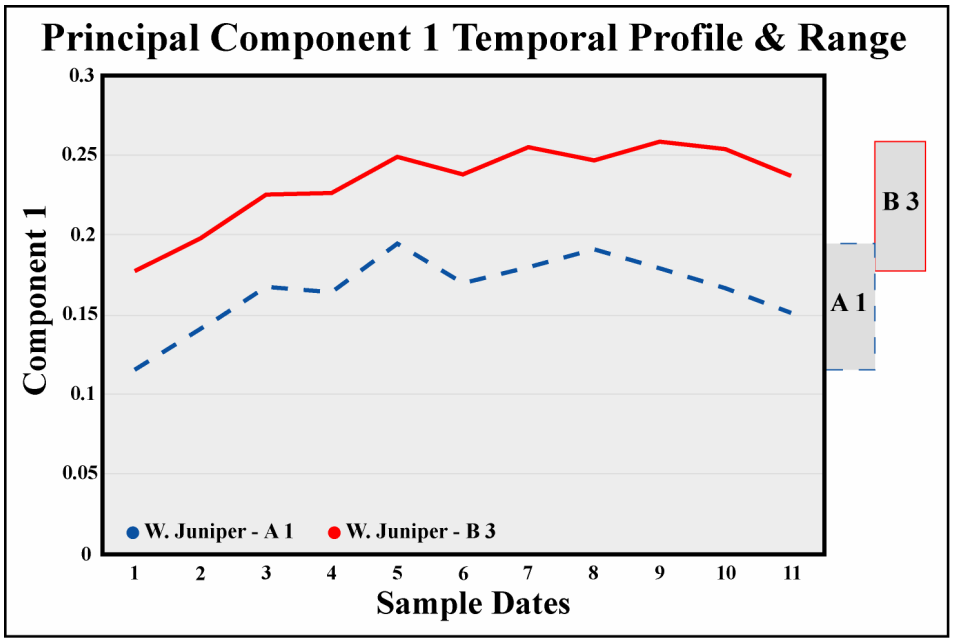

Figure 24. Effects of topography: PC 1 temporal profile for samples A1 and B3 over 11 orbits

The relationship of PC 1 between samples A1 and B3 (Figure 24) is much like the relationship of mean reflectance between A1 and B3 (Figure 23). The PC 1 temporal profile is very similar between samples, with B3 consistently higher value than A1. The range of PC 1 is nearly identical between samples: < 2% difference between A1 and B3.

The NDVI at site A1 was consistently higher than the NDVI at B3, and the range of NDVI at A1 was 105% higher than at B3 (Figure 25). There is high inverse correlation between Component 1 and NDVI at both samples with an R^2 value of 0.9 at A1 and 0.96 at B3 (Figure 26 a / b).

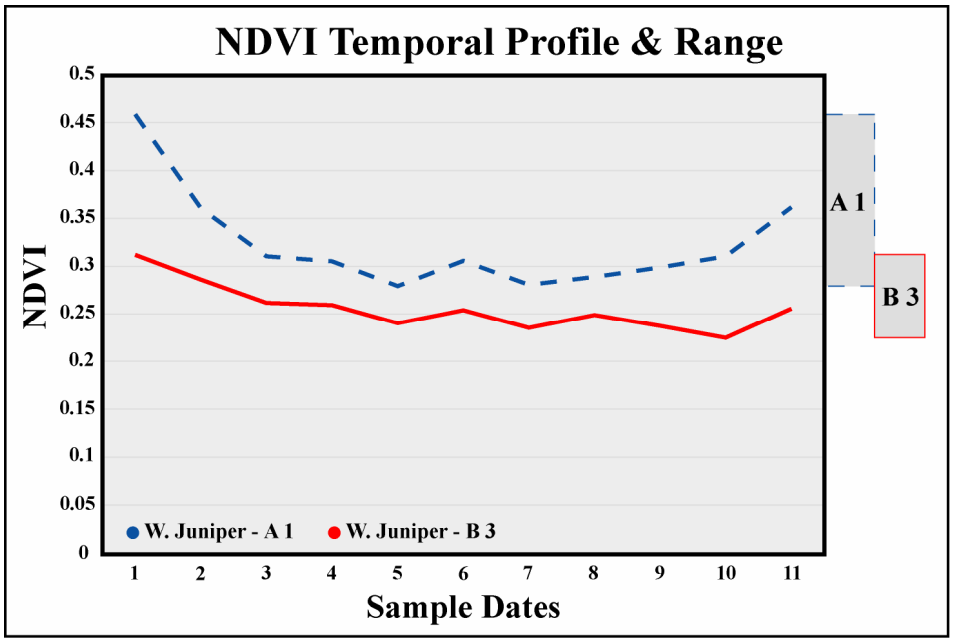

Figure 25. Effects of topography: NDVI temporal profile for samples A1 and B3 over 11 orbits

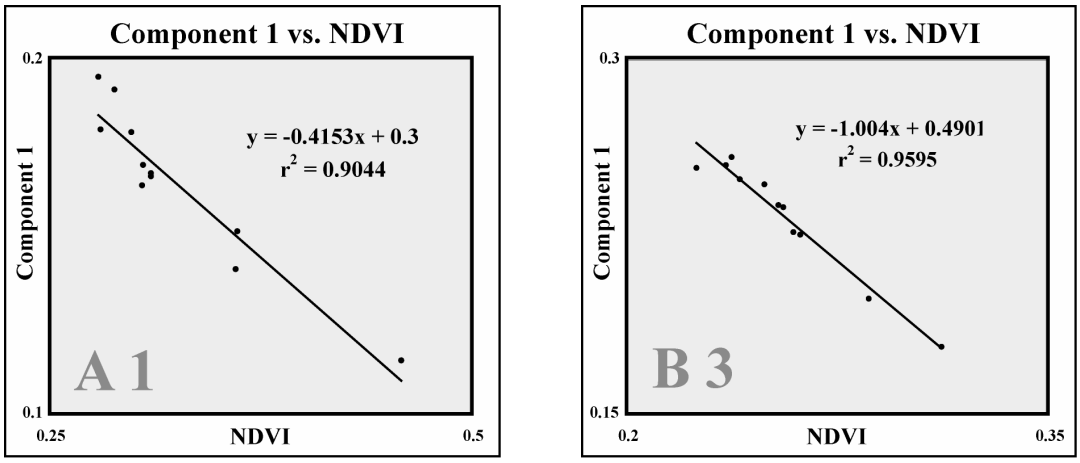

Figure 26 a / b. Effects of topography: .a The plot on the left shows the correlation plot of NDVI vs. PC 1 for sample A1 .b The plot on the right shows the correlation plot of NDVI vs. PC 1 for sample B3

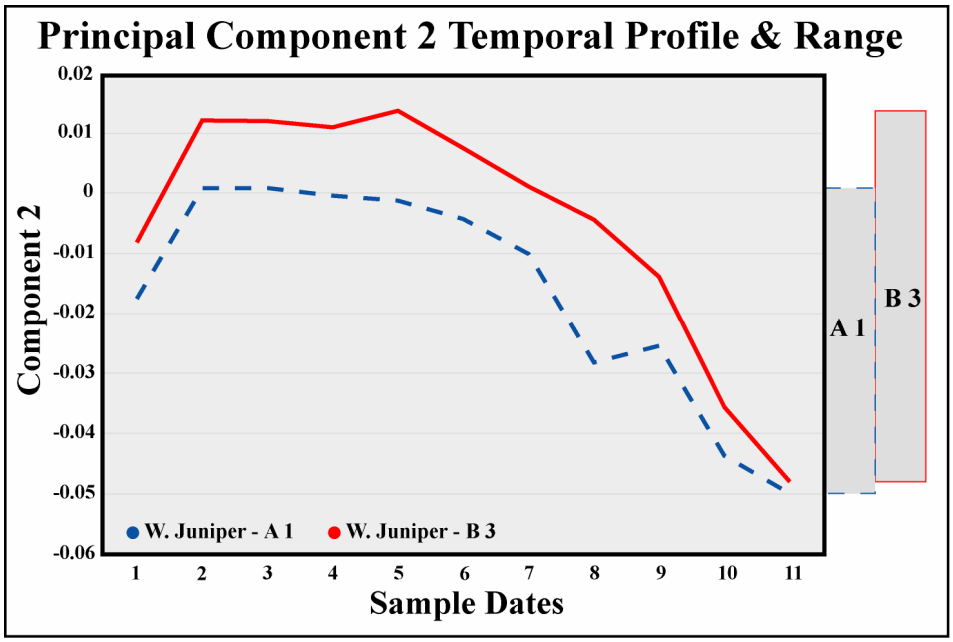

Figure 27. Effects of topography: Principal component 2 temporal profile for samples A1 and B3 over 11 orbits

Like PC 1, the magnitude of PC 2 was higher at sample B3 than A1 (Figure 27), but PC 2 had greater variation over time than PC 1. The temporal profile of PC 2 for both samples showed distinct differences between dates, with spikes of magnitude in each sample that were not reflected in the other sample at the same date. The range of PC 2 was also much greater at B3, 21% higher than at A1. Examination of the temporal profiles of both samples showed that that PC 2 increased in value towards the summer solstice, peaked after the solstice on July 27, 2005 and decreased away towards the winter solstice.

At samples A1 and B3 there is nearly equal high inverse correlation between PC 2 and solar zenith angle (Figure 28) and PC 2 and the relative azimuth angle (Figure 29). The correlation between PC 2 and solar zenith angle at sample A1 has an r^2 value of 0.97, and sample B3 has an r^2 value of 0.96. The correlation between PC 2 and the relative solar azimuth angle is equal for samples A1 and B3 with r^2 values of 0.95 at each sample.

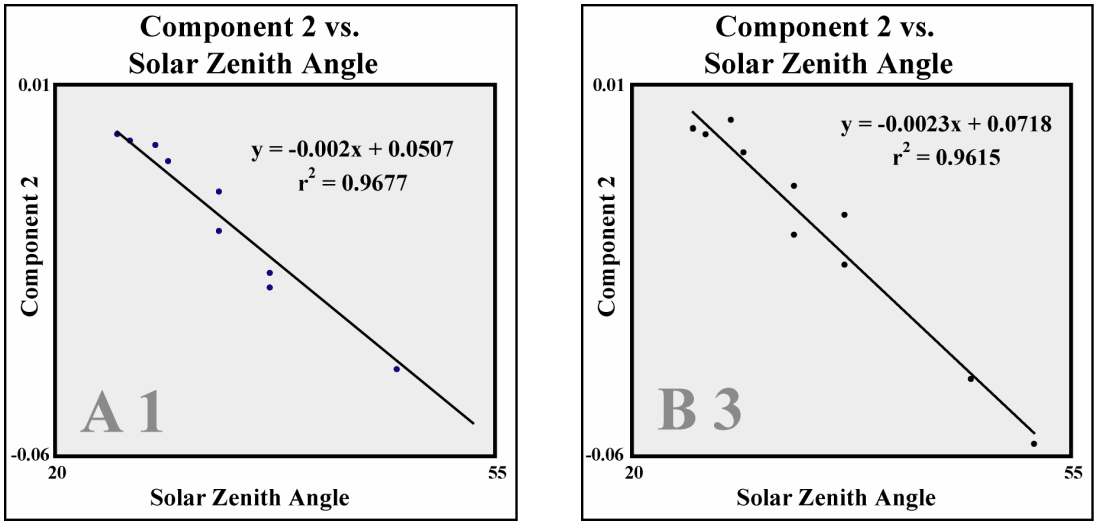

Figure 28 a / b. Effects of topography: .a The plot on the left shows the correlation plot of solar zenith angle vs. PC 2 for sample A1 .b The plot on the right shows the correlation plot of solar zenith angle vs. PC 2 for sample B3

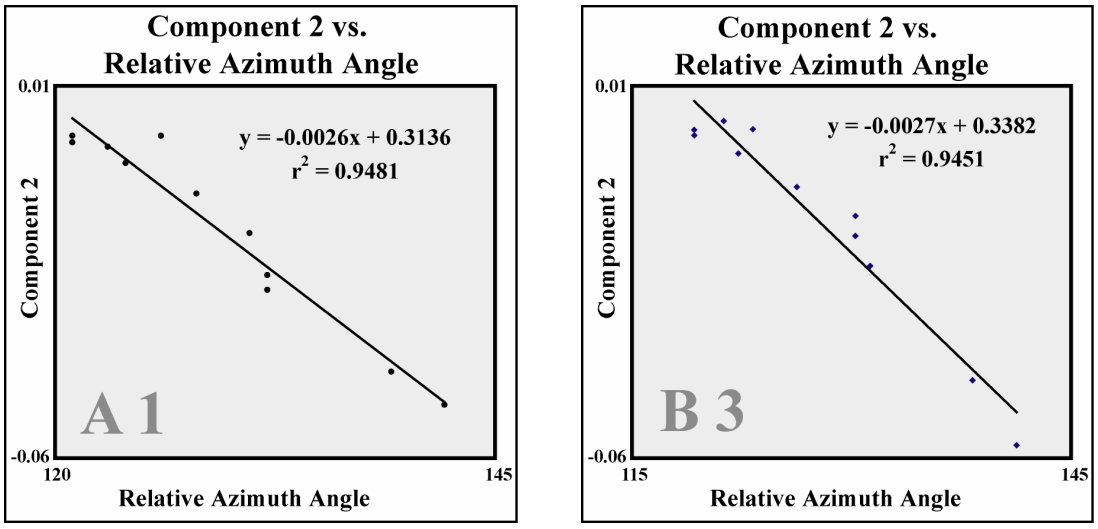

Figure 29 a / b. Effects of topography: .a The plot on the left shows the correlation plot of relative solar / sensor azimuth angle vs. PC 2 for sample A1 .b The plot on the right shows the correlation plot of relative solar / sensor azimuth angle vs. PC 2 for sample B3

Effects of Vegetation Density on Principal Components 1 and 2

Evergreen Site

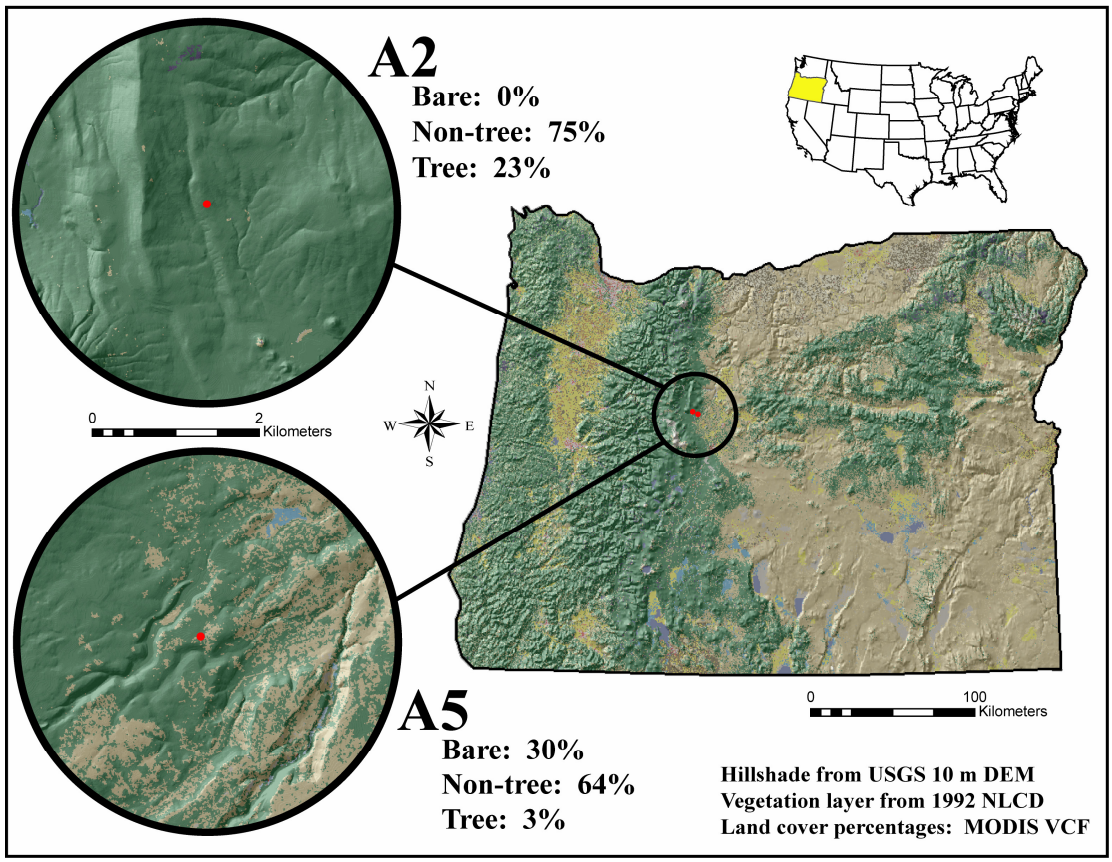

Figure 30. Vegetation density effects - Evergreen: Site overview map

Table 8. Vegetation density effects - Evergreen: Sample dates and orbits

Sample	Date	Orbit		Sample	Date	Orbit
1	3/8/2005	27777		8	7/27/2004	24515
2	4/22/2004	23117		9	7/30/2005	29874
3	5/27/2005	28942		10	8/15/2005	30107
4	6/12/2005	29175		11	8/31/2005	30340
5	6/25/2004	24049		12	9/27/2003	20088
6	7/11/2004	24282		13	10/13/2003	20321
7	7/14/2005	29641				

Two samples of ponderosa pine from central Oregon were selected to assess the effects of varying density of vegetation cover on principal components 1 and 2 (Figure 30, Table 8). Samples were selected to vary in percent tree cover and bare ground, while having near similar percentages non-tree cover (Table 9). Sample Lat-A5 has almost no tree cover, about similar percent of non-tree vegetation as Lat-A5, and significantly more bare ground. The slope at each sample is less than 5º to minimize any topographic effect.

Table 9. Vegetation density effects - Evergreen: MODIS VCF estimates of vegetation cover

Evergreen Sample	% Tree	% Non-tree	% Bare
A2	43	54	0
A5	3	64	30

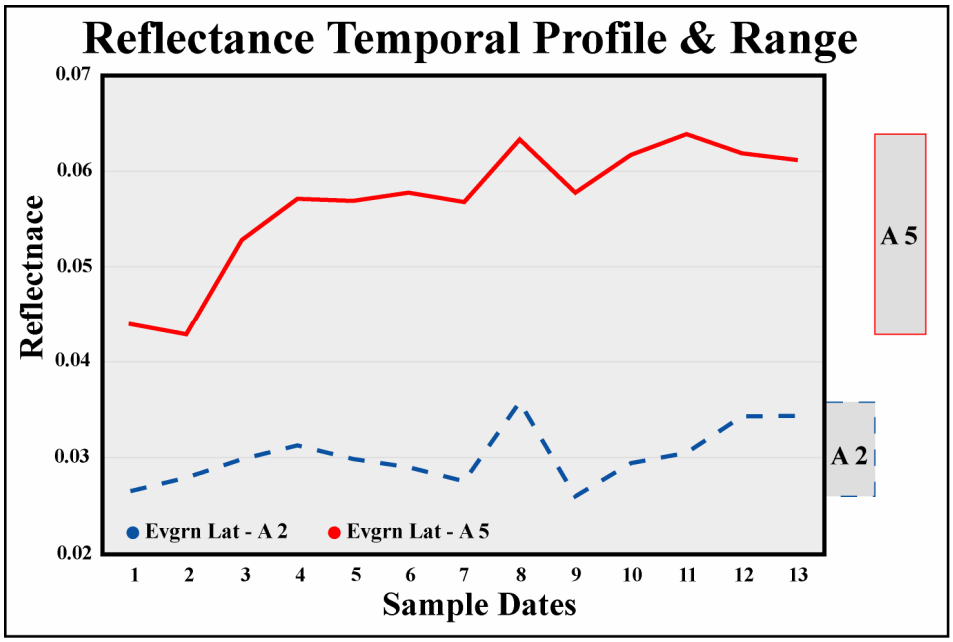

Figure 31. Vegetation density effects - Evergreen: Aggregate reflectance temporal profile for samples Lat-A2 and Lat-A5 over 13 orbits

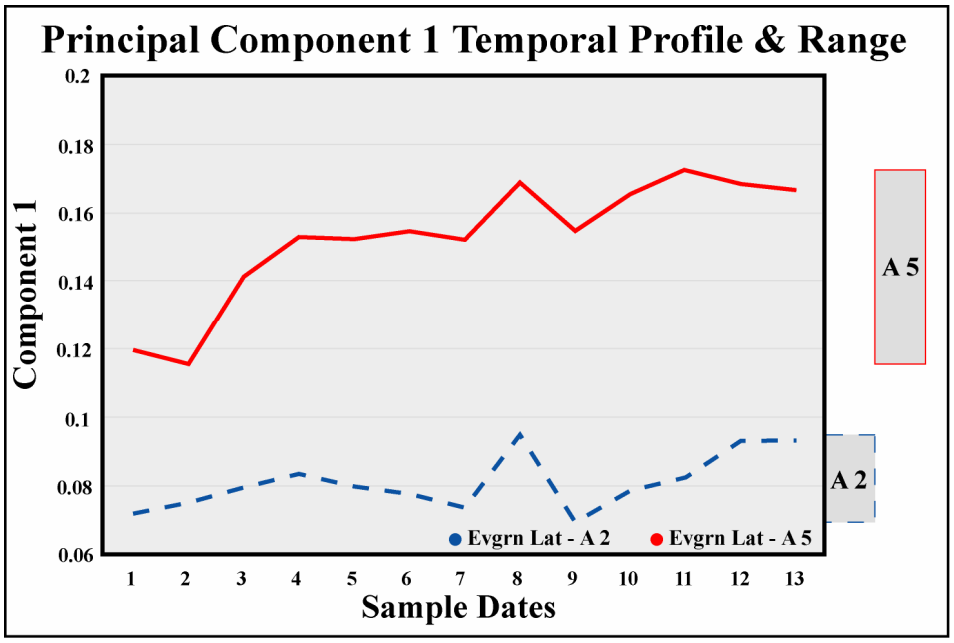

Figure 32. Vegetation density effects - Evergreen: Principal component 1 temporal profile for samples Lat-A2 and Lat-A5 over 13 orbits

The mean reflectance is 86% higher at Lat-A5 than Lat-A2, and the range of mean reflectance is approximately 110% greater at Lat-A5 than Lat-A2 (Figure 31). The temporal profiles of mean reflectance for each sample were similar, with the primary difference between the two samples being the greater range of mean reflectance at Lat-A5 and the higher magnitude of reflectance at Lat-A5.

The PC 1 value at each date is significantly higher at Lat-A5. The range of values for PC 1 is approximately 123% higher at Lat-A5 (Figure 32). The temporal profiles for reflectance and PC 1 value for samples Lat-A2 and Lat-A5 are very similar in variation over time, as are the relative magnitudes between samples, and the relative range of return between the samples.

The NDVI (Figure 33) is consistently higher at sample Lat-A2 than Lat-A5 for every date sampled, averaging 40% higher NDVI at Lat-A2 than Lat-A5. There is less than 1% difference in the range of NDVI between samples Lat-A2 and Lat-A5.

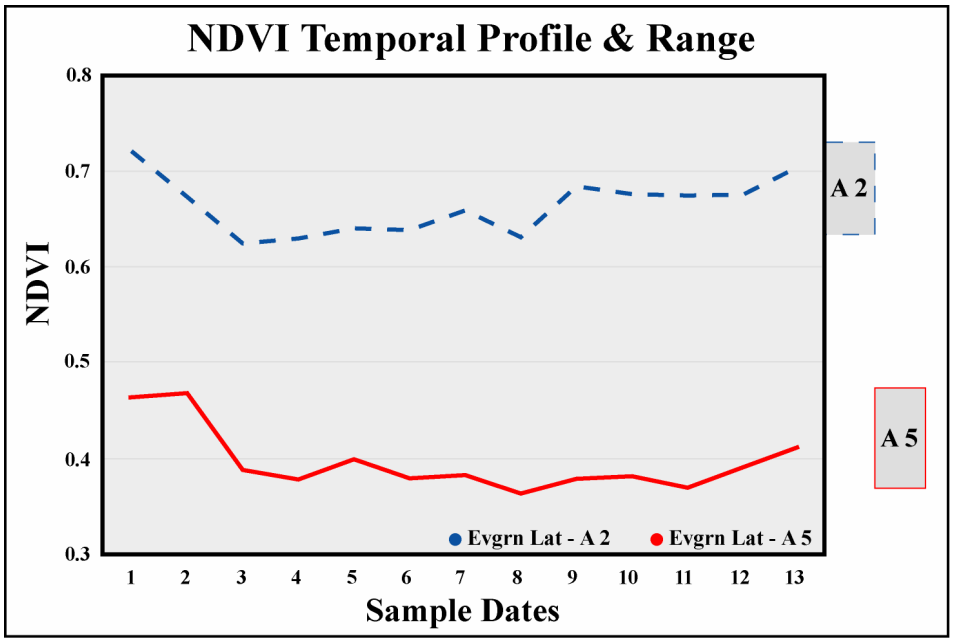

Figure 33. Vegetation density effects - Evergreen: NDVI temporal profile for samples Lat-A2 and Lat-A5 over 13 orbits

There is essentially no correlation between PC 1 and NDVI at sample Lat-A2 as the r^2 value is 0.3 (Figure 34a). There is a moderate inverse correlation between PC 1 and NDVI at sample Lat-A5 with an r^2 of 0.7 (Figure 34b).

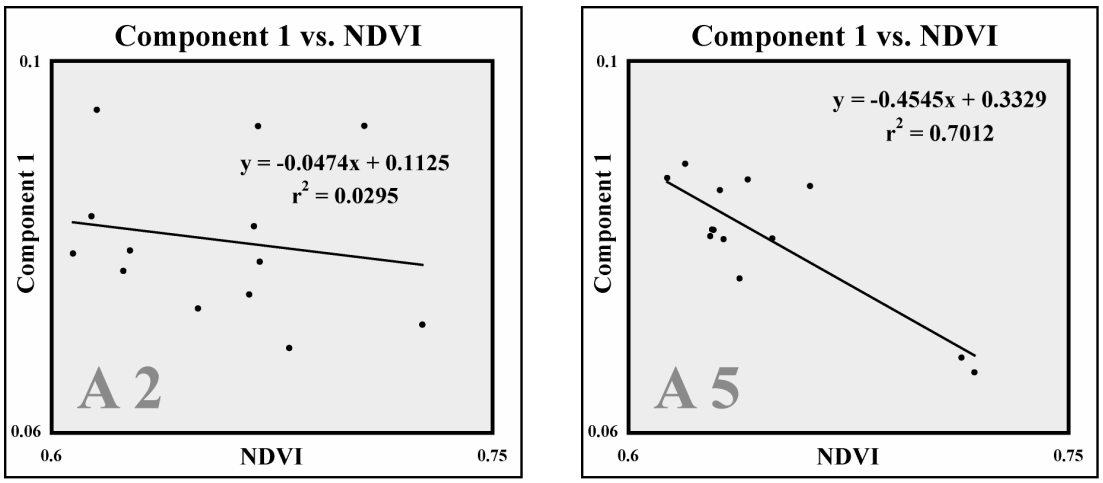

Figure 34 a / b. Vegetation density effects - Evergreen: .a The plot on the left shows the Lat-A2 correlation plot of NDVI vs. PC 1 .b The plot on the right shows the Lat-A5 correlation plot of NDVI vs. PC 1

The relationship between PC 2 at Lat-A2 and Lat-A5 is very different than the relationship of PC 1 between samples (Figure 35). The maximum values of PC 2 are similar at both sites, but the minimum value is much lower at Lat-A5. The minimum value of Lat-A5 is approximately 120% lower than the minimum value at Lat-A2. Like PC 1, the range of values for PC 2 at Lat-A5 is greater, approximately 75% greater than at Lat-A2.

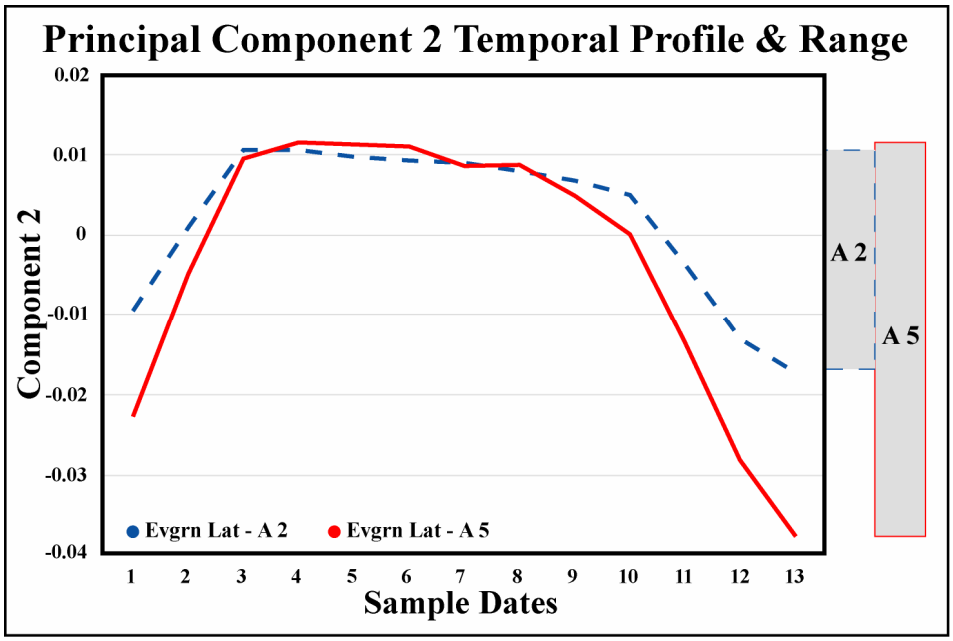

Figure 35. Vegetation density effects - Evergreen: PC 2 temporal profile for samples Lat-A2 and Lat-A5 over 13 orbits

There is a high inverse correlation between Component 2 and solar zenith angle at both samples with r^2 values of 0.96 at each sample (Figure 36 a / b). Similarly, there is high inverse correlation between Component 2 and the relative solar azimuth angle at both samples (Figure 37 a / b). Sample Lat-A2 has an r^2 of 0.94 and Lat-A5 is slightly higher with an r^2 value of 0.96.

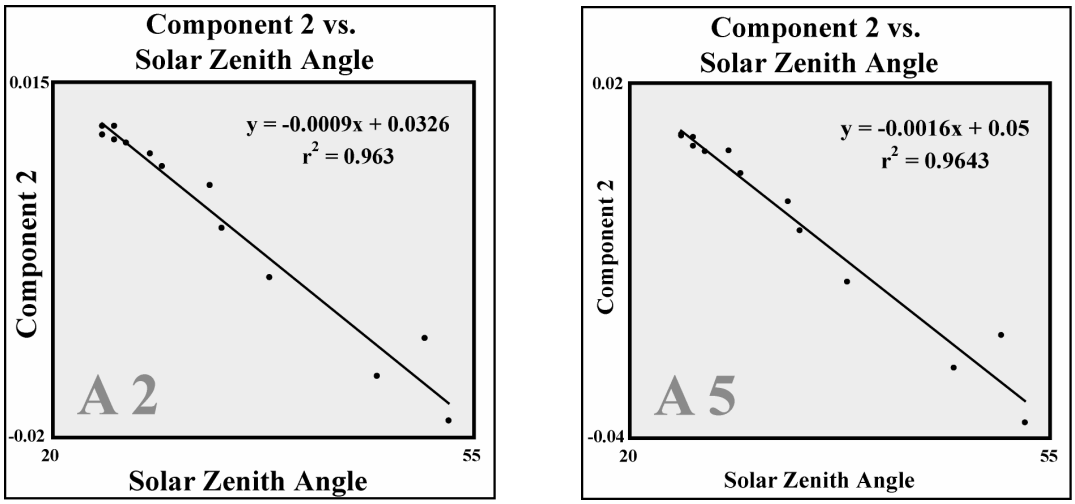

Figure 36 a / b. Vegetation density effects - Evergreen: .a The plot on the left shows the correlation of solar zenith angle vs. PC 2 for sample Lat-A2 .b The plot on the right shows the correlation of solar zenith angle vs. PC 2 for sample Lat-A5

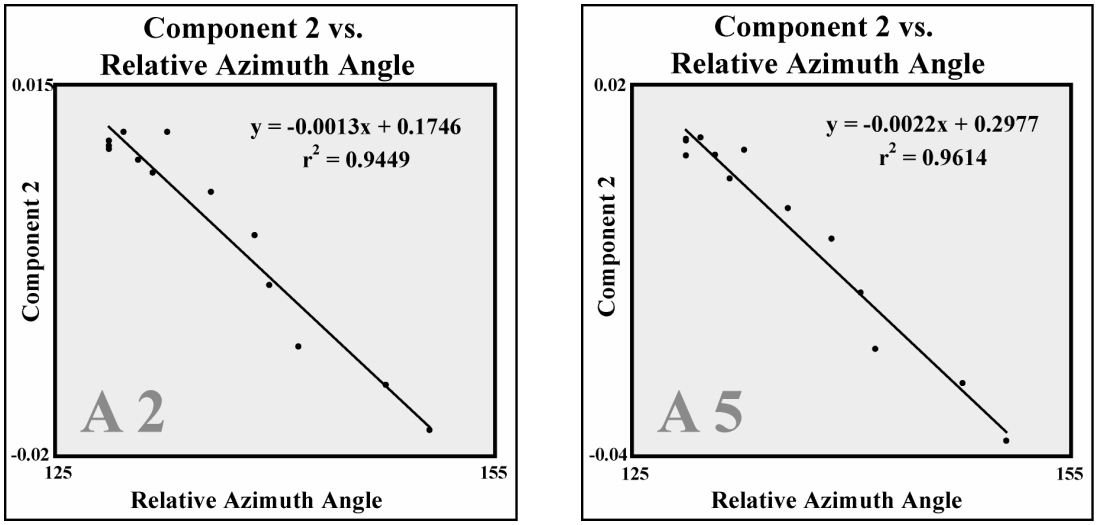

Figure 37 a / b. Vegetation density effects - Evergreen: .a The plot on the left shows the correlation of relative solar / sensor azimuth angle vs. PC 2 for sample Lat-A2 .b The plot on the right shows the correlation of relative solar / sensor azimuth angle vs. PC 2 for sample Lat-A5.

Shrubland and Grassland Site

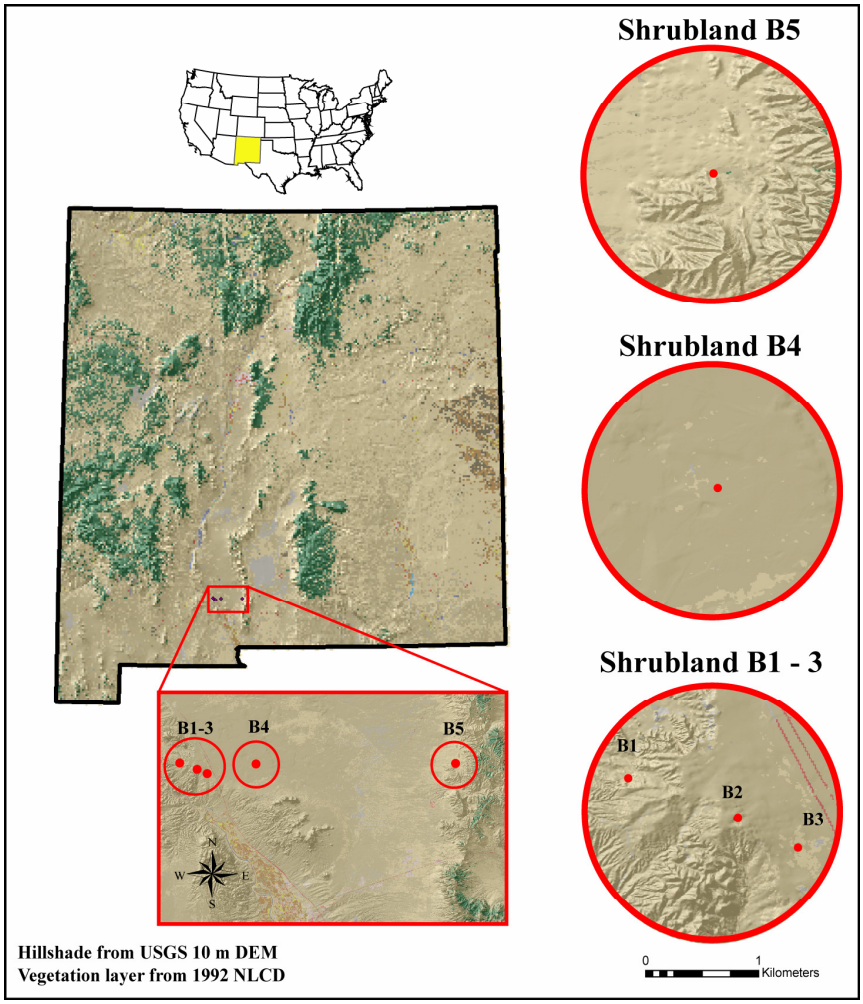

Figure 38. Vegetation density effects - Shrubland: Site overview map

Five samples from the shrublands and grasslands of southern New Mexico were selected to examine the effects of varying density and species of vegetation on the principal components (Figure 38, Table 10). Shrubland samples were selected to vary in percent of groundcover and vegetation type. Samples Lat-B1 and Lat-B5 are primarily grassland. Samples Lat-B3 and Lat-B4 are shrubland dominated. Sample Lat-B2 is transitional between grassland and shrubland. Each of the five samples consists of varying percentages of bare ground and non-tree vegetation (Table 11). Samples were selected to be at similar latitude and cover approximately 36 kilometers east-to-west.

Table 10. Vegetation density effects - Shrubland: Sample dates and orbits

Sample	Date	Orbit		Sample	Date	Orbit
1	1/15/2005	27019		8	4/21/2004	28417
2	1/29/2004	21893		9	5/20/2004	23524
3	2/2/2002	11408		10	6/21/2004	23990
4	2/24/2003	11641		11	8/8/2004	24689
5	3/1/2004	22359		12	10/30/2005	21213
6	3/17/2004	22592		13	12/1/2005	31679
7	4/5/2005	28184		14	12/14/2004	26553

Table 11. Vegetation density effects - Shrubland: MODIS VCF estimates of vegetation cover

Shrubland Sample	% Tree	% Non-tree	% Bare
B1	0	12	82
B2	0	22	76
B3	0	14	84
B4	0	16	82
B5	0	56	41

The mean reflectance profiles of the Shrubland density samples show the grassland samples with consistently lower mean reflectance than the shrub or transitional samples (Figure 39). The mean reflectance profile for sample Lat-B4 is unique from the other samples, showing a much higher sensitivity to the temporal variation in reflectance than the other samples. Sample Lat-B4 has the highest mean reflectance over time, and samples Lat-B1 and Lat-B5, both grassland, the lowest.

With the exception of sample Lat-B4, the temporal variation in reflectance is similar for the grass samples (Lat-B1 and Lat-B5) and the shrub and transitional samples (Lat-B2 and Lat-B3), which are each separated by their magnitude of reflectance. Examined by magnitude and range of reflectance and excluding Lat-B4, the magnitude of reflectance is comparatively higher for the Shrubland and

transitional samples than at the grassland samples, while the variation in reflectance between the five samples all fall within the same overall range of value.

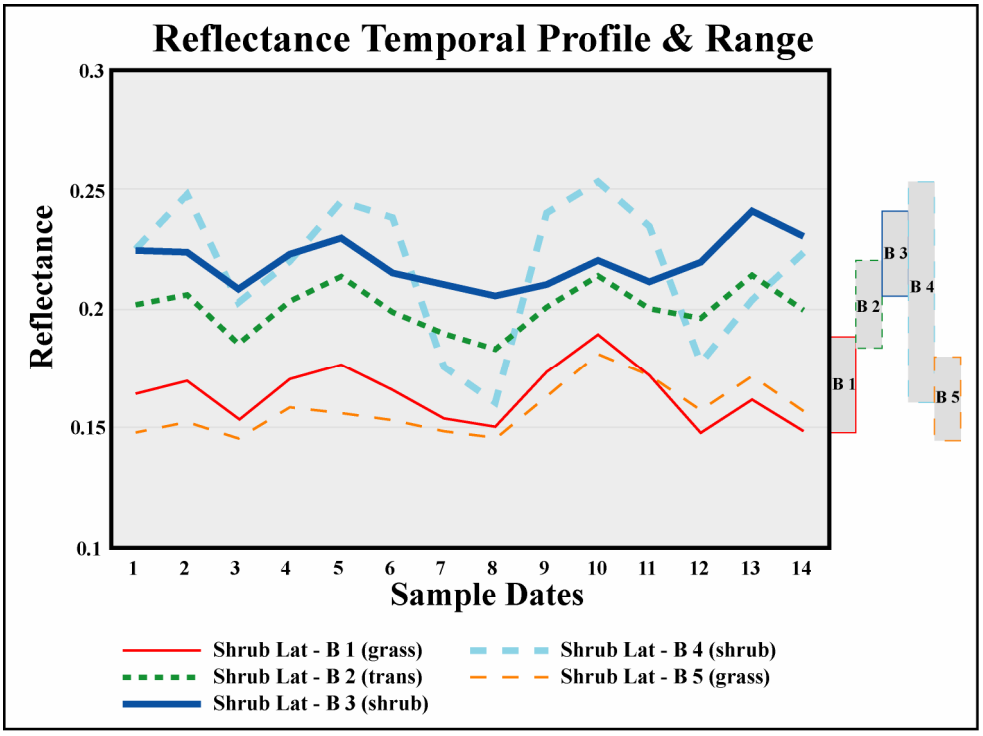

Figure 39. Vegetation density effects - Shrubland / Grassland: Aggregate reflectance temporal profile for samples Lat-B1 – Lat-B5 over 14 orbits

Principal component 1, like reflectance, shows clear distinction between the shrubland and grassland samples (Figure 40). As was the case for the mean reflectance, the PC 1 profile of sample Lat-B4 is unique among the five samples. The PC 1 range of sample Lat-B4 is approximately 140% greater than the range of the sample Lat-B3, the next greatest range. With the exception of sample Lat-B4, the range of values for PC 1 are nearly similar at all samples, and the PC 1 profiles show the Shrubland samples to have higher PC 1 value than the grassland samples.

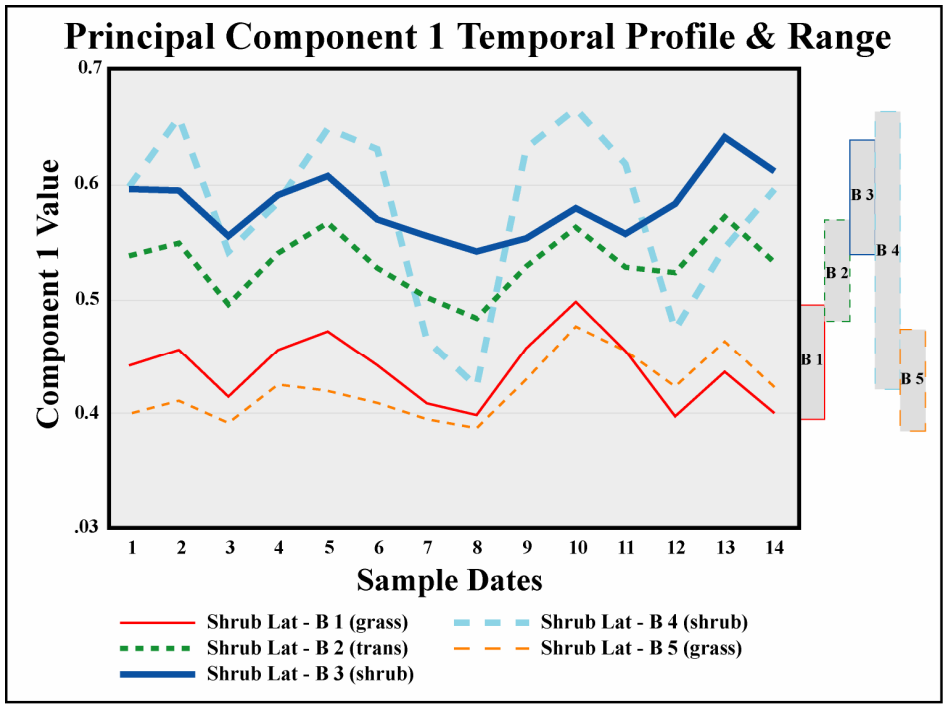

Figure 40. Vegetation density effects - Shrubland / Grassland: Principal component 1 temporal profile for samples Lat-B1 – Lat-B5 over 14 orbits.

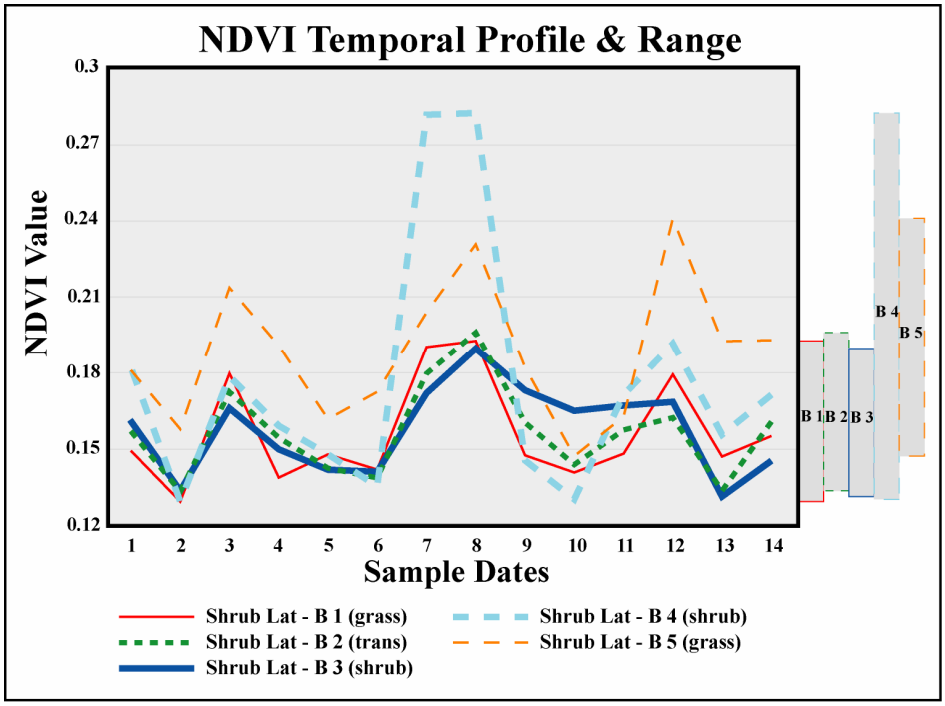

Figure 41. Vegetation density effects - Shrubland / Grassland: NDVI temporal profile for samples Lat-B1 – Lat-B5 over 14 orbits.

The NDVI temporal profiles show similar trends but with extreme differences in magnitude between samples and differences in the range of values (Figure 41). Like the ranges for PC 1, sample Lat-B4 has the highest range in NDVI, 120% higher than the average of the other 4 samples.

The correlation between PC 1 and NDVI varies by sample (Figure 42 a / b, Figure 43 a / b, Figure 44). Each sample shows an inverse correlation between PC 1 and NDVI similar to the Shrubland correlation site evaluations. The lowest correlation is at sample Lat-B5 (grassland) with an r^2 value of 0.48. The highest correlations are at samples Lat-B2 and Lat-B4 (transitional and shrubland) with r^2 values of 0.79 and 0.78. Samples Lat-B1 and Lat-B3 (grassland and shrubland) have similar moderate correlations with r^2 values of 0.67 and 0.65.

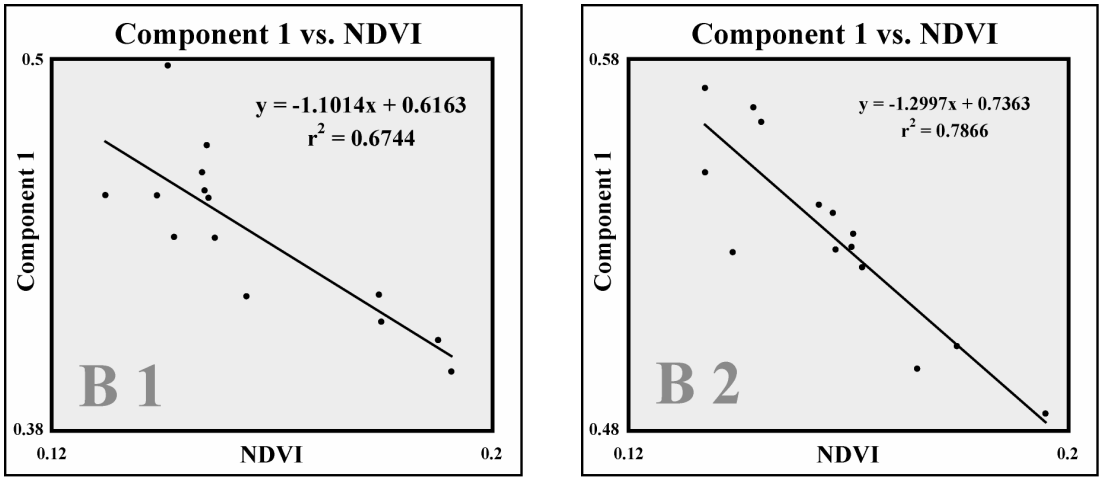

Figure 42 a / b. Vegetation density effects - Shrubland: .a The plot on the left shows the correlation plot of NDVI vs. PC 1 for sample Lat-B1 .b The plot on the right shows the correlation plot of NDVI vs. PC 1 for sample Lat-B2

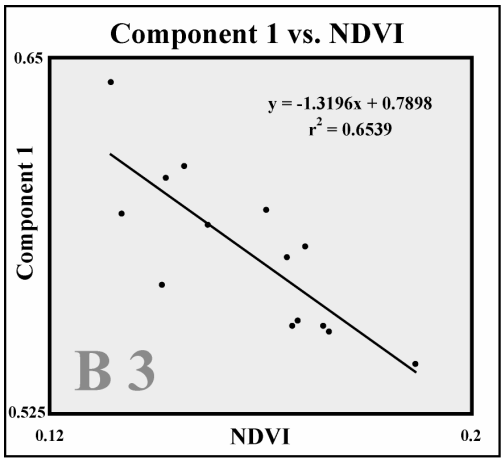

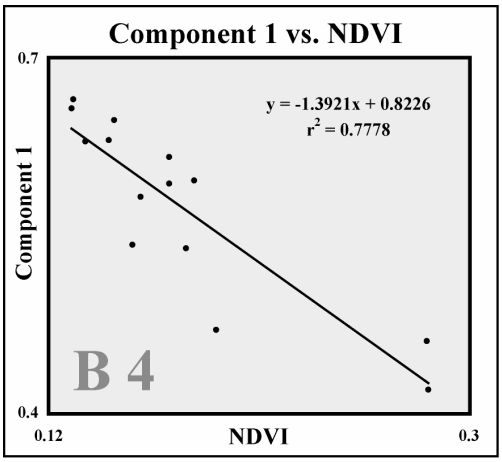

Figure 43 a / b. Vegetation density effects - Shrubland: .a The plot on the left shows the correlation plot of NDVI vs. PC 1 for sample Lat-B3 .b The plot on the right shows the correlation plot of NDVI vs. PC 1 for sample Lat-B4

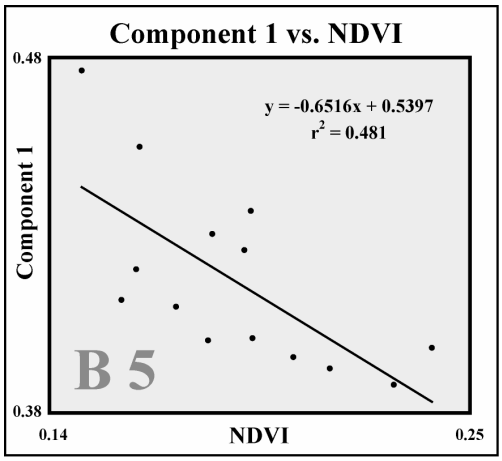

Figure 44. Vegetation density effects - Shrubland: Correlation plot of NDVI vs. PC 1 for sample Lat-B5

Examination of the range and magnitude of PC 2 at each of the five samples shows that all samples have similar maximum PC 2 values, and similar profiles over time (Figure 45). It was interesting to note that sample Lat-B4, which had a reflectance profile and PC 1 profile extremely dissimilar from the other samples, displayed a PC 2 profile completely in line with the other samples. The grassland samples (Lat-B1 and Lat-B5) had the largest range of PC 2 value, and the shrubland and transitional samples the lowest. Sample Lat-B3 had the absolute lowest range of Component 2 value.

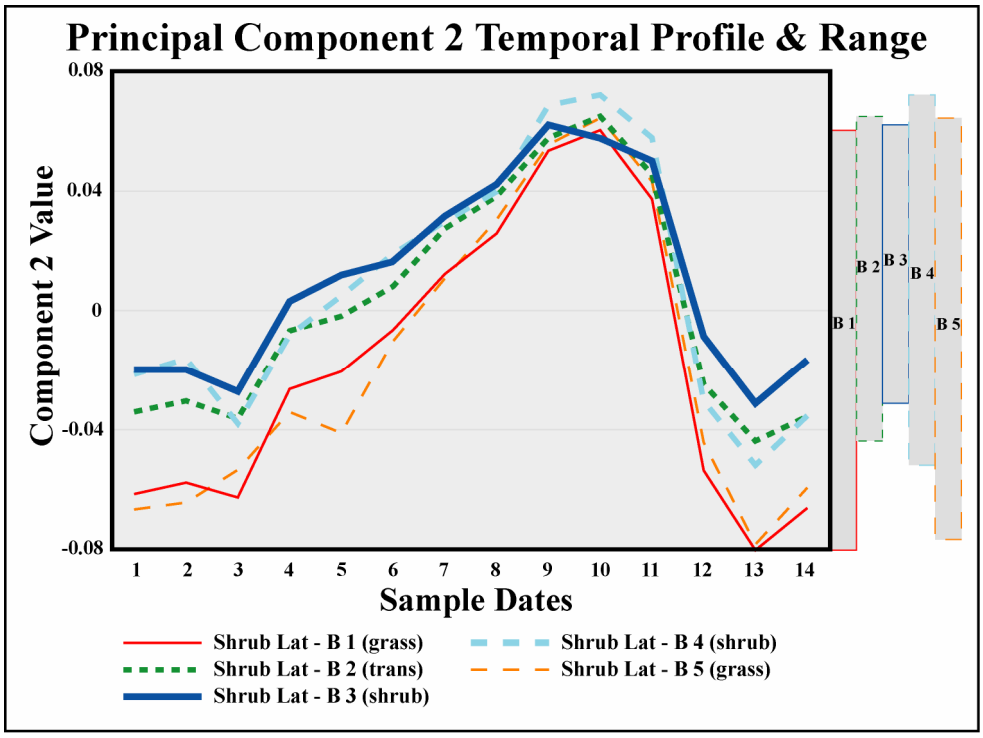

Figure 45. Vegetation density effects - Shrubland / Grassland: PC 2 component 2 temporal profiles for samples Lat-B1 – Lat-B5 over 14 orbits

For each of the five samples, there is very high inverse correlation between PC 2 and the solar zenith angle (Figure 46 a / b, Figure 47 a / b, Figure 48). The lowest r^2 is at sample Lat-B4, 0.94, with sample 3 at 0.97 and samples Lat-B1, Lat-B2, and Lat-B5 at 0.98. Similarly, there is high inverse correlation between Component 2 and the relative azimuth angle between sun and sensor for each of the samples, with an r^2 value of 0.92 for every sample (Figure 49 a / b, Figure 50 a / b, Figure 51).

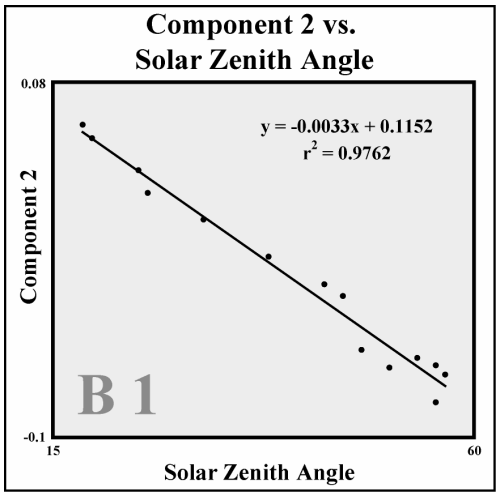

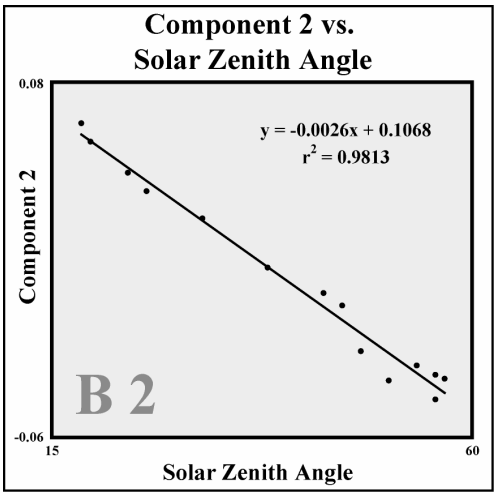

Figure 46 a / b. Vegetation density effects - Shrubland: .a The plot on the left shows the correlation of solar zenith angle vs. PC 2 for sample Lat-B1 .b The plot on the right shows the correlation of solar zenith angle vs. PC 2 for sample Lat-B2

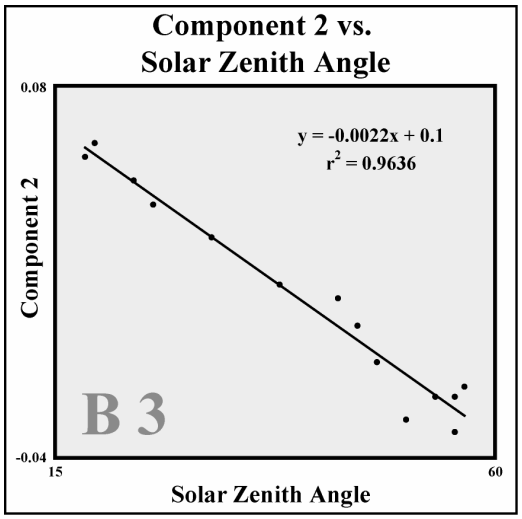

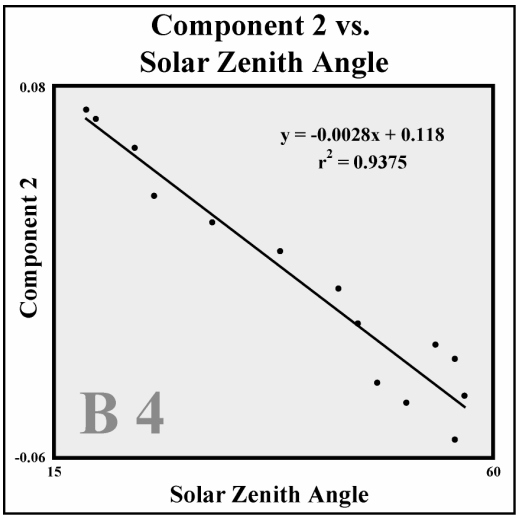

Figure 47 a / b. Vegetation density effects - Shrubland: .a The plot on the left shows the correlation of solar zenith angle vs. PC 2 for sample Lat-B3 .b The plot on the right shows the correlation of solar zenith angle vs. PC 2 for sample Lat-B4

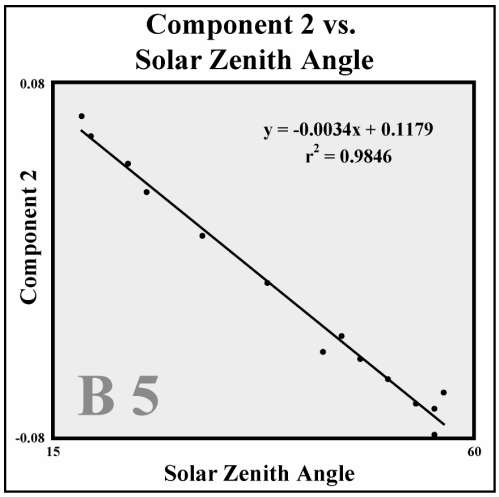

Figure 48. Vegetation density effects - Shrubland: Correlation plot of solar zenith angle vs. principal component 2: Sample Lat-B5

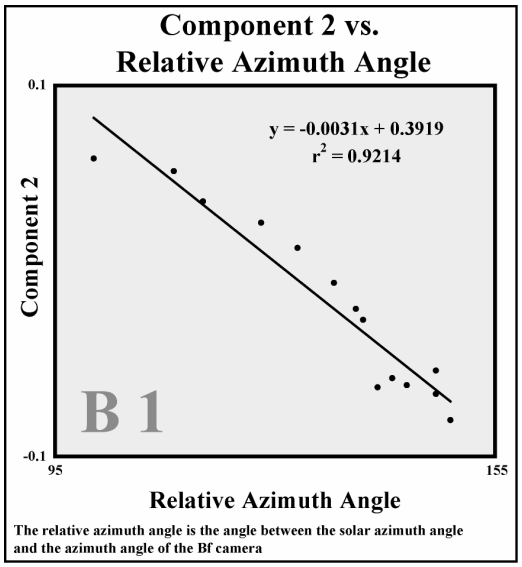

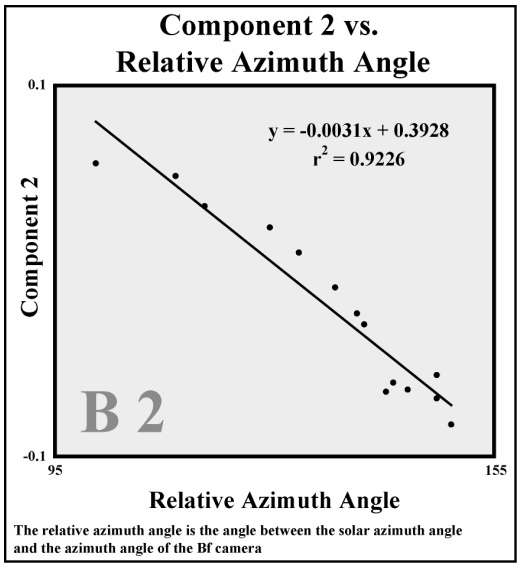

Figure 49 a / b. Vegetation density effects - Shrubland: .a The plot on the left shows the correlation of relative solar / sensor azimuth angle vs. PC 2 for sample Lat-B1 .b The plot on the right shows the correlation of relative solar / sensor azimuth angle vs. PC 2 for sample Lat-B2

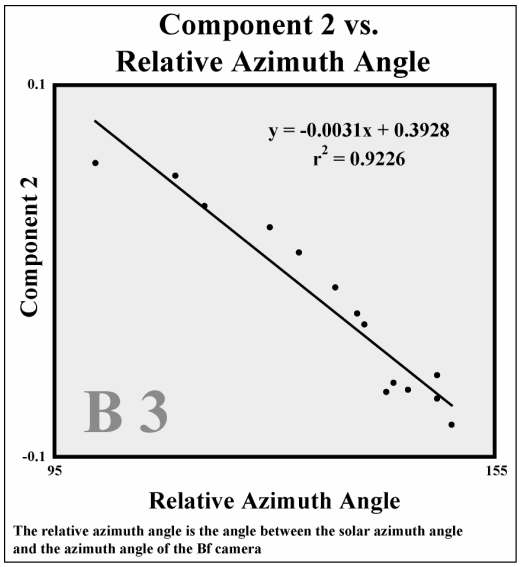

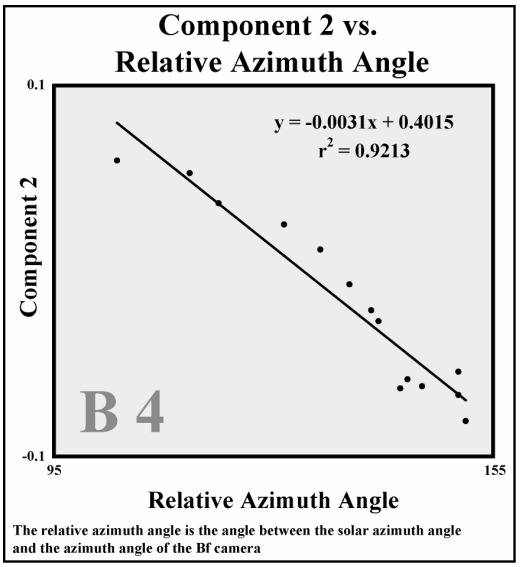

Figure 50 a / b. Vegetation density effects - Shrubland: .a The plot on the left shows the correlation of relative solar / sensor azimuth angle vs. PC 2 for sample Lat-B3 .b The plot on the right shows the correlation of relative solar / sensor azimuth angle vs. PC 2 for sample Lat-B4

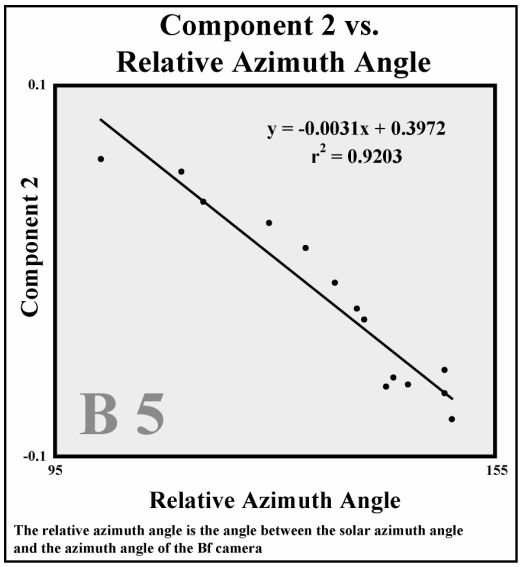

Figure 51. Vegetation density effects - Shrubland: Correlation plots of relative solar / sensor azimuth angle vs. principal component 2: Sample Lat-B5

Comparison of Evergreen and Shrubland Sites

Examination of samples Lat-A2 and Lat-A5 from the Evergreen latitude profile site shows that each of the samples has a PC 1 profile very similar to its mean reflectance profile. Between samples the primary difference is in the magnitude of mean reflectance, and consequently PC 1, which is higher at Lat-A5 due to a higher percentage of bare ground and less tree cover. The PC 2 temporal profile shows a relationship between the two samples that is temporally dependent. The samples have nearly similar maximum values for eight sampled dates near the summer solstice. As the sampled dates moved away from the summer solstice, the PC 2 trends of each sample diverge. Lat-A5 drops in PC 2 value significantly lower that Lat-A2. The temporal range of PC 2 for Lat-A5 is 75% greater than for Lat-A2.

The Shrubland latitude profile samples were selected to examine the relationship of the principal components among samples that had no tree cover and varying percentages of non-tree vegetation and bare ground. The five Shrubland latitude profile sites show mean reflectance temporal profiles varying between samples, but with the two grassland samples, Lat-B1 and Lat-B5, displaying the same temporal variations as the other samples, only at a lower magnitude. The profiles in PC 1 are similar to those of mean reflectance. The temporal profile of PC 2, like for the Evergreen samples, shows each sample with similar maximum PC 2 value at the dates sampled closest to the summer solstice, with diverging profiles away from the summer solstice. The range of PC 2 at each of the sites show Lat-B1 and Lat-B5 as having the lowest PC 2 values and the greatest PC 2 range. The VCF classifies these two samples differently in terms of percent ground cover, but the 1992 NLCD classifies both samples as grassland. Visual inspection with Landsat ETM + imagery indicates that these two samples have very high percentage of ground cover.

Changes in the Structural Dynamics of Vegetation after a Burn

Evaluation of the ability of the principal components to relate the structural changes in vegetation following a stand-replacing disturbance was conducted on the Biscuit Fire Complex in southwestern Oregon. The Biscuit Fire started on July 13,

2002, burning approximately 500,000 acres of the Siskiyou National Forest, including the whole of the Kalmiopsis Wilderness Area (Wilderness 2006). Investigation of vegetation change expressed through the PCA transformation was evaluated for seven samples from the Biscuit Fire Complex, for a cross section of the burned area, and for the entire burned area. Burn severity was assessed from a vegetation change layer created by the Siskiyou National Forest (USDA-FS 2006).

Samples were taken from MISR orbit 8540 (July 26th, 2001) and orbit 19025 (July 26th, 2003) to assess the change in vegetation. Areas of douglas fir / mixed conifer (OR-GEO 2006), existing on slopes of less than 5º, were filtered for sampling. From these potential sites, three samples identified as: 'little or no change' and four from: 'dead trees without needles' were selected for examination (Figure 52). These areas represent regions where the fire caused little to no change (LNC), and areas of high severity burn (HSB). Vegetation change layers were created for the whole of the Biscuit Fire Complex for the first three principal components to assess the ability of the PCA transformation to relate the change in the structural dynamics of vegetation after a major disturbance at the landscape level. A vegetation change layer of NDVI, derived from the MISR nadir camera, was created as a reference to compare the principal component values.

The topography of the Siskiyou National Forest is very rugged with elevations ranging from 500 to 5,000 feet. Vegetation classes varied from location to location, as did burn severity. Selection of the study sites was greatly constrained by the need to find areas of both high severity burn and little to no change in conjunction with similar vegetation cover, and low slope. Due to these constraints there exists the possibility of spatial autocorrelation between samples.

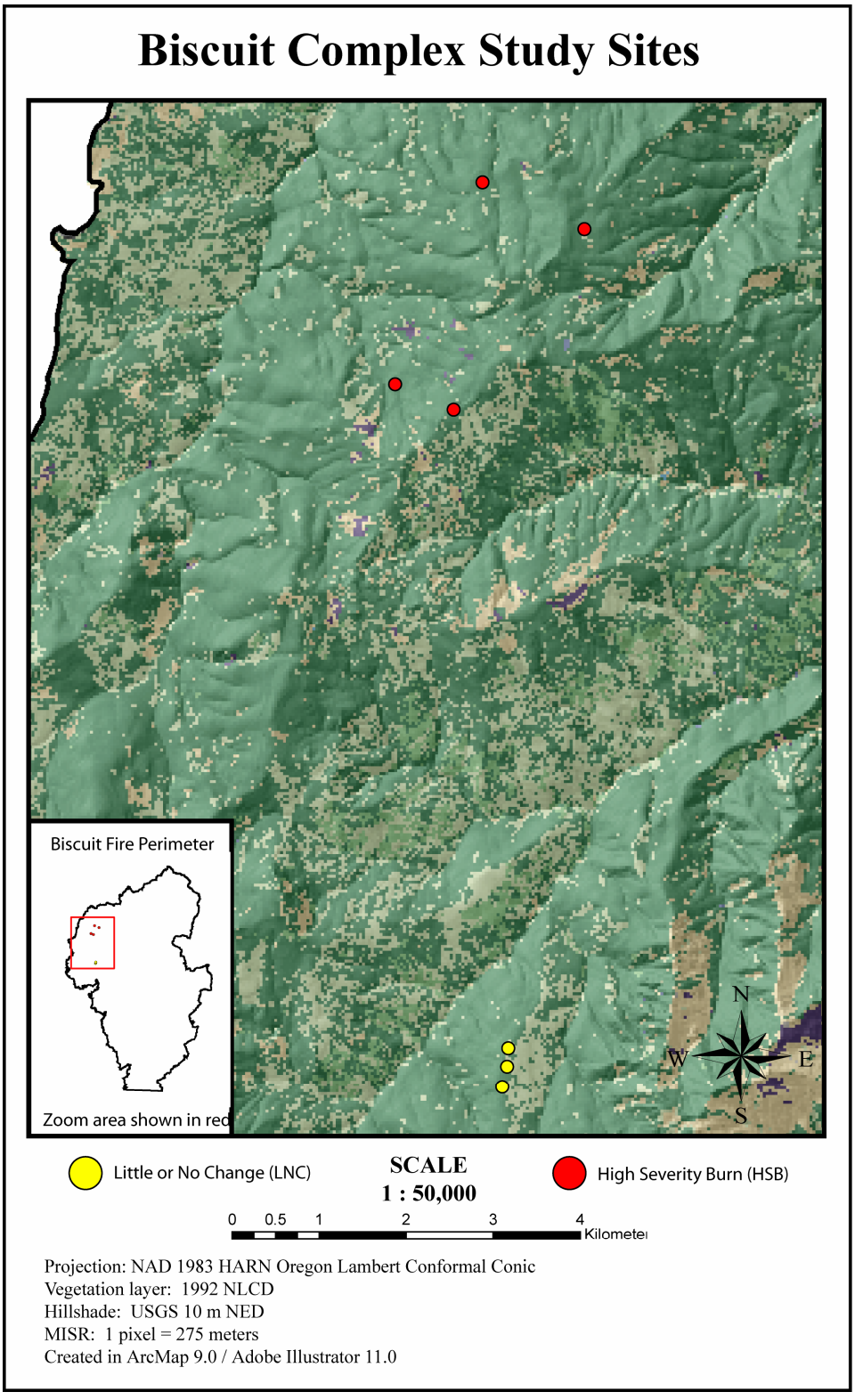

Figure 52. Biscuit Fire: Study sites

Study Samples: Change from 2001 - 2003

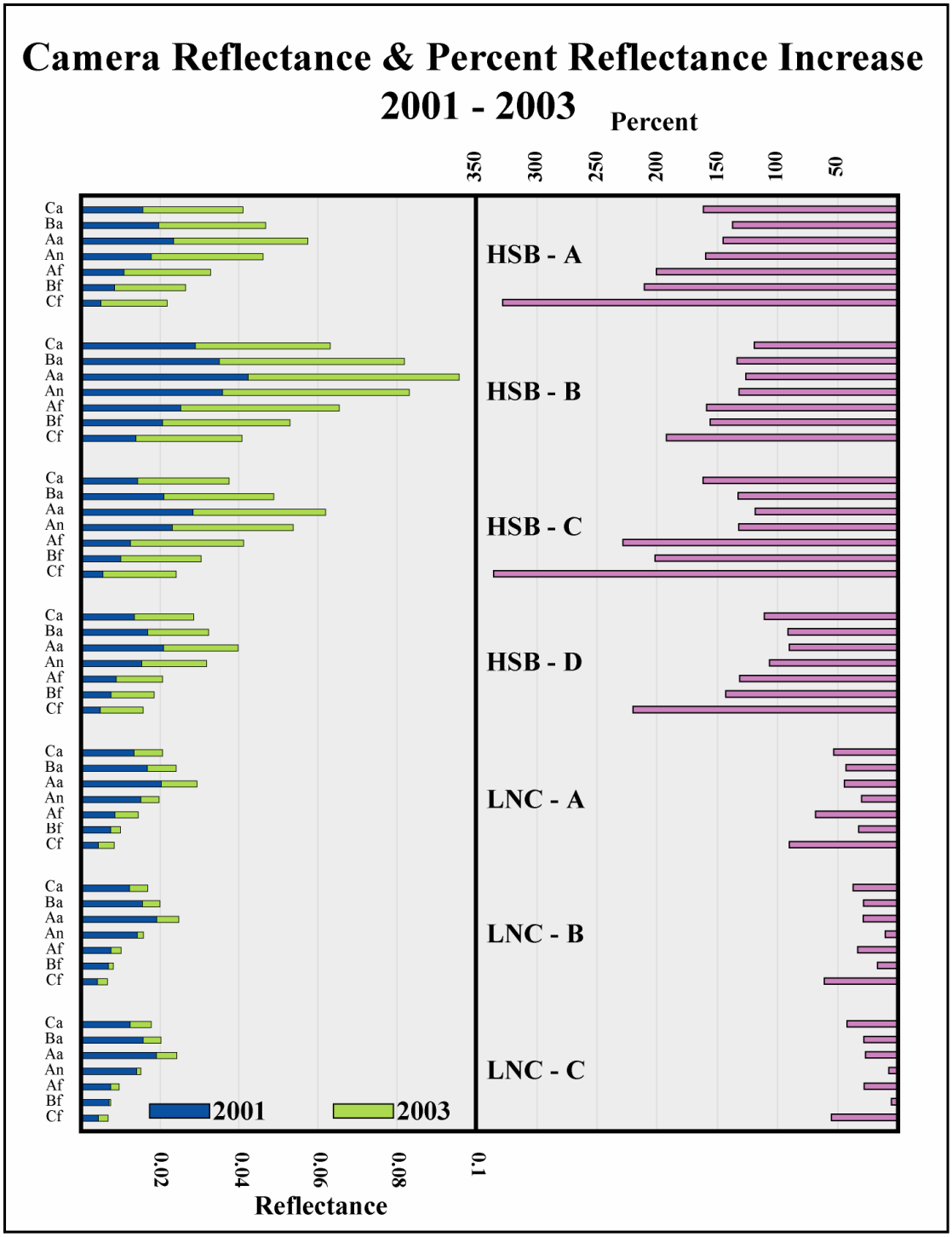

Figure 53. Biscuit Fire: Camera reflectance and percent reflectance increase 2001 - 2003

At the seven samples selected from the Biscuit Complex, reflectance increased for every sample from both the HSB samples and the LNC samples, with a much greater increase at the HSB areas than the LNC areas (Figure 53). The increase in mean reflectance at the HSB samples ranged from 106 – 161%, averaging 138% across the four samples. Reflectance increased less at the LNC samples, with values ranging from 24 – 45%, averaging 32% increase across samples. For each sample, the greatest increase in reflectance was for the Cf camera. For the HSB areas: the second and third highest reflectance increases were for the Af and Bf cameras, while at the LNC samples the cameras with the second and third highest increase in reflectance varied by sample.

NDVI decreased across all samples with the HSB samples decreasing much more than the LNC samples (Figure 54). On average, the NDVI of the HSB samples decreased 10 times more than the LNC samples.

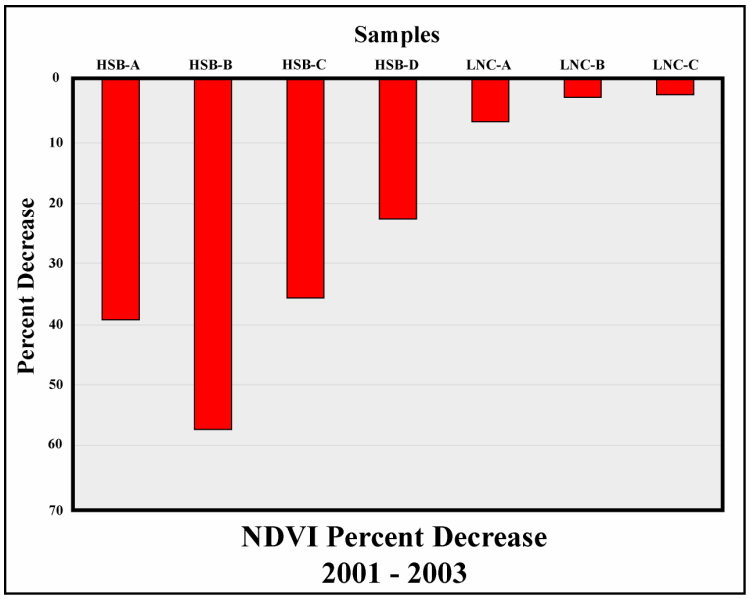

Figure 54. Biscuit Fire: NDVI percent decrease 2001 – 2003

Principal component 1 increased across all samples, with the HSB samples increasing an average of 143%, and the LNC samples an average of 34% (Figure 55). The percent increase in PC 1 was very nearly similar the percent increase in mean reflectance for each sample.

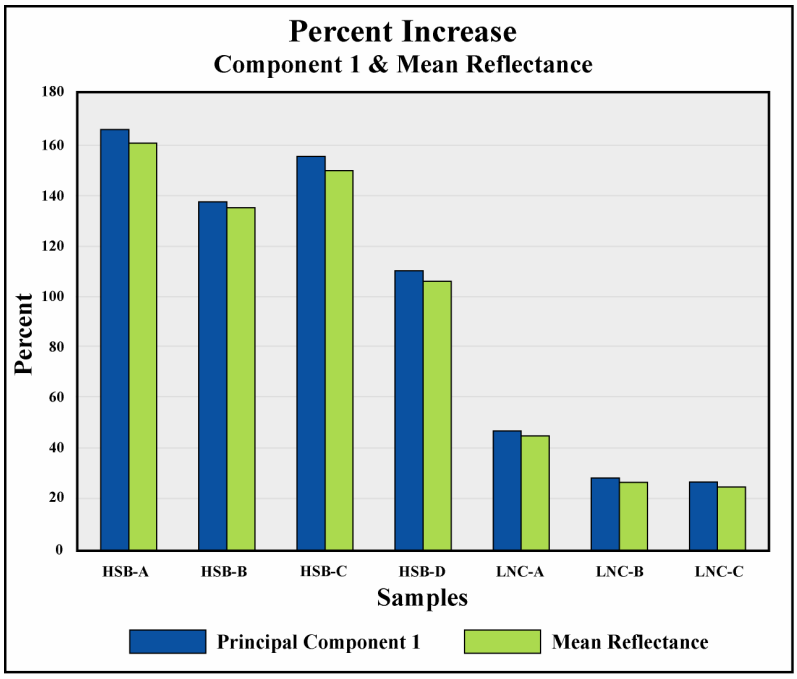

Figure 55. Biscuit Fire: Percent change of PC 1 and mean reflectance 2001 – 2003

Principal component 2 increased at the HSB samples and decreased at the LNC samples (Figure 56). The increase in PC 2 at the HSB areas was not consistent across samples. HSB - A and D increased 32% and 16%, respectively, while HSB – B increased 1,767% and HSB – C increased 3,534%. The LNC samples showed the greatest decrease at LNC-C, followed by B and A. All LNC samples decreased between 60% and 110% from 2001 – 2003.

The 1,767% and 3,534% increase in PC 2 at two of the HSB samples is the result of very small numbers increasing. For instance, HSB – B increased from negative four ten-thousandths to positive seven thousandths. While this change is still quite large relatively, the magnitude of increase compared to the breadth of PC 2 values in the vegetated sites from the correlation study sites is really not all that extraordinary.

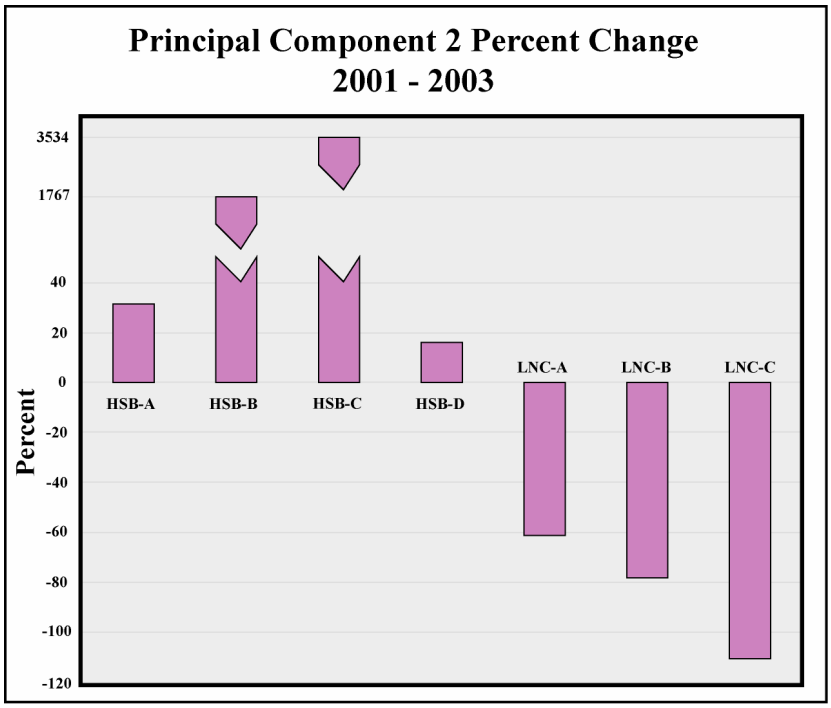

Figure 56. Biscuit Fire: Percent change of PC 2 2001 – 2003

Principal component 3 increased at all samples (Figure 57). The increase in PC 3 was higher for the HSB areas, with HSB-B having the highest percent increase of all samples. Examined against the percent decrease in NDVI (Figure 54), the HSB and LNC sample's increase in PC 3 relative to the other sample's increase is very similar to the decrease in NDVI among the samples relative to each other.

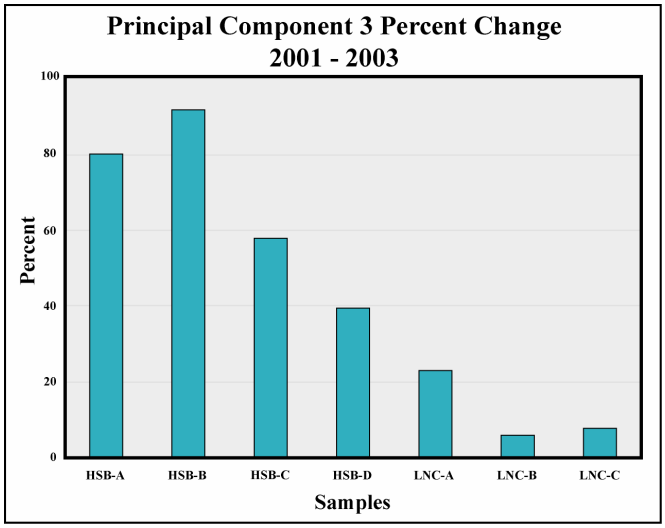

Figure 57. Biscuit Fire: Percent change of PC 3 2001 – 2003

Motion of Study Samples in PCA Space

Examination of Figure 58 shows the motion in PCA space of a cross section of pixels from the Biscuit Fire Complex after the burn. The area sampled is representative of all levels of burn severity and little to no change. The trend of the change from 2001 -2003 is of increasing PC 1 and PC 2 for the year immediately following the burn. This sample does not show the trajectory through PCA space of individual samples, only the general trend of samples after the fire, and does not discriminate between levels of burn severity.

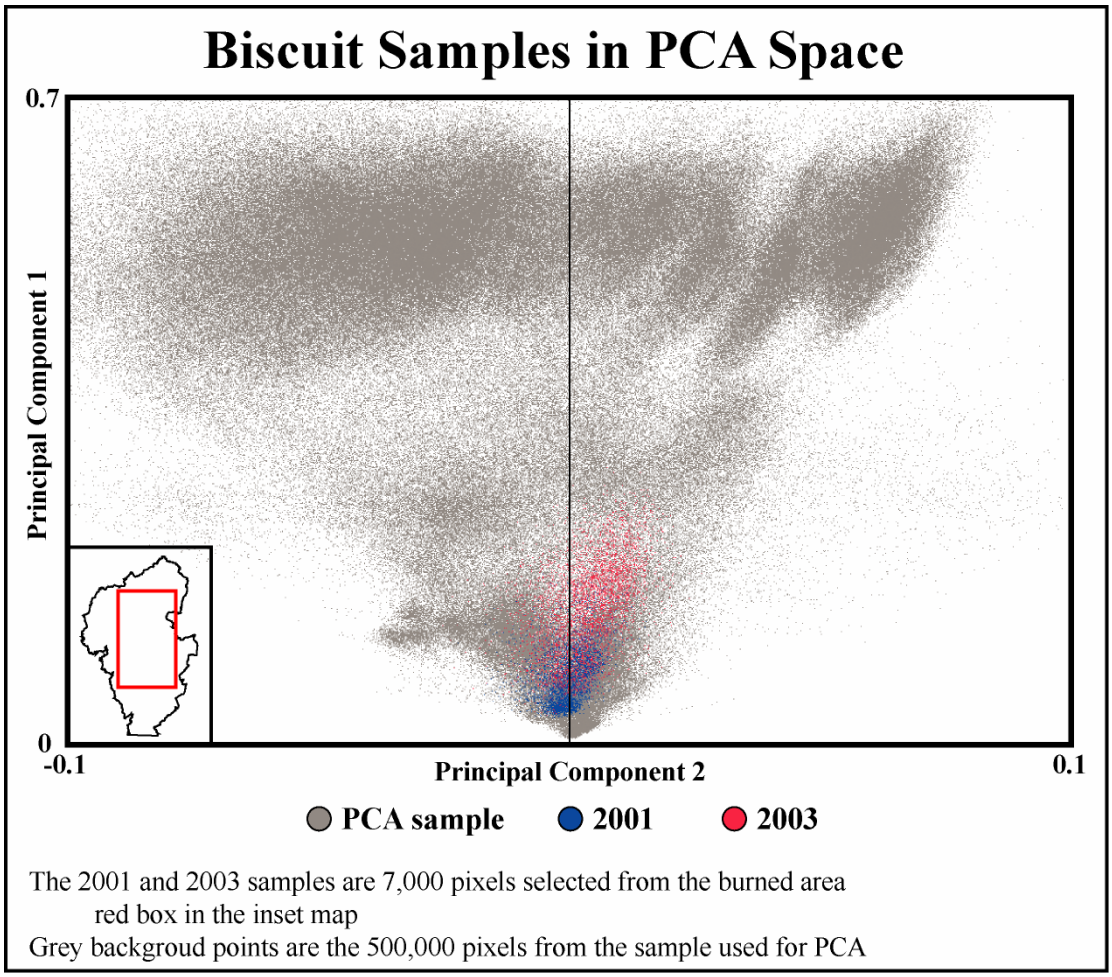

Figure 58. Biscuit Fire: Cross section of 7,000 pixels showing the change in PCA space of burned and unburned areas from 2001 and 2003. The scatter plot defining the shape of the M-Cone are the sites from the PCA sample

In the PC 1 vs. PC 2 dimension, all seven samples from the Biscuit Complex occupy a region in PCA space near the region defined by the Deciduous and Evergreen correlation study sites (Figure 59). Each of the HSB samples is unique in its position in the PCA space relative to the other HSB samples, with varying intensities along PC 1 and PC 2. This region of space can best be described as being of lower intensity along the PC 1 axis than the Evergreen and the Deciduous sites in the open canopy months, and of lower PC 2 intensity than the Deciduous sites in the closed canopy months.

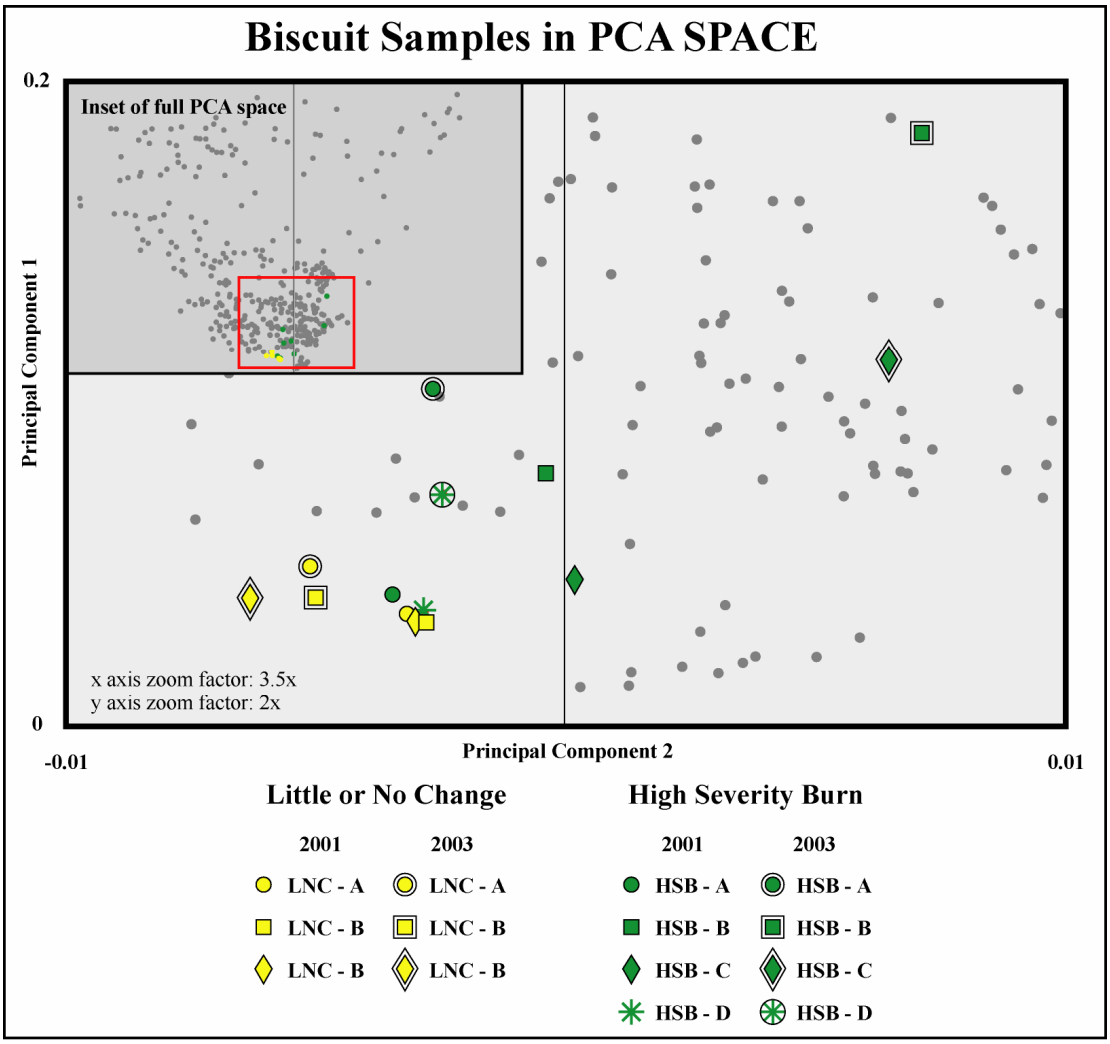

Figure 59. Biscuit Fire: Change in PC 1 vs. PC 2 space of HSB and LNC samples 2001 – 2003. The backdrop of points are the samples from the correlation study sites

All of the 2001 HSB samples have negative Component 2 values except for HSB – C. In contrast to the range the HSB samples from 2001 show in PCA space, the LNC samples from 2001 all occupy essentially the same space. There is almost no variation through PCA space among the LNC samples relative to the amount of space covered by the HSB samples. The PCA space occupied by the LNC samples exists lower along the PC 1 axis than any of the HSB samples, and along the PC 2 axis with the lowest of the HSB samples (A and D).

Samples HSB – A and D both show an increase along the PC 1 axis, with comparatively little change along the PC 2 axis. HSB – B and C both increased along the PC 1 axis and also increased along the PC 2, axis moving well into the positive PC 2 region of space. The HSB samples in 2003, like their counterparts in 2001, are still within the same general region of PCA space as defined by the Evergreen sites. The LNC samples behaved very differently than the HSB samples after the burn, decreasing in PC 2 value and showing very little increase along the PC 1 axis.

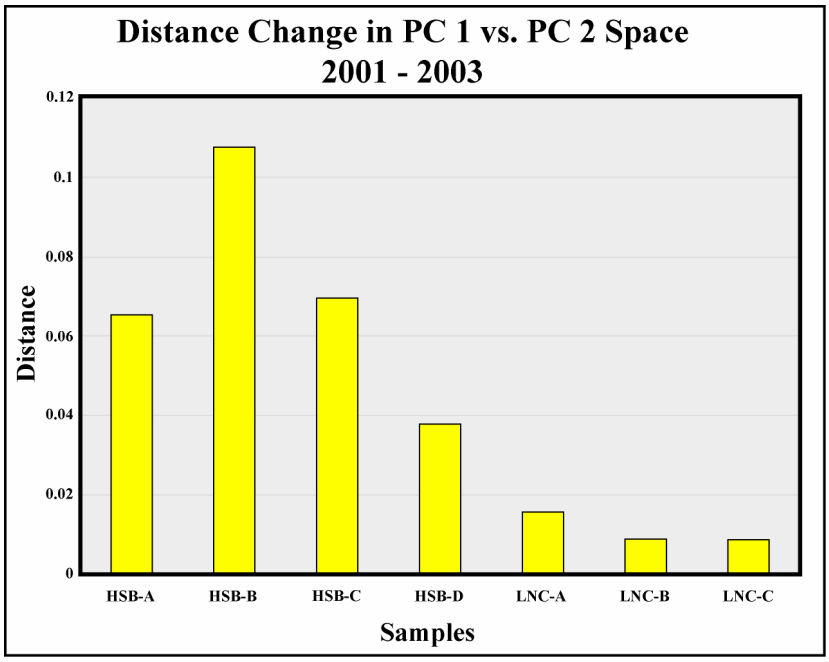

Figure 60. Biscuit Fire: Distance change in PC 1 vs. PC 2 space 2001 - 2003

The change in location in PCA space and the vector change (Figure 60) from 2001 to 2003 are much more pronounced in the HSB samples than in the LNC samples. On average, the HSB samples had a vector change 525% higher than the LNC samples. The HSB samples showed the greatest vector change after the fire, with HSB – B having the greatest vector change, HSB – A and C about the same amount, and HSB – D the lowest.

In the PC 1 vs. PC 3 dimension, all seven samples occupy a region in PCA space along the leading edge of the M-Cone, in the negative half of the space (Figure 61). The seven samples had lower PC 1 value than most of the correlation study site samples, and PC 3 values similar to those of the correlation study site Evergreen samples. The HSB samples in 2001 varied through the PCA along both axes. The samples are spread along the leading edge of the M-Cone in this dimension with much more variation in space for the HSB samples than for the LNC samples. The samples of LNC are tightly grouped in this dimension, similar to their grouping in the PC 1 vs. PC 2 dimension, with values lower along the PC 1 axis, and higher along the PC 3 axis than the HSB samples. For both the HSB and LNC samples from 2001, there is an increase in PC 1 value with decreasing PC 3 value.

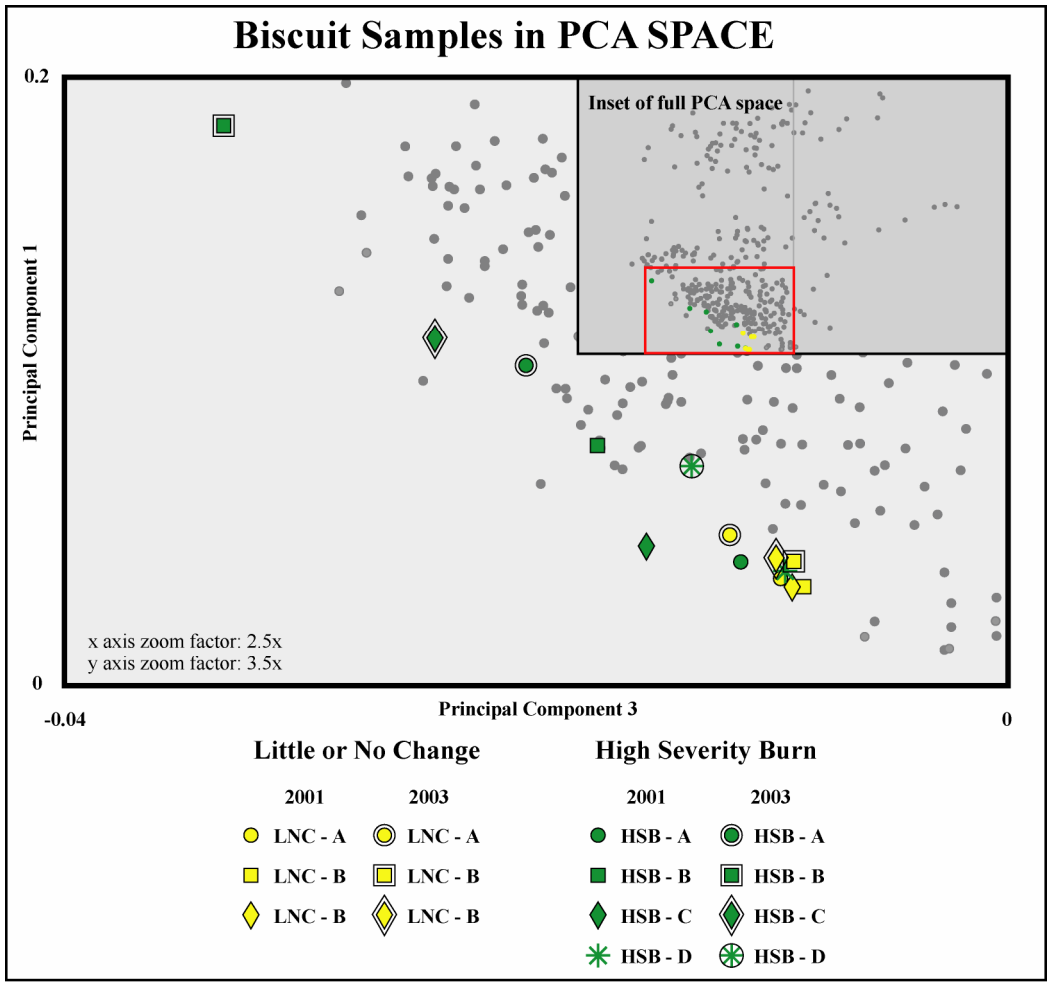

Figure 61. Biscuit Fire: Change in PC 1 vs. PC 3 space of HSB and LNC samples 2001 – 2003. The backdrop of points are the samples from the correlation study sites

In the PCA space, the motion of samples from 2001 to 2003 show an increase along the PC 1 axis and a decrease along the PC 3 axis. Samples are moving along the leading edge of the M-Cone space. This is reflected in both the HSB samples and the LNC samples. The primary difference between the variations of the two groups in PCA space from 2001 - 2003 is the magnitude of change. The HSB samples traveled greater distance through the PCA space than the LNC samples, but the general direction of travel was similar for both groups.

The average vector change of the HSB samples was approximately 260% greater than the average vector change of the LNC samples (Figure 62). The HSB samples 1, 2, and 3 all had change in space significantly greater than the LNC samples, with HSB-2 showing the greatest increase overall. HSB sample 4 showed vector change nearly similar to the LNC samples.

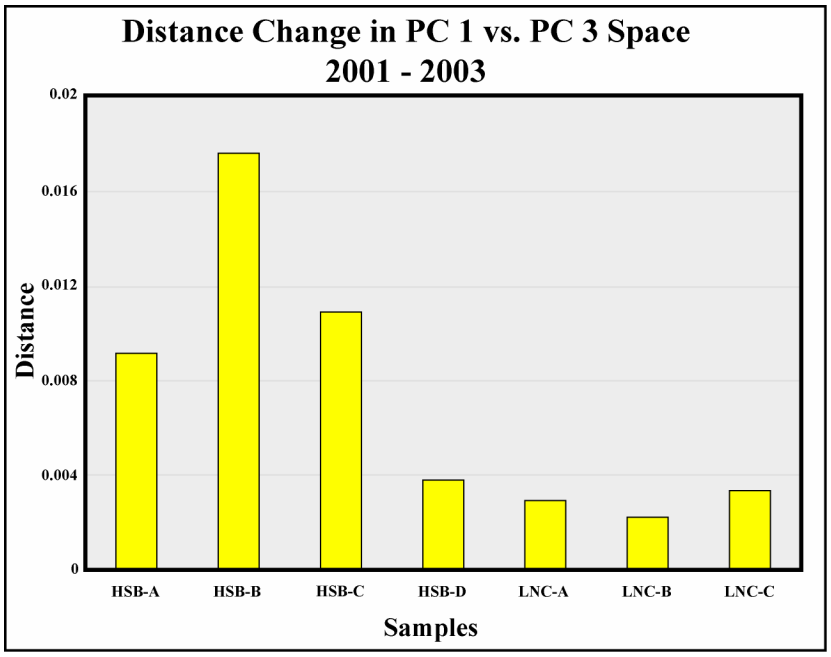

Figure 62. Biscuit Fire: Distance change in PC 1 vs. PC 3 space 2001 - 2003

In the PC 2 vs. PC 3 dimension, all seven samples from the Biscuit Complex occupied a region of space shared by nearly every one of the correlation study samples (Figure 63). The Deciduous, Evergreen – C, Grassland, Shrubland, and Agriculture sites all have samples in the region of the PCA space occupied by the Biscuit samples. The region of the PCA space occupied by the Biscuit Complex samples cannot accurately be described except as being roughly in the center of the possible spread of points as defined by the correlation study sites.

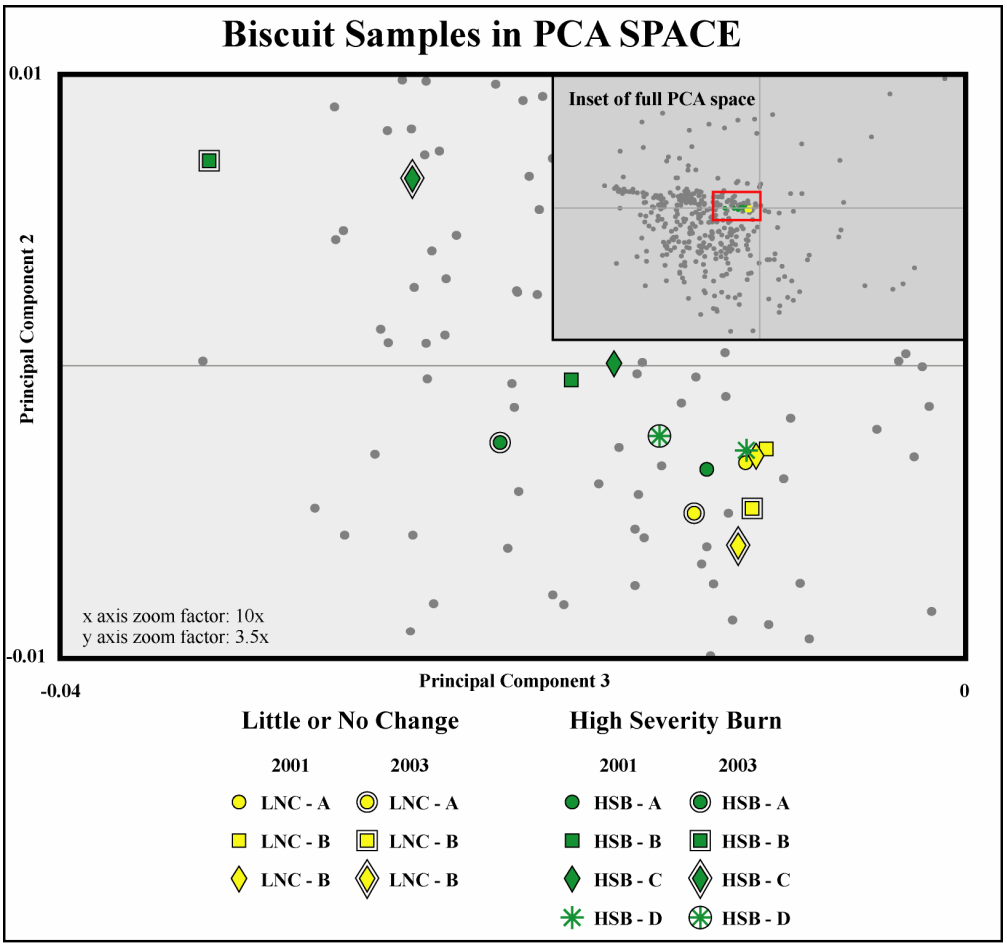

Figure 63. Biscuit Fire: Change in PC 2 vs. PC 3 space of HSB and LNC samples 2001 – 2003. The backdrop of points are the samples from the correlation study sites

The HSB samples in 2001 exhibit a greater spread through the PC 2 vs. PC 3 space than did the LNC samples. This is similar to the behavior of both groups in the other two dimensions. There is very little variation along the PC 2 axis between samples as compared to the amount of variation along the PC 3 axis. The LNC samples clustered together higher along PC 3 axis than the HSB samples, with similar intensity along the PC 2 axis.

As was the case in the other dimensions, the motion of HSB burn sites in the PC 2 vs. PC 3 dimension was much more pronounced than the motion of the LNC samples. The average vector change in the HSB samples was approximately 710% higher than the average change of the LNC samples. HSB-2 had the greatest vector change, 68% greater than the average change of the other HSB samples. This is similar to what occurred in the other two dimensions. The motion in PC 1 vs. PC 3 space for the HSB samples is quite different from the LNC samples. HSB samples A and D move negatively down the PC 3 axis with very little change along the PC 2 axis. HSB samples B and C each move negatively down the PC 3 axis, but also significantly increase along the PC 2 axis.

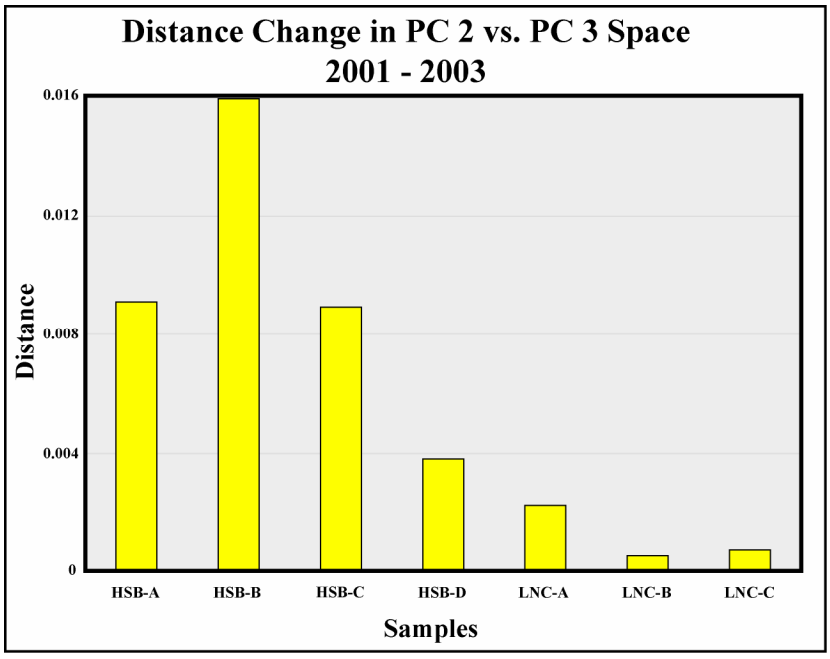

Figure 64. Biscuit Fire: Distance change in PC 2 vs. PC 3 space 2001 - 2003

In contrast to the other dimensions where the vector change for the LNC samples from 2001 – 2003 was similar for each sample, in the PC 2 vs. PC 3 dimension, the vector change for LNC-A was much greater than the change for the other LNC samples (Figure 64). LNC-A had a vector change 200% greater than the vector change for LNC-C, the next greatest vector change. In PC 2 vs. PC 3 space all

of the LNC samples move away from the center of the zero value on both axes in roughly the same direction from 2001 to 2003. Change is very slight from 2001 and 2003 for the LNC samples as compared to the HSB samples.

Landscape Evaluation of Change

An examination of the entire Biscuit Fire Complex in the Siskiyou National Forest shows how the principal components of the M-Cone transformation relate changes in vegetation structure and cover at a landscape scale. The change in each of the first three principal components from 2001 - 2003 is examined against the change in NDVI using areas of high severity burn and little or no change as a guide.

The No Data values are the result of topographic shadowing of one or more of the MISR cameras. Many areas of the Siskiyou National Forest have terrain steep enough to shadow the extreme off-nadir MISR cameras. This occurred for both north and south facing slopes. The MI1B2T data product does not have recorded radiance values for these pixels. Since the PCA transformation of the MISR data is dependent upon input from 7 bands, loss of value in a single band leads to unrepresentative transformed values. Any pixel missing one or more camera returns was removed.

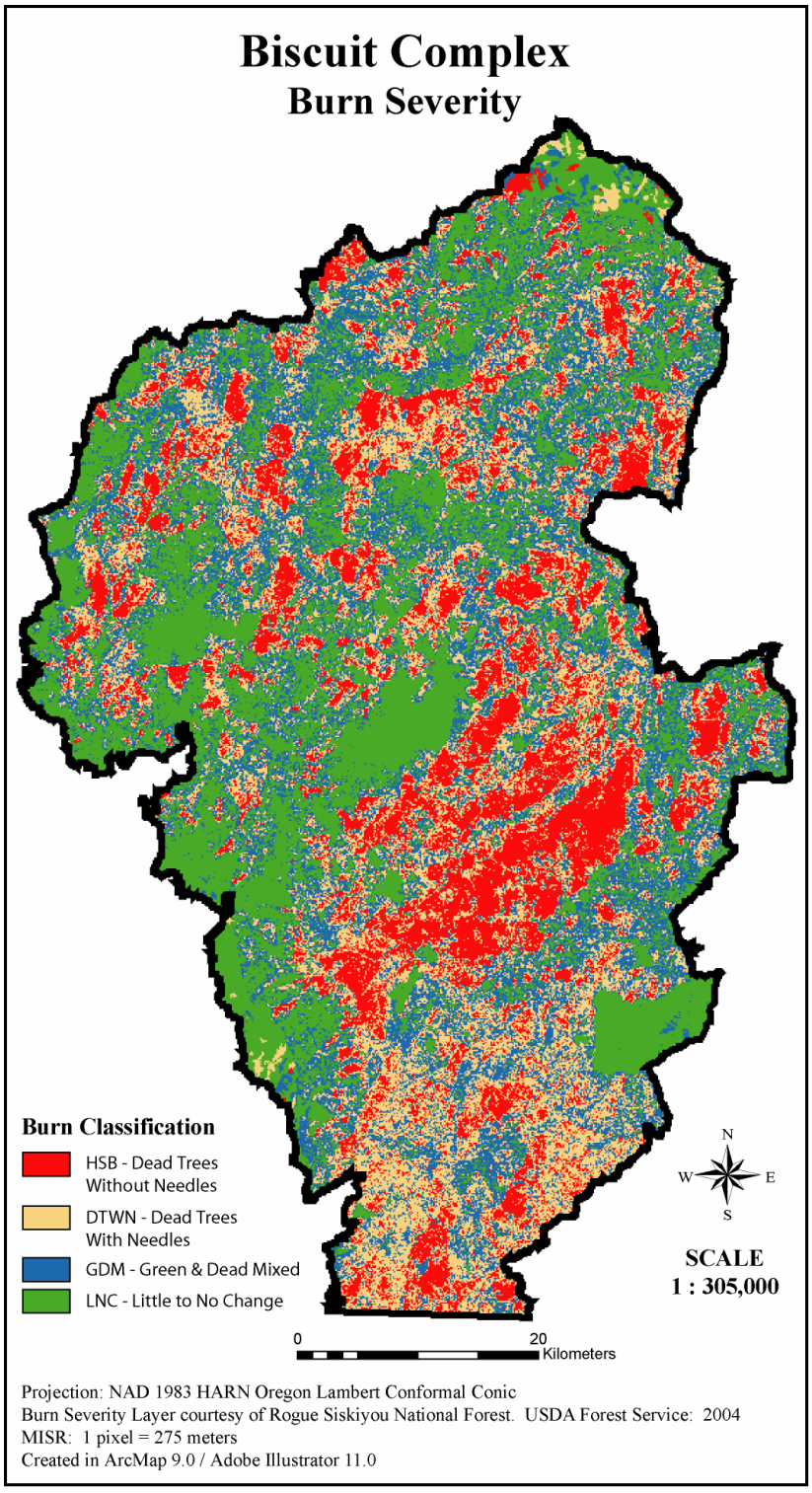

Figure 65. Biscuit Fire: U.S.D.A. Forest Service – Rogue River: Siskiyou National Forest burn severity map

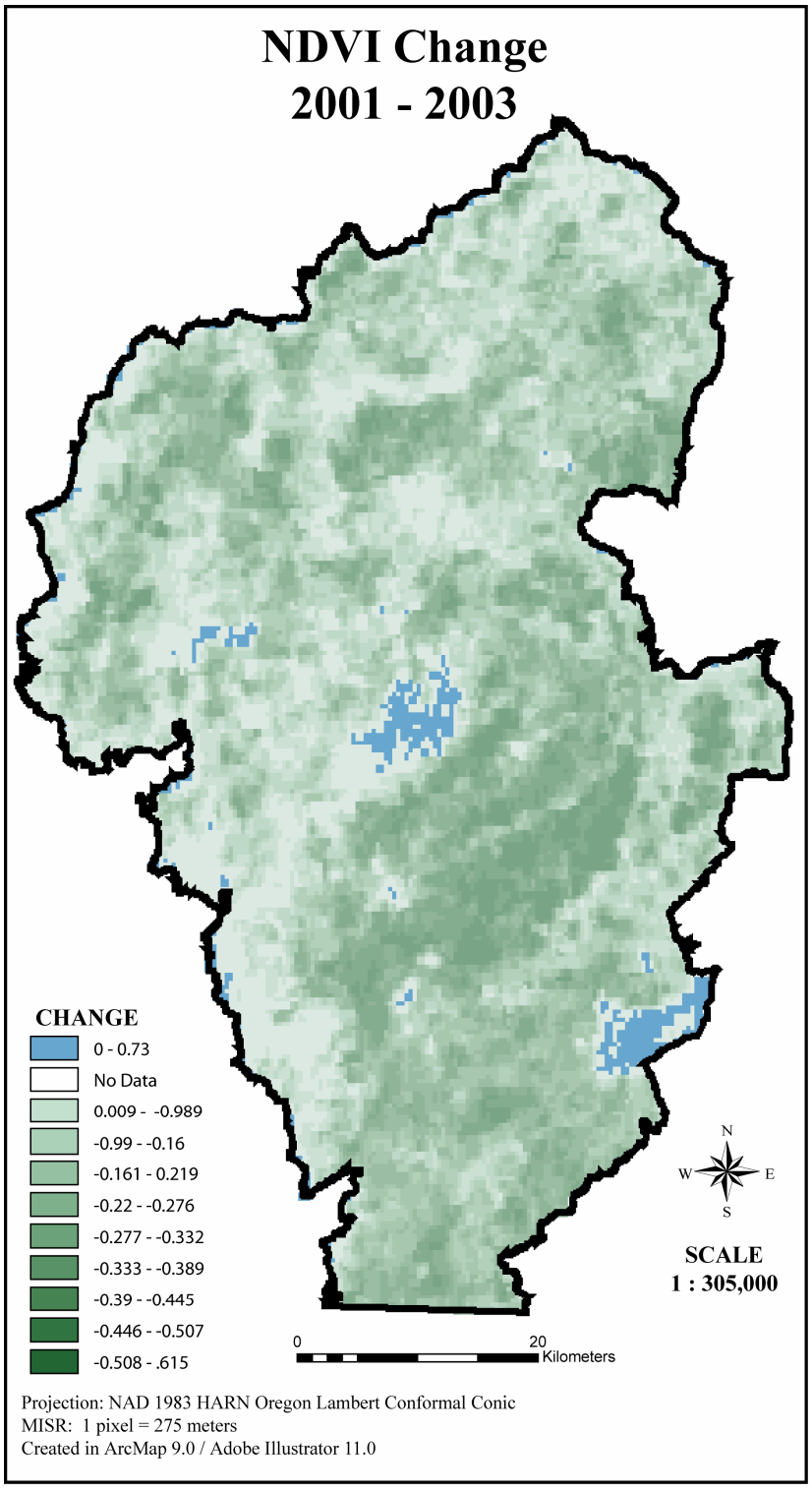

Figure 66. Biscuit Fire: Regional change in NDVI 2001 - 2003

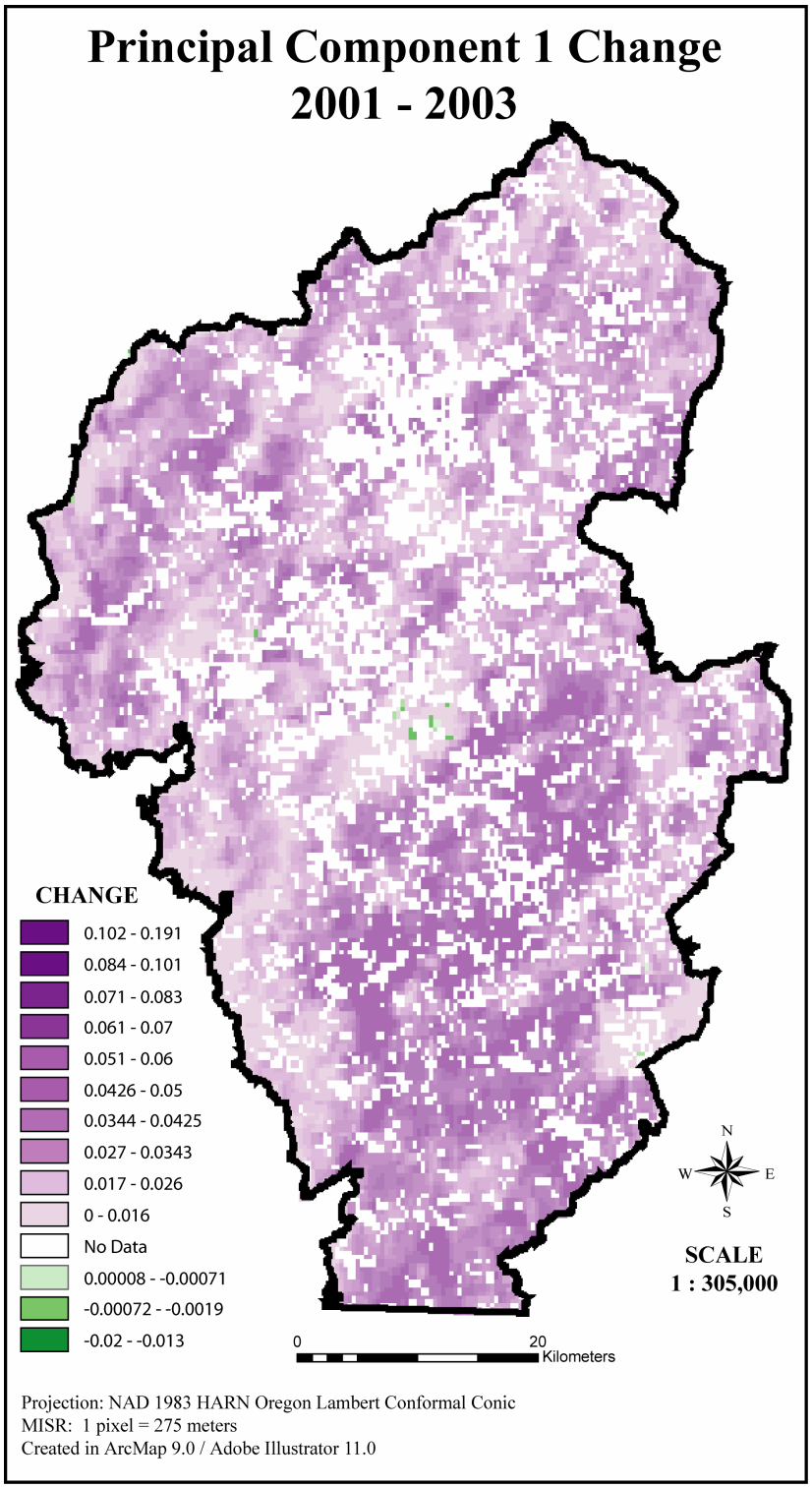

Figure 67. Biscuit Fire: Regional change in PC 1 2001 - 2003

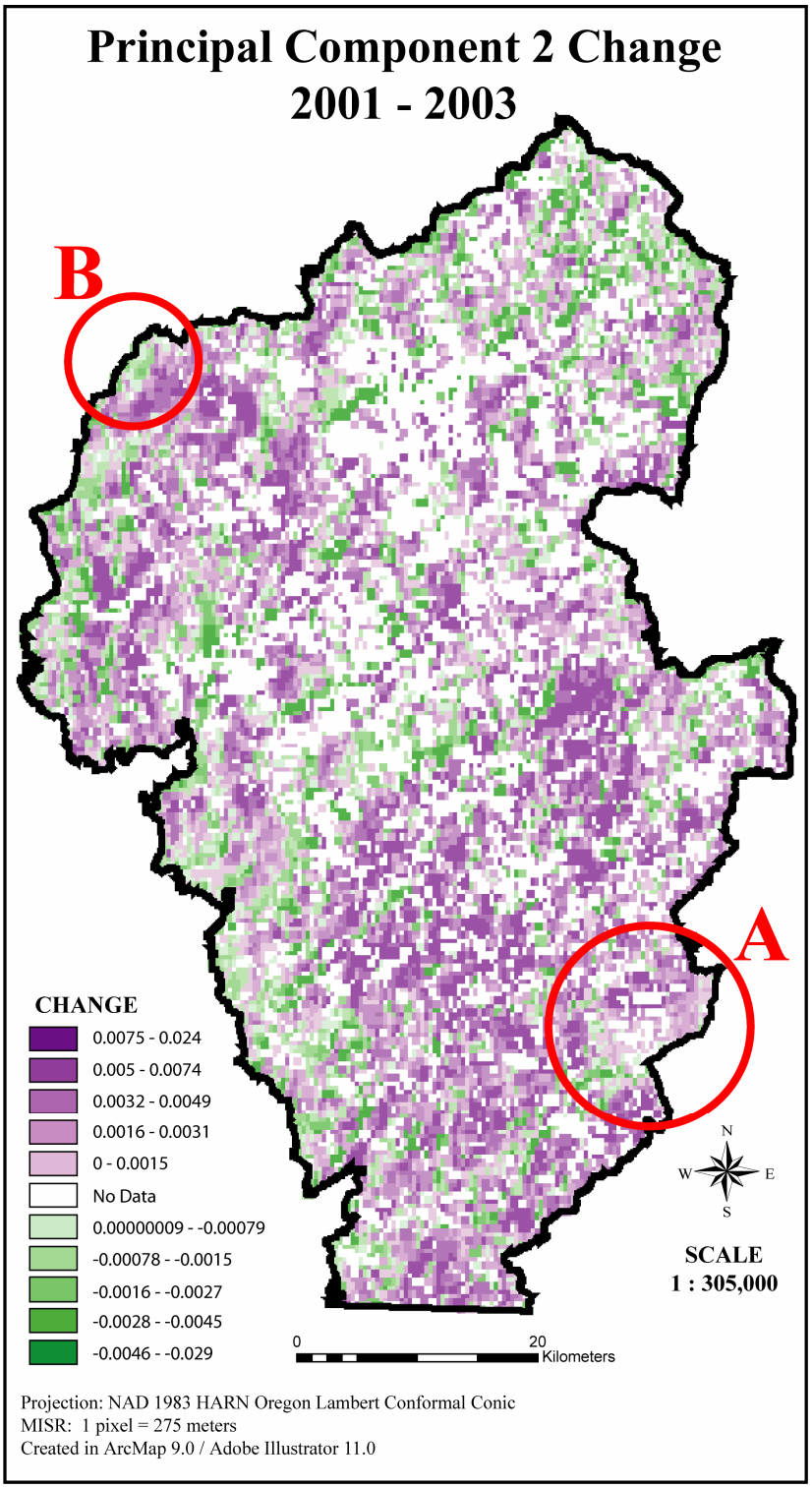

Figure 68. Biscuit Fire: Regional change in PC 2 2001 – 2003. The circled regions are areas of increasing (A) and decreasing (B) PC 2. Both circled areas exist on level terrain

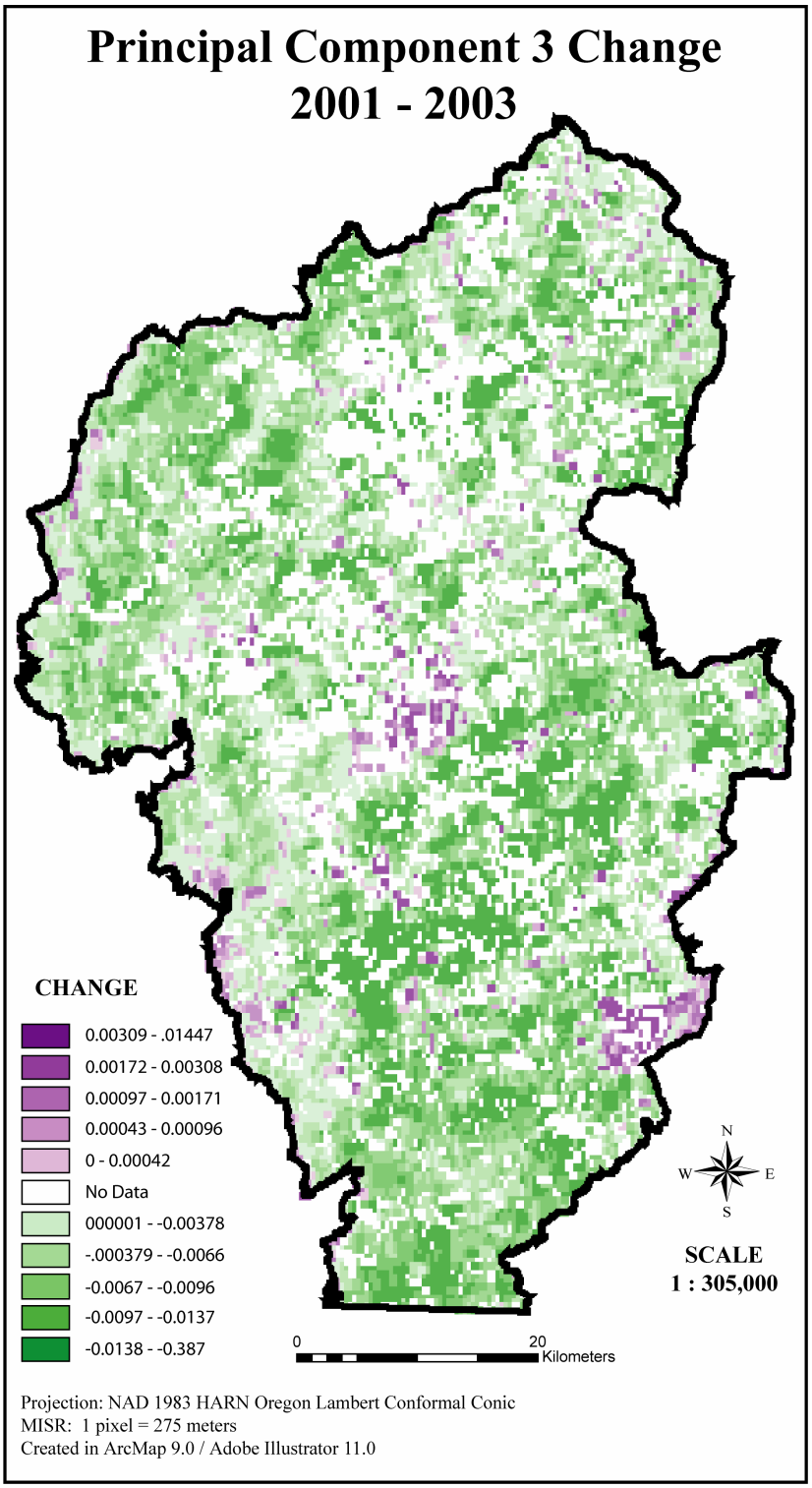

Figure 69. Biscuit Fire: Regional change in PC 3 2001 - 2003

Figure 65 displays the Biscuit Fire Perimeter with the areas of highest severity burn in red and the areas of little to no change in green. Figure 66 shows the change in NDVI from 2001 to 2003. The scale for the change in NDVI displays increasing negative change in NDVI as darkening shades of green. Any region where the NDVI increased is shown in blue. In very little of the Biscuit Fire Complex did NDVI increase in the year following the burn.

The change in PC 1 from 2001 to 2003 is shown in Figure 67. Increasing PC 1 values are shown as darkening shades of purple, decreasing values as darkening shades of green. PC 1 increased in nearly every region of the burned area. The very few areas that decreased in PC 1 are located in the areas that increased in NDVI. It is clear that the areas with the largest drop in NDVI after the burn are those areas with the largest increase in PC 1 after the burn. Viewed against the burn severity layer (Figure 65), the areas with the greatest increase in PC 1 were often the HSB areas and the areas of the greatest decrease in PC 1 were the areas of LNC.

The change in PC 2 from 2001 – 2003 is shown in Figure 68. The total area of increasing PC 2 is approximately twice as large as the area of decreasing PC 2. Visually, increasing and decreasing PC 2 values are not linked to the topography as the increasing and decreasing returns are found on ridgelines, on the north and south slopes of hills, and in valleys. The relationship between the change in PC 2 and the burn severity is inconsistent. Areas of LNC sometimes show increasing PC 2 value (Figure 68-circle A), and at other locations show varying levels of decreasing PC 2 value (Figure 68-circle B). Both of the circled areas are located on fairly level terrain. The areas of HSB generally show an increase in PC 2. This relationship is also inconsistent as areas of decreasing PC 2 are also in HSB areas. There is some visual correlation between areas increasing PC 2 value and the boundary between the regions of differing severity burn, although the large sections of missing pixels make this hard to determine.

The change in PC 3 from 2001 – 2003 is shown in Figure 69. The majority of the Biscuit burn area decreased in PC 3. The change in PC 3 shows very loose visual correlation to burn severity. The HSB regions of the Biscuit Complex are generally

those areas with the greatest decrease in PC 3. The LNC regions are generally the areas with increasing or slightly decreasing PC 3 value. The very few areas that increased in PC 3 are almost exclusively in LNC areas. Change in PC 3 shows some visual correlation in the clustering of increasing and decreasing PC 3 regions to regions of increasing and decreasing NDVI. The two large clusters of increasing NDVI are also the largest clusters of increasing PC 3. The areas of the greatest decrease in NDVI are often the areas of the greatest decrease in PC 3.

DISCUSSION

The PCA transformation of only the red bands was the most successful transformation in creating principal components directly correlated to measurable metrics. Initial PCA transformations were conducted with full spatial resolution of the nadir camera. The full nadir camera resolution was retained based on research by Kimes (2006) who found in a study that when using a neural network model with multi-angular and multi-spectral information from the AirMISR instrument, canopy heights of forests as measured by the Laser Vegetation Imaging Sensor (LVIS) sensor could be predicted with high accuracy. Component loadings from several samples at this spectral resolution failed to show any clear association between the camera angles and the factor loadings. That canopy height can be predicted from multi-angular imagery is suggestive that one of the principal components is correlated to some degree with vegetation height.

The interactively created sample for PCA was the alternative to a random sample of all available pixels in the processed MI1B2T data. The inability of the water, snow, and cloud masks to remove non-terrestrial features from the sample resulted in a PCA transformation unrepresentative of soils and vegetation. A random sample from all of the available MISR scenes was assessed for possible use as a sample for PCA. This random sample was created to contain approximately 2% (2.6 million pixels) of the available pixels in the processed MI1B2T data set. The MI1B2T had been converted to reflectance and corrected for the atmosphere by dark pixel subtraction. Clouds were masked using the MIRCCM with only 'high-confidence' cloud free pixels retained, and masked for snow and water using the masks created from the thresholds of NDSI and NDVI.

This attempt at a random sample of available pixels proved to be ill suited to the task due to the contamination of the sample by cloud, water, snow, and urban areas. The MIRCCM left too many clouds unmasked or only partially masked. The MIRCCM failed to mask high altitude, thin and wispy clouds, small clouds, and the edges of cloud banks. The threshold algorithms used to mask water and snow

suffered from the same shortcomings as the MIRCCM: There was simply too much information in a given scene that was not natural vegetation or soil that cleared the thresholds. Additionally, upon further investigation, the masks were removing vast areas of the Earth's surface suitable for sampling. The snow and cloud masks were removing very bright soil in shrubland areas, or a recently plowed field prior to planting.

The first three principal components were examined because they collectively explained 99.6% of the variance in the sample. Statistical confirmation as to the components of significance could not be fulfilled due to the irregularities of the sample used for PCA. The determination of the significance of the derived components was initially to be carried out using a Monte Carlo simulation known as the Preisendorfer N-rule (Preisendorfer et al., 1981). This requires 1000 random simulations that have the same statistical properties as the actual dataset. Due to the bi-modal distribution of the PCA sample, the random generation of sample simulations matching the statistical properties of the actual sample could not be accomplished. As the first three principal components collectively explained 99.6% of the variance of the sample, the remaining 4 components are in all likelihood noise and redundant information and were not examined.

Principal Component Findings

The first principal component, as the factor loadings indicate, is a measure of overall scene reflectance. As it is a linear sum of reflectance from seven angles, principal component 1 is representative of surface albedo. The temporal profile of all seven cameras at the Grassland - 2 illustrates this interpretation (Figure 10). The temporal profile of PC 1 is very similar to the profile of reflectance from all 7 cameras. Spikes in reflectance from multiple cameras are magnified in PC 1 (Figure 10 - sample date 5), while spikes in reflectance from a single camera are not reflected by an increase in PC 1 (sample dates 8 and 11). PC 1 in effect 'smoothes-out' the minor variations in reflectance in multiple cameras while at the same time magnifying moments of significant change in multiple cameras.

The phenological characteristics of the samples were loosely tied to the correlations between PC 1 and NDVI. Every one of the sites targeting the most phenologically dynamic vegetation, Deciduous, Grassland, Agriculture, showed high correlations between PC 1 and NDVI, but both Western Juniper sites also displayed correlations nearly equal to and sometimes higher than the sites with more pronounced phenology. Even though western juniper itself is relatively phenologically invariant, the grasses in the background would be phenologically dynamic. The Deciduous samples each showed the highest correlation between PC 1 and NDVI of any sample (Figure 73 a / b / c). The Evergreen sites generally showed the lowest correlation between PC 1 and NDVI of any of the vegetated correlation study sites.

The second principal component, as the factor loadings indicate, is a ratio contrasting aft and fore reflectance. PC 2 is a measure of the intensity and direction of shadows cast on the ground. Principal component 2 is representative of anisotropy.

At nearly all of the correlation study sites, PC 2 was shown to have high inverse correlation with both the solar zenith angle and with the relative azimuth angle between the sensor and the path of incident radiation. Also, at all of the sites, PC 2 showed higher inverse correlation with solar zenith angle than with the relative azimuth angle.

As the value of PC 2 is a ratio of reflectance between cameras, the temporal profile for various sites and samples are all essentially of the same general shape, bell-shaped with a peak value at or near the summer solstice, usually positive, and then dropping away from the summer solstice with minimum values at or near the winter solstice, always negative. This is evident at the latitude profile sites (Figure 35 and Figure 45). The five samples at the Shrubland latitude profile site have significantly higher scene reflectance than the Evergreen latitude profiles samples (Figure 9) and consequently have high magnitude positive and negative value at PC 2 (Figure 14), with exactly the same bell-shaped profile at each site (Figure 35).

This discrepancy in total range of PC 2 is related to the significantly lower PC 2 value is the months near winter solstice as the positive magnitude PC 2 value was nearly similar at each sample of a given site. Previous work (Asner et al., 1998) and preliminary results suggest that at the 275 meter spatial resolution of the MISR pixels, the percent of ground cover and the spatial distribution of the vegetation are the factors controlling the range of value in PC 2. It remains inconclusive what specific characteristics of a vegetated scene are driving the absolute magnitudes, and consequently the range of PC 2.

At the Evergreen site, sample Lat-A5, with the higher percentage of bare ground and far fewer trees than Lat-A2, had a greater range of PC 2 than Lat-A2. The samples at the Shrubland site show temporal profiles similar to the Evergreen samples. The Shrubland samples have similar PC 2 temporal profiles despite having very dissimilar temporal mean reflectance profiles. Each of the Shrubland samples shows a similar peak PC 2 value near the summer solstice. Like the Evergreen latitude profile samples, the variation in the range of PC 2 at the Shrubland samples is dictated by the lowest PC 2 return for samples. Unlike the Evergreen samples, the samples with the lowest PC 2 value at the Shrubland site (samples Lat-B1 and Lat-B5) are those samples with the highest percent ground cover, although this is based on visual interpretation of Landsat imagery.

Principal component 3 was not related to any available metric. Research is suggestive that that PC 3 is not entirely noise and may in fact be related to physical properties of the site. Examination of all samples from the correlation study sites shows that, almost without exception, the only sites with positive PC 3 value are for Grassland, Shrubland, and Agriculture sites. In evaluation of the Biscuit Complex Fire at the landscape scale, PC 3 did show positive visual correlation with burn severity. Also, the seven samples evaluated at the Biscuit Complex occupied the same space in the PC 1 vs. PC 3 dimension in 2001 and moved in very similar fashion through the PCA space after the burn.

The effect that topography on the principal components as examined at the Western Juniper sites shows that variations in topography between the two samples

causes different magnitudes of total reflectance at each sample and therefore differing magnitudes of PC 1 and PC 2 at each sample. Juniper A1, on rugged land, had lower temporal mean reflectance and PC 1 value than Juniper B3. Both samples had a nearly equal range of value in both reflectance and PC 1. The most noticeable difference between samples is that the PC 2 temporal profile of A2 is consistently lower, even in the near summer solstice months, than B3. Both Juniper samples are of similar land cover percentages detailed by the VCF and visual verification with Landsat. This suggests topography does have an impact on the PCA because even at the Shrubland latitude profile site, PC 2 was similar in the highest value months to the other 4 samples despite having completely disparate reflectance profile.

Analysis of the Biscuit Complex Fire

The performance of the first three principal components to characterize vegetation change in the Biscuit Fire Complex had varied success. Difficulty in interpreting the results of the change analysis stems from the unknown amount of noise inherent in the value of the principal components, and pixels lost due to topographic shadowing of one or more MISR cameras in the Siskiyou National Forest. The loss of information due to topographic shadowing of MISR cameras highlights a limitation on the transformation. Due to the nature of the MISR sensor, the extreme off-nadir cameras will often be shadowed by steep terrain. This terrain is not an issue to SVA sensors and the MISR cameras at and near nadir, but since the PCA depends upon input from all seven bands, loss of a single camera means loss of the entire pixel.

The first principal component showed the change in vegetation after the burn as a near mirror image of NDVI. Areas of severe drop in NDVI were the areas of high increase in PC 1. The characterization of PC 1 as a magnification of the aggregate camera reflectance is reinforced by the seven individual samples from the Biscuit Complex. The seven sampled regions from the burn all showed percent increase in PC 1 nearly similar, but higher, to the percent increase in mean reflectance.

The success of PC 2 to characterize the structural dynamics of vegetation at the Biscuit Fire Complex is much harder to determine. The loss of data to topographic shadowing makes it difficult to determine the spatial pattern of PC 2 increase and decrease throughout the burned and unburned areas. A rough spatial pattern indicates that PC 2 increased in areas of the highest severity burn and decreased in areas of lower severity burn or little to no change, although in some instances PC 2 both increased and decreased in areas of little to no change. Results indicated that the absolute positive magnitude of PC 2 is a function of the total reflectance of a scene. This being the case it would appear from the Biscuit samples that the areas of HSB burn decreased in vegetation cover as the PC 2 increased for each area of HSB and that vegetation cover actually increased at the LNC samples as PC 2 decreased at each sample. Examination of the cross-section of Biscuit samples showing the change in PCA space from 2001 – 2003 (Figure 58) supports this interpretation. As samples increased in PC 1 value after the burn, indicating increased reflectance, there was a corresponding increase in PC 2 as well.

The success of PC 3 to evaluate the structural dynamics of vegetation after the burn is difficult to determine. Principal component 3 did show some positive spatial correlation to the severity of burned areas at the landscape scale. The very few areas where PC 3 increased are the areas of little to no change. The areas where PC 3 decreased the most are the areas of the highest severity burn. Evaluation of the seven samples taken at the Biscuit Fire Complex shows that all samples from 2001 and 2003 exist on the leading edge of the M-Cone in PC 1 vs. PC 3 space and that the samples all followed the same trajectory of change in PC 1 vs. PC 3 space from 2001 – 2003. Whether these changes in PC 3 are the result of the sensitivity of PC 3 to specific physical characteristics of the vegetation changing after the fire or is simply PC 3 changing as a source of noise is unclear. However, that the samples of Douglas fir exist in the same PC 1 vs. PC 3 M-Cone space as other evergreen samples, and that PC 3 exhibits a spatial pattern similar to burn severity and changing NDVI at all is suggestive that PC 3 may carry unique structural information on vegetation.

Sources of Error

The primary sources of error in this study are related to camera reflectance, preferential sampling in the sample used for PCA, and temporal inconsistency between study sites. To a lesser extent there is some error associated with the reprojection of the MISR orbits to a geographic lat / lon coordinate system, and with the spatial resampling of ancillary datasets.

Occasionally the reflectance at any given camera was obviously wrong. Any sample dates determined to have unrepresentative, incorrect reflectance were removed from analysis. The determination as to whether a camera's reflectance was too far removed from the norm to remain in the study is subjective. A camera's reflectance was compared against the same camera's reflectance for every date in a sample. If the reflectance of any camera at one date was orders of magnitude higher or lower than the reflectance of the same camera at any other date, and the intensity of the increase or decrease was not a common occurrence over time at the sample, then that date was removed. This occurrence was almost exclusively related to the winter months at a site (November – February) and is most likely the result of snow contamination.

The error associated with the sample used for the PCA is a result of the spatial constraints imposed by the desire to sample only the same pixel at all dates for a particular vegetation class. The PCA sample is a stratified sample, with an unequal number of pixels sampled at each site and month, an unequal number of vegetation classes sampled at each site and month, and certain vegetation classes have been preferentially sampled. Spatially, the location of all samples within the conterminous United States limits all samples to a specific range of possible solar illumination angles.

There is also a temporal inconsistency between samples used in these analyses. In analysis of the samples from the correlation study sites, not all samples from each site share the same temporal range of dates sampled, nor the same number of dates sampled. For this reason the differences in reflectance and range of magnitude for the principal components may be the result of unequal temporal

sampling and not the result of physical differences at the site. Due to the lack of samples, the spatial and temporal correlation of samples, heteroscedacity, and the non-normal distribution of the sample data, the samples used in the study sites do not meet the statistical requirements of randomness.

The value of PC 1 and PC 2 will also be greatly influenced by variations in the local solar illumination angle. The value of the principal components, as a function of reflectance from seven angles, is directly dependent upon solar elevation and the relative azimuth angle between the sensor and the sun. At the study sites, variation in the solar illumination leads to a discrepancy between the principal components of essentially identical vegetated scenes. The influence of the angle of solar elevation, and of the relative azimuth angle between the sensor and the sun will require that for a spatiotemporal analysis, the angles of solar illumination and view should be as nearly equal at all sites and times as possible.

CONCLUSIONS

This study is an initial attempt at examining the feasibility of a PCA of multi-angular, red band imagery to characterize the structural dynamics of vegetation. The scope of the study was not to directly quantify the principal components of the PCA to metrics of vegetation structure, but to see if the principal components derived from a multi-angular, multi-temporal sample of MISR data could be correlated to any metrics of vegetation structure at all.

A principal components transformation of MISR data results in a new set of uncorrelated components, where the first three principal components explain greater than 99% of the variance in the sample. While it could not be statistically verified, the remaining four components likely represent noise or redundant information. The first two principal components were correlated to an index of vegetation and to solar illumination, respectively. Principal component 1 is representative of scene albedo, and principal component 2 of surface anisotropy. The third principal component could not be correlated to any available metric, but preliminary results suggest that there may be unique information present in principal component 3. The ability of the principal components to relate the structural dynamics in vegetation at the Biscuit Complex Fire was partially successful. Principal component 2, representative of anisotropy, showed an increase from 2001 to 2003 in most of the HSB areas in the Biscuit Complex, indicating a loss of tree cover, and change in the spatial distribution of trees and other vegetation in relation to each other. The ability of the transformation developed for this study to characterize the structure of vegetation is scale dependent, and representative of larger scale structural characteristics such as canopy gap fraction. None of the components could be definitively related to more fine-scale changes in the vegetation such as the sub-canopy three-dimensional scatters: leaves, twigs, standing litter.

PCA of the red bands from MISR cameras Cf – Ca results in two components directly correlated to measurable properties of a vegetated scene. Viewed in PCA space, classes of vegetation as identified by the 1992 NLCD appear in distinct and

unique regions of space. The phenological cycle of vegetation is apparent in the PCA space and is visible in the dimensions defined by PC 1 vs. PC 2 and PC 1 vs. PC 3.

Principal component 1 is a measure of overall reflectance, nearly similar to the reflectance of the MISR nadir camera, but more sensitive to fluctuations captured by four or more cameras. A high inverse correlation exists between PC 1 and NDVI for nearly every vegetated sample. Examination of the temporal profile of PC 1 against the nadir reflectance and mean reflectance of the correlation study sites indicates that PC 1 may be a better measure of surface albedo than what the nadir camera alone can relate.

Principal component 2 is a measure of anisotropy, driven by changing solar illumination. There is high inverse correlation between PC 2 and solar zenith angle and PC 2 and the relative azimuth angle between the sensor and the angle of incident radiation for nearly every vegetated sample studied. Principal component 2 is representative of surface anisotropy and, at the 275 meter MISR pixel scale, most likely representative of the percent of ground cover and / or the spatial distribution of vegetation in a pixel.

Principal component 3 could not be correlated with any available metric. The temporal variations in PC 3 are erratic and with considerable magnitudes of variation as compared to the first two principal components. There is however evidence to suggest that PC 3 carries unique information on vegetation.

The vegetation change at the Biscuit Complex Fire on a landscape scale was visible when viewed individually by principal components. The change was most marked in PC 1, as an inverse of the change in NDVI. The change was less clear in PC 2 mostly due to the large amount of information missing because of topographic shadowing of one or more of the MISR cameras. The response of PC 2 to burn severity was varied and not constant across the burned area. In PC 3 could be seen a pattern of change similar to the spatial pattern of burn severity. Like PC 2, the pattern of PC 3 in relation to burn severity was not consistent, but suggestive that the change in PC 3 was a result of more than simply noise in the signal. The Biscuit Fire

Complex was not a suitable study site to evaluate vegetation change using this technique due to the high loss of pixels to topographic shadowing.

A principal components analysis of multi-angle imagery of only the red spectrum of the EMS results in three principal components explaining greater than 99% of the variance in the sample, with the first two principal components directly correlated to measurable properties of the scene. Preliminary results suggest that unique information about the properties of vegetation may be contained in the third principal component.

The PCA transformation of MISR data as presented in this study holds promise for improved vegetation indices and estimates of biomass at a global scale. As a linear sum of reflectance sampled from 7 angles, principal component 1 is a more complete sample of albedo from a vegetated surface and is not biased to a single view direction as measurements from a only a nadir camera would be. Initial investigation into the effects of varying vegetation density and land cover type on principal component 2 indicates that surface anisotropy as characterized by PC 2 is representative of percentages of ground cover and the spatial distribution of vegetation; and also possibly of vegetation height.

The M-Cone vegetation space as defined by the axes of PC1 and PC 2 shows that the transformed data space is successful at separating classes of vegetation into distinct regions of PCA space. The 'Badge of Trees' from the multi-spectral Tasseled Cap transformation is visible in PCA space, on and near the tip and leading negative PC 2 edge of the M-Cone where the Evergreen and Deciduous correlation study samples are located. The PC 1 vs. PC 2 space is useful in showing the regional change after a stand-replacing disturbance as demonstrated at the Biscuit Complex Fire.

There is no established range of noise associated with the M-Cone transformation. Principal components display a normal range of variation that could result in misleading interpretations of component values if not accounted for in analysis. The temporal profile of PC 2 illustrates this variation in component value with the series of spikes and dips in PC 2 value around a mean trend. The PCA

sample built for this study was created to represent a wide variety of vegetation and soils reflectance. PCA however, is a sensor specific and data dependent transformation due to the inherent differences between instruments, resulting in different coefficients of rotation for every unique dataset (Crist 1985). The coefficients of rotation derived in this study cannot be directly applied to other sensors, or directly to another MISR data set.

This study shows how a PCA of multi-angle imagery of a single spectral band can be used to provide information on the structural dynamics of vegetated scenes not possible from SVA multi-spectral remote sensing. The PCA transformation presented in this study divides the information obtained from a multi-angle sample of reflectance into two unique metrics. Principal component 1 is a measure of albedo, and principal component 2, a measure of anisotropy. The characterization of anisotropy in PC 2 provides a single metric describing the spatial distribution and canopy gap fraction of vegetated scenes. This is dependent upon the spatial resolution of the MISR imagery used and may not be constant at different scales. The ability to assess the 'patchiness' of vegetation can provide further insight into the three-dimensional variations in vegetation not possible with SVA vegetation metrics. In a future study, it would be advisable to stratify samples by solar zenith angle rather than by date as the variation in solar illumination is more a controlling factor in the PCA than the date of imagery.

REFERENCES

Asner, G. P. (1998). "Biophysical and Biochemical Sources of Variability in Canopy Reflectance." Remote Sensing of Environment **64**: 234-253.

Asner, G. P., B. H. Braswell, D. S. Schimel and C. A. Wessman (1998). "Ecological research needs from multiangle remote sensing data." Remote Sensing of Environment **63**(2): 155-165.

Braswell, R., X. Xiao, S. Boles, S. Frolking, B. Moore III and Q. Zhang (2003). "Sensitivity of vegetation indices to atmospheric aerosols: Continental-scale observations in Northern Asia." Remote Sensing of Environment **84**(3): 385-392.

Carr, J. R. (2002). Data Visualization In The Geosciences. Upper Saddle River, New Jersey, Prentice-Hall, Inc.

Chavez, P. S. J. (1989). "Extracting Spectral Contrast in Landsat Thematic Mapper Image Data Using Selective Principal Components Analysis." Photogrammetric Engineering and Remote Sensing **55**(3): 339-348.

Chengquan, H., B. Wylie, L. Yang, C. Homer and G. Zylstra (2002). Derivation of a Tasseled Cap Transformation Based on Landsat 7 At-Satellite Reflectance. USGS**:** 1-10.

Chopping, M. J., L. H. Su, A. Rango and C. Maxwell (2004). "Modeling the reflectance anisotropy of Chihuahuan Desert grass-shrub transition canoy-soil complexes." Internation Journal of Remote Sensing **25**(14): 2725-2745.

Cohen, W. B., T. K. Maiersperger, D. P. Turner, W. D. Ritts, D. Pflugmacher, R. E. Kennedy, A. Kirschbaum, S. W. Running, M. Costa and S. T. Gower (2006). "MODIS Land Cover and LAI Collection 4 Product Quality Acrosss Nine Sites in the Western Hemisphere." IEEE Transactions on Geoscience and Remote Sensing **44**(7): 1843-1857.

Crippen, R. E. (1987). "The regression intersection method of adjusting image data for band ratioing." Internation Journal of Remote Sensing **8**(2): 137-155.

Crist, E. P. (1983). The Thematic Mapper Tasseled Cap - - A Preliminary Formulation. Symposium on Machine Processing of Remotely Sensed Data - Proceedings, W. Lafayette, IN, Institute of Electrical and Electronics Engineers.

Crist, E. P. (1985). "A TM Tasseled Cap Equivalent Transformation for Reflectance Factor Data." Remote Sensing of Environment **17**: 301-306.

Crist, E. P. and R. C. Cicone (1984). A Physically-Based Transformation of Thematic Mapper Data - The TM Tasseled Cap. IEEE Transactions on Geoscience and Remote Sensing. **GE-22:** 256-263.

Crist, E. P. and R. C. Cicone (1984a). "Application of the Tasseled Cap Concept to Simulated Thematic Mapper Data." Photogrammetric Engineering and Remote Sensing **50**(3): 343-352.

Crist, E. P. and R. J. Kauth (1986). "The Tasseled Cap De-Mystified." Photogrammetric Engineering and Remote Sensing **52**(1): 81-86.

Crist, E. P., R. Laurin and R. C. Cicone (1986). Vegetation and soils information contained in transformed Thematic Mapper data. Proceedings of IGARSS' 86 Symposium, Paris.

Curran, P. J. (1983). "Estimating Green LAI from Multispectral Aerial Photography." Photogrammetric Engineering and Remote Sensing **49**: 1709-1720.

Davis, J. C. (1973). Statistics and Data Analysis in Geology, John Wiley & Sons, Inc.

Diner, D. J., G. P. Asner, R. Davies, Y. Knyazikhin, J.-P. Muller, A. W. Nolin, B. Pinty, C. B. Schaaf and J. Stroeve (1999). New Directions in Earth Observing: Scientific Applications of Multiangle Remote Sensing, Bulletin of the American Meteorological Society**:** 2209-2227.

Diner, D. J., J. C. Beckert, T. H. Reily, C. J. Bruegge, J. E. Conel, R. A. Kahn, J. V. Martonchik, T. P. Ackerman, R. Davies, S. A. W. Gerstl, H. R. Gordon, J. P. Muller, R. B. Myneni, P. J. Sellers, B. Pinty and M. M. Verstraete (1998). "Multi-angle Imaging SpectroRadiometer (MISR) description and experiment overview." IEEE Transactions on Geoscience and Remote Sensing **36**: 1072-1087.

Garbulsky, M. F. and J. M. Paruelo (2004). "Remote sensing of protected areas to derive baseline vegetation functioning characteristics." Journal of Vegetation Science **15**(5): 711-720.

Gauch, H. G. J. (1982). Multivariate analysis in community ecology. Cambridge, MA, Cambridge University Press.

Gerard, F. F. and P. R. J. North (1997). "Analyzing the Effect of Structural Variability and Canopy Gaps on Forest BRDF Using a Geometric-Optical Model." Remote Sensing of Environment **62**(1): 46-62.

GLCF. Global Land Cover Facility: University of Maryland. Earth Science Data Interface. 11/10/2006. http://glcfapp.umiacs.umd.edu:8080/esdi/index.jsp.

Gobron, N., B. Pinty, M. M. Verstraete, J. V. Martonchik, Y. Knyazikhin and D. J. Diner (2000). "Potential of multiangular spectral measurements to characterize land surfaces: Conceptual approach and exploratory application." Journal of Geophysical Research **105**(D13): 17,539-17,549.

Gobron, N., B. Pinty, M. M. Verstraete, J.-L. Widlowski and D. J. Diner (2002). "Uniqueness of Multiangular Measurements - Part II: Joint Retrieval of Vegetation Structure and Photosynthetic Activity from MISR." IEEE Transactions on Geoscience and Remote Sensing **40**(7): 1574-1592.

Jackson, R. D. (1983). "Spectral Indices in *n*-Space." Remote Sensing of Environment **13**: 409-421.

Jensen, J. R. (2000). Remote Sensing of the Environment: An Earth Resource Perspective. Upper Saddle River, NJ, Prentice-Hall, Inc.

Jenson, S. K. and F. A. Waltz (1979). Principal Components Analysis and Canonical Analysis in Remote Sensing. American Society of Photogrammetry 45th Annual Meeting, Washington D.C.

Kimes, D. S., J. Gastellu-Etchegorry and P. Esteve (2002). "Recovery of forest canopy characteristics through inversion of a comlex 3D model." Remote Sensing of Environment **79**: 320-328.

Kimes, D. S., Ranson, K.J., Sun, G., Blair, J.B. (2006). "Predicting lidar measured forest vertical structure from multi-angle spectral data." Remote Sensing of Environment **100**: 503 - 511.

Kimes, D. S. and P. J. Sellers (1985). "Inferring hemispherical reflectance of the Earth's surface for global energy budgets from remotely sensed nadir or directional radiance values." Remote Sensing of Environment **18**(3): 205-223.

LCI. U.S.G.S. Land Cover Institute. National Land Cover Dataset 1992. 3/2006. 11/10/2006. http://landcover.usgs.gov/natllandcover.php.

Martonchik, J. V., D. J. Diner, B. Pinty, M. M. Verstraete, R. B. Myneni, Y. Knyazikhin and H. R. Gordon (1998). "Determination of land and ocearn reflective, radiative, and biophysical properties using multiangle imaging." IEEE Transactions on Geoscience and Remote Sensing **36**(1266-1281).

MISRa. N.A.S.A. Langley Atmospheric Science Data Center. Multi-angle Imaging SpectroRadiometer (MISR) Langley DAAC Project Guide. 4/7/2006. 10/10/2006. <http://eosweb.larc.nasa.gov/GUIDE/campaign_documents/misr_ov.html>.

MISRb. N.A.S.A. Langley Atmospheric Science Data Center. MISR Level 1 Products Quality Statement. 4/10/2006. 11/10/2006. <http://eosweb.larc.nasa.gov/PRODOCS/misr/Quality_Summaries/L1_Products_20040310.html>.

MODIS-VCF. U.S.G.S.-N.A.S.A. Land Processes Distributed Active Archive Center. MODIS/Terra Vegetation Continuous Fields Product Description. 7/28/2005. 7/10/2006. http://edcdaac.usgs.gov/modis/mod44b.asp.

Myneni, R. B., C. D. Keeling, C. J. Tucker, G. Asrar and R. R. Nemani (1997). "Increased plant growth in the northern high latitudes from 1981-1991." Nature **386**: 689-702.

NED. U.S.G.S. National Elevation Dataset. 8/2006. 11/10/2006. http://ned.usgs.gov/.

Ni, W., X. Li, C. E. Woodcock, J. L. Roujean and R. Davis (1997). "Transmission of solar radiation in boreal conifer forests: measurements and models." Journal of Geophysical Research **102**(D24): 29,555-29,566.

Ni, W., C. E. Woodcock and D. L. B. Jupp (1999). "Variance in Bidirectional Reflectance over Discontinuous Plant Canopies." Remote Sensing of Environment **69**(1): 1-15.

Nicodemus, F. E., J. C. Richmond, J. J. Hsia, I. W. Ginsberg and T. Limperis (1977). Geometrical Considerations and Nomenclature for Reflectance. Washington D.C., National Bureau of Standards: U.S. Department of Commerce**:** 67.

Nolin, A. W. (2004). "Towards retrieval of forest cover density over snow from the Multi-angle Imaging SpectroRadiometer (MISR)." Hydrologic Processes **18**: 3623 - 3636.

OR-GEO. Oregon Geospatial Enterprise Office (GEO). Forested Lands. 10/26/2006. 11/10/2006. http://www.gis.state.or.us/data/alphalist.html.

Perry, C. R. J. and L. F. Lautenschlager (1984). "Functional Equivalence of Spectral Vegetation Indices." Remote Sensing of Environment **14**: 169-182.

Pinty, B., J.-L. Widlowski, M. M. Verstraete and D. J. Diner (2002). "Uniqueness of multiangular measurements - part I: an indicator of subpixel surface

heterogeneity from MISR." IEEE Transactions on Geoscience and Remote Sensing **40**: 1560-1573.

Preisendorfer, R. W., F. W. Zwiers and T. P. Barnett (1981). "Foundations of Principal Component Selection Rules." Scripps Institution of Oceanography: University of California, San Diege **81-4**: 192.

Running, S. W., L. Queen and M. Thornton (2000). "The Earth Observing System and forest management." Journal of Forestry **98**(6): 29-31.

Russel, C. A., J. R. Irons and P. W. Dabney (1997). "Bidirectional reflectance of selected BOREAS site from multiangle airborne data." Journal of Geophysical Research **102**(D24): 29505 - 29516.

Schaepman-Strub, G., M. E. Schaepman, T. E. Painter, S. Dangel and J. V. Martonchik (2006). "Reflectance quantities in optical remote sensing - definitions and case studies." Remote Sensing of Environment **103**: 27-42.

Schimel, D. S. (1995). "Terrestrial biogeochemical cycles: global estimates with remote sensing." Remote Sensing of Environment **51**(1): 49-56.

Singh, A. and A. Harrision (1985). "Standardized Principal Components." International Journal of Remote Sensing **6**(6): 883-896.

USDA-FS. U.S.D.A. F.S. Rogue River - Siskiyou National Forest. Biscuit Fire Recovery Project: Final Environmental Impact Statement. 6/1/2004. 11/10/2006. http://www.fs.fed.us/r6/rogue-siskiyou/biscuit-fire/feis.shtml.

Widlowski, J.-L., B. Pinty, N. Gobron and M. M. Verstraete (2001). "Characterization of surface heterogeneity detected at the MISR/TERRA subpixel scale." Geophysical Research Letters **28**(24): 4639-4642.

Wilderness. The Wilderness Society. Summary of the Biscuit Complex Fire, Oregon/Calilfornia. 11/10/2006. http://www.wilderness.org/Library/Documents/WildfireSummary_Biscuit.cfm .

Xavier, A. S. and L. S. Galvao (2005). "View angle effects on the discrimination of selected Amazonian land cover types from a principal-component analysis of MISR spectra." Internation Journal of Remote Sensing **26**(17): 3797-3811.

Zhang, Y., Y. Tian, R. B. Myneni, Y. Knyazikhin and C. E. Woodcock (2002). "Assessing the information content of multiangle satellite data for mapping biomes I. Statistical analysis." Remote Sensing of Environment **80**(3): 418-434.

APPENDICES

APPENDIX A: Correlation Study Sites in PCA Space

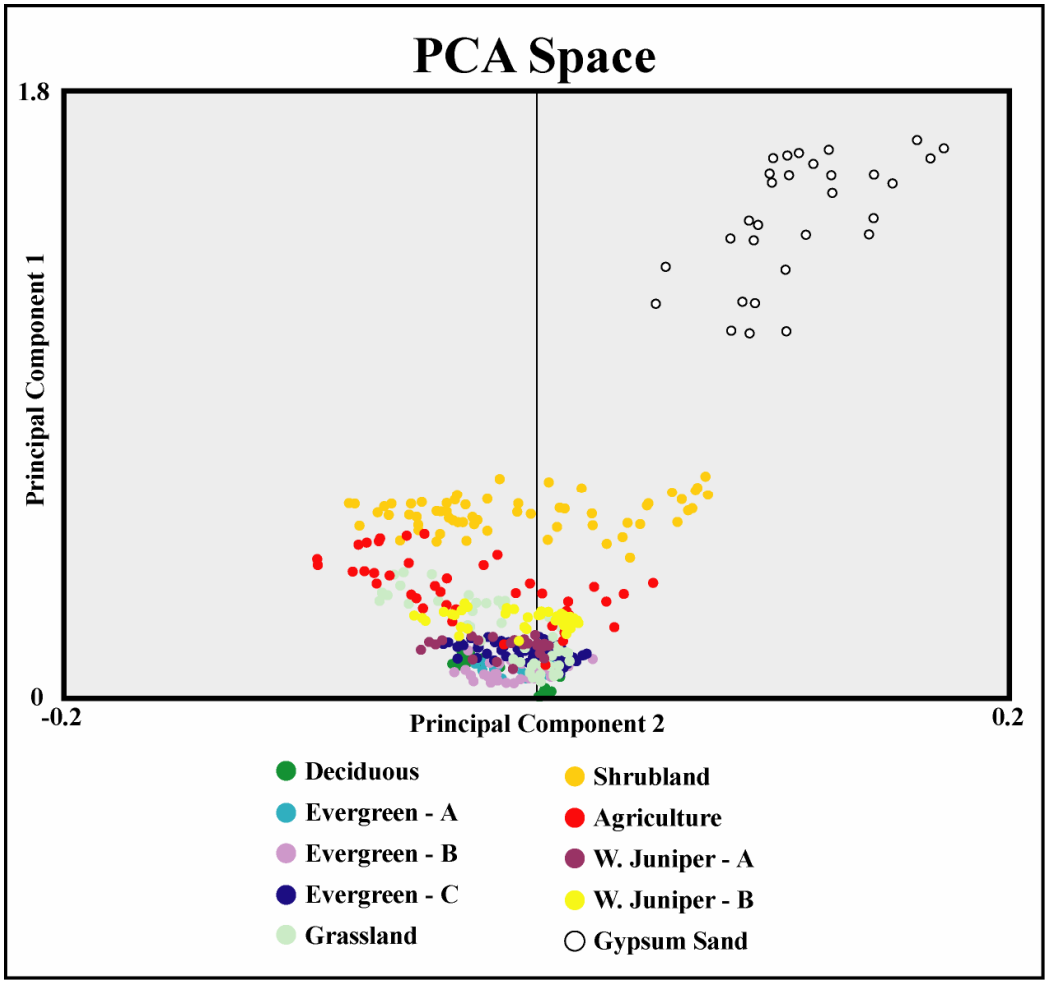

Figure 70. Correlation study site samples in PCA space: PC 1 and PC 2

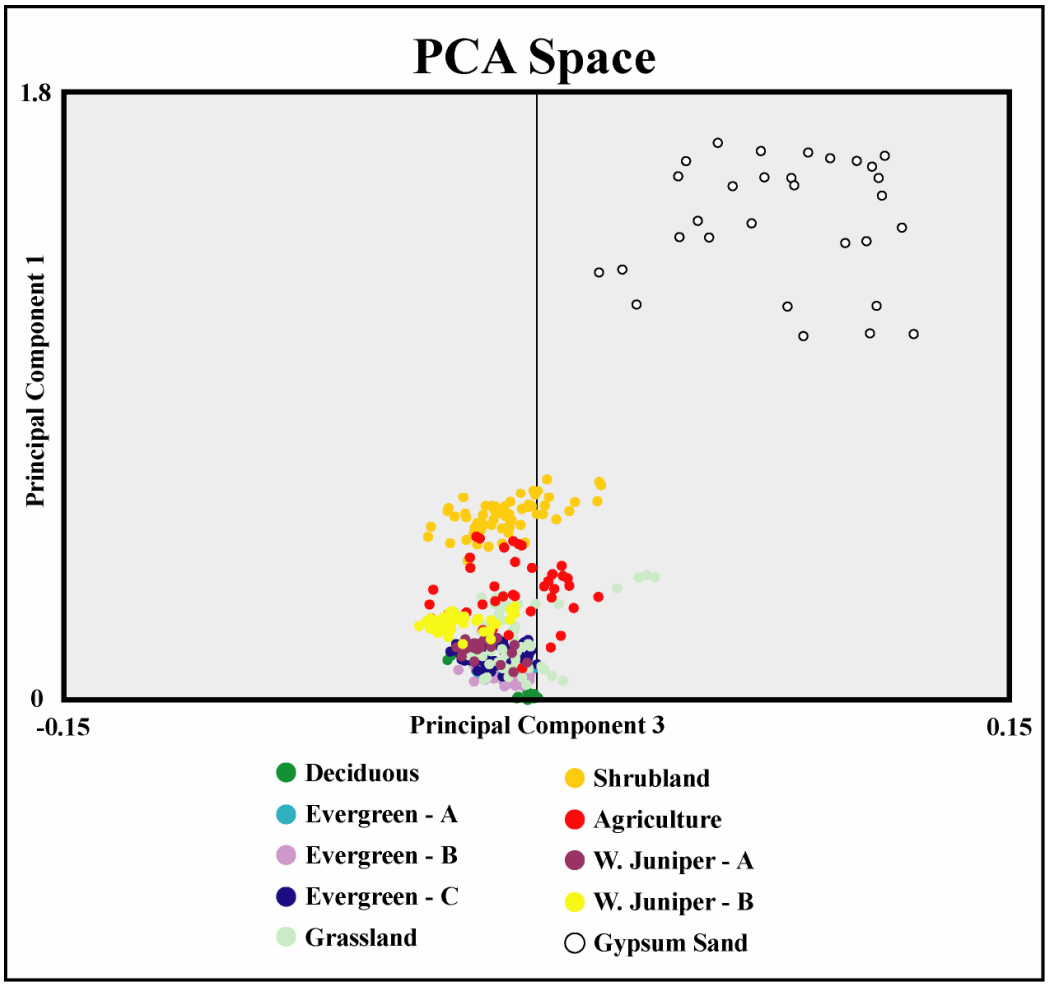

Figure 71. Correlation study site samples in PCA space: PC 1 and PC 3

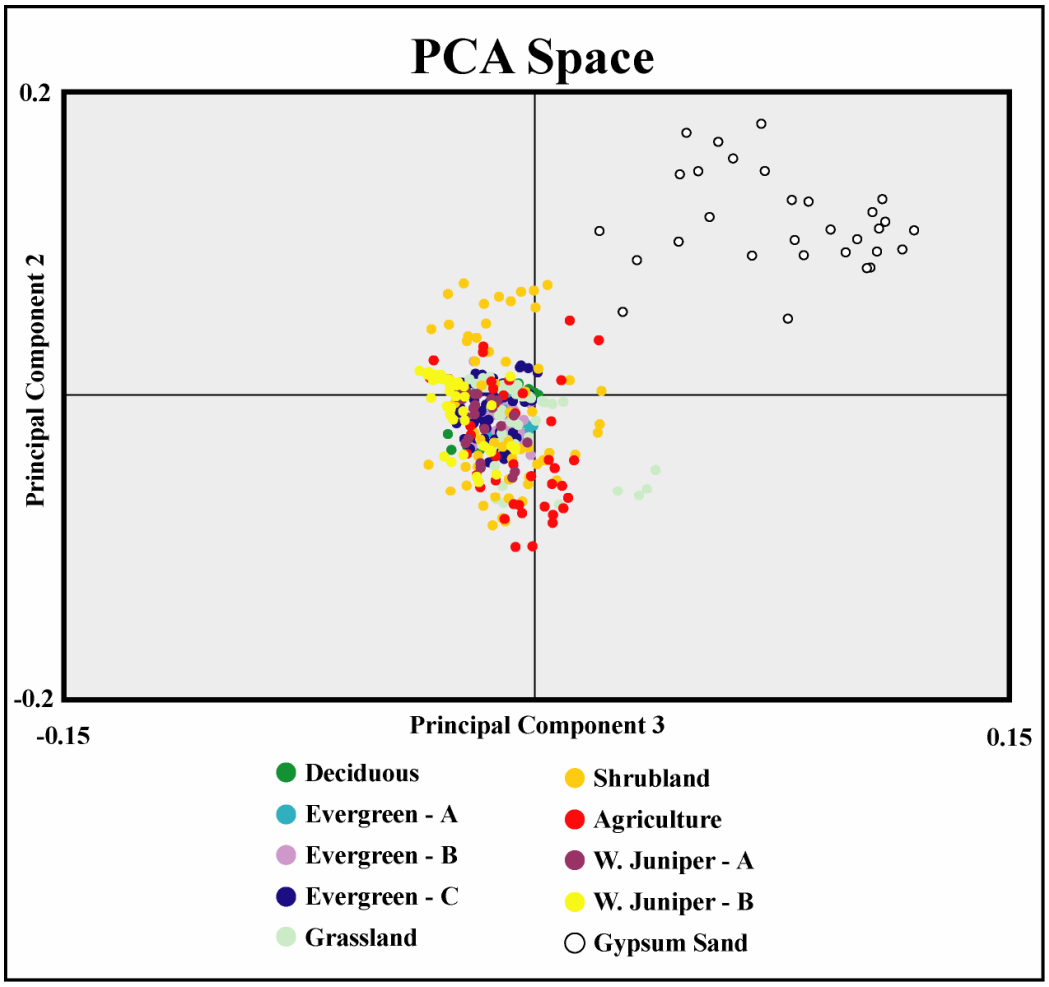

Figure 72. Correlation study site samples in PCA space: PC 2 and PC 3

APPENDIX B: Correlation Plots: Principal Component 1 vs. NDVI

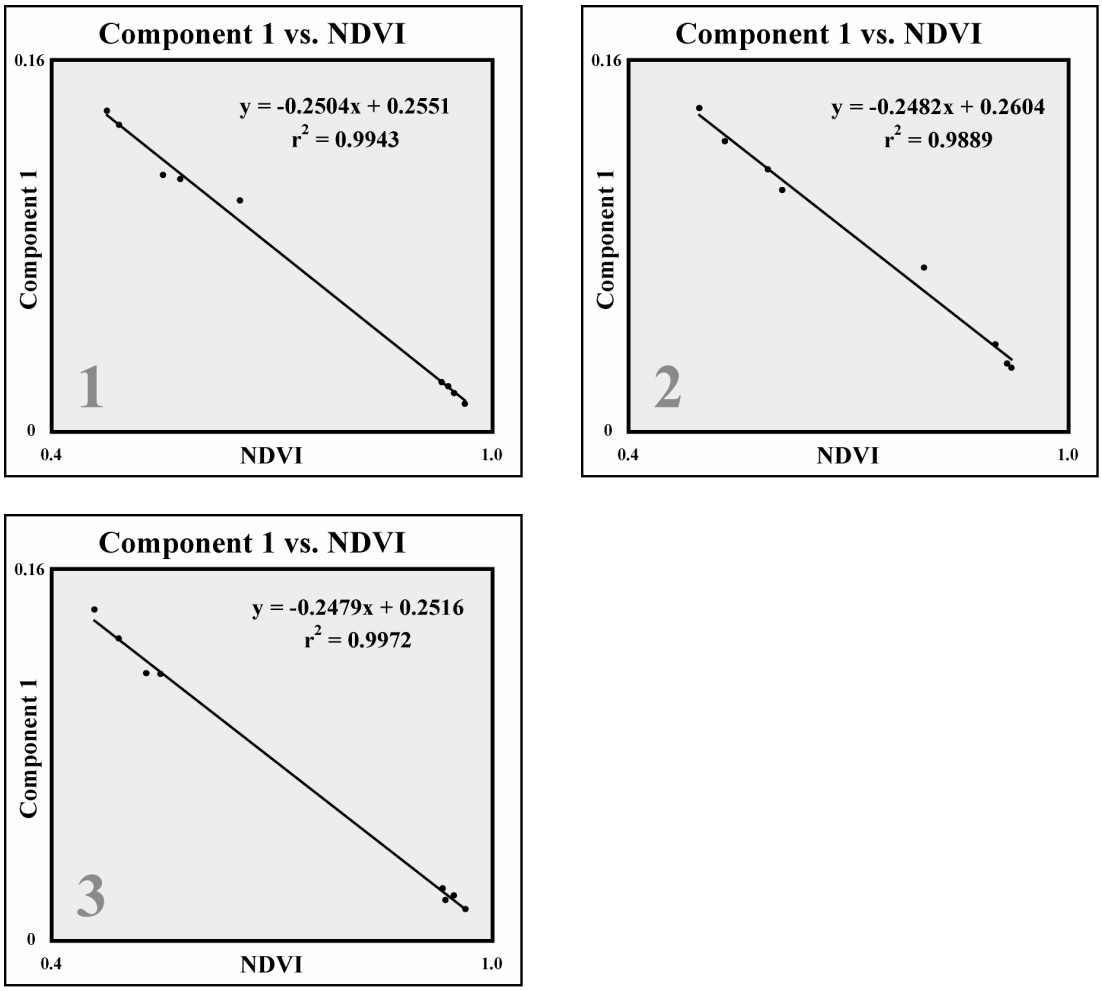

Figure 73 a / b / c. Correlation plots of PC 1 vs. NDVI: .a The top left plot shows Deciduous sample 1 .b The top right plot shows Deciduous sample 2 .c The bottom left plot shows Deciduous sample 3

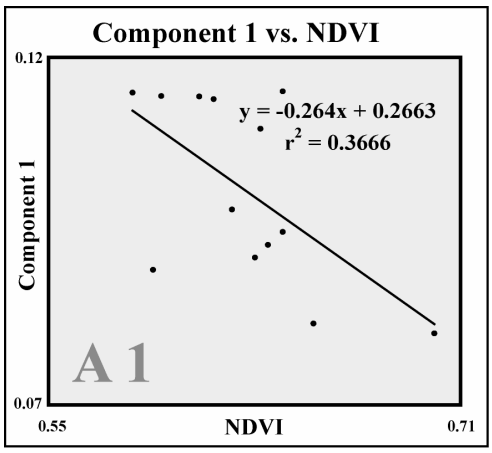

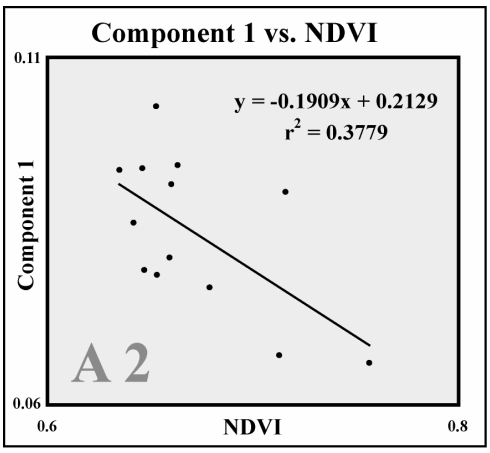

Figure 74 a / b. Correlation plots of PC 1 vs. NDVI: .a The left plot shows Evergreen – A1 .b The right plot shows Evergreen – A2

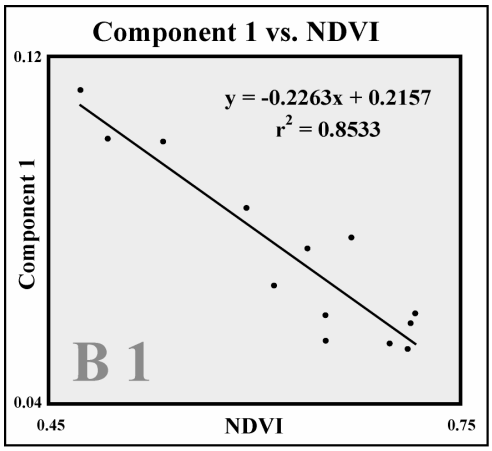

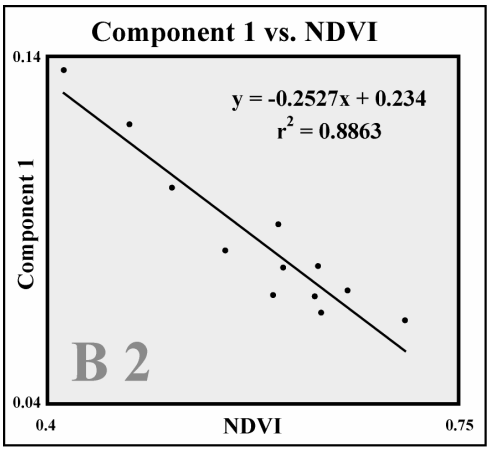

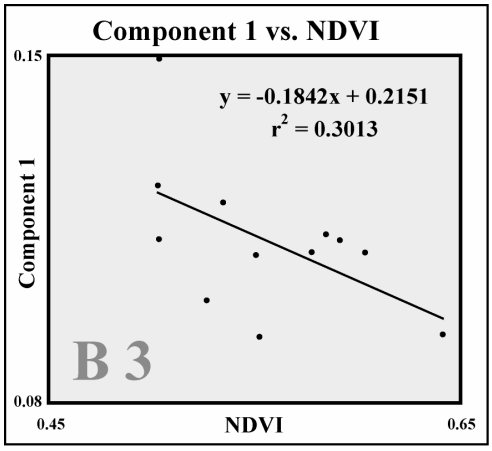

Figure 75 a / b / c. Correlation plots of PC 1 vs. NDVI: .a The top left plot shows Evergreen –B1 .b The top right plot shows Evergreen – B2 .c The bottom left plot shows Evergreen – B3

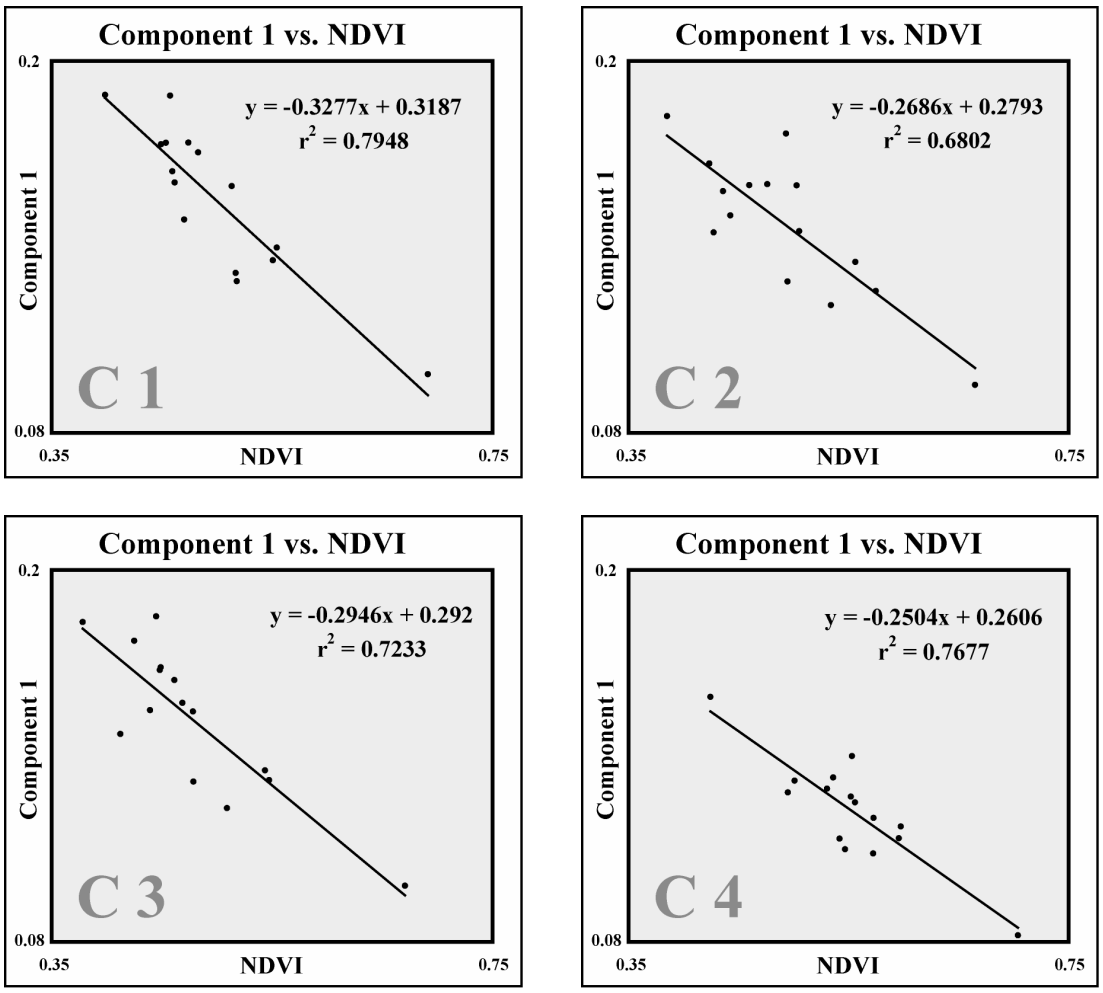

Figure 76 a / b / c / d. Correlation plots of PC 1 vs. NDVI: .a The top left plot shows Evergreen –C1 .b The top right plot shows Evergreen – C2 .c The bottom left plot shows Evergreen – C3 .d The bottom right plot shows Evergreen – C4

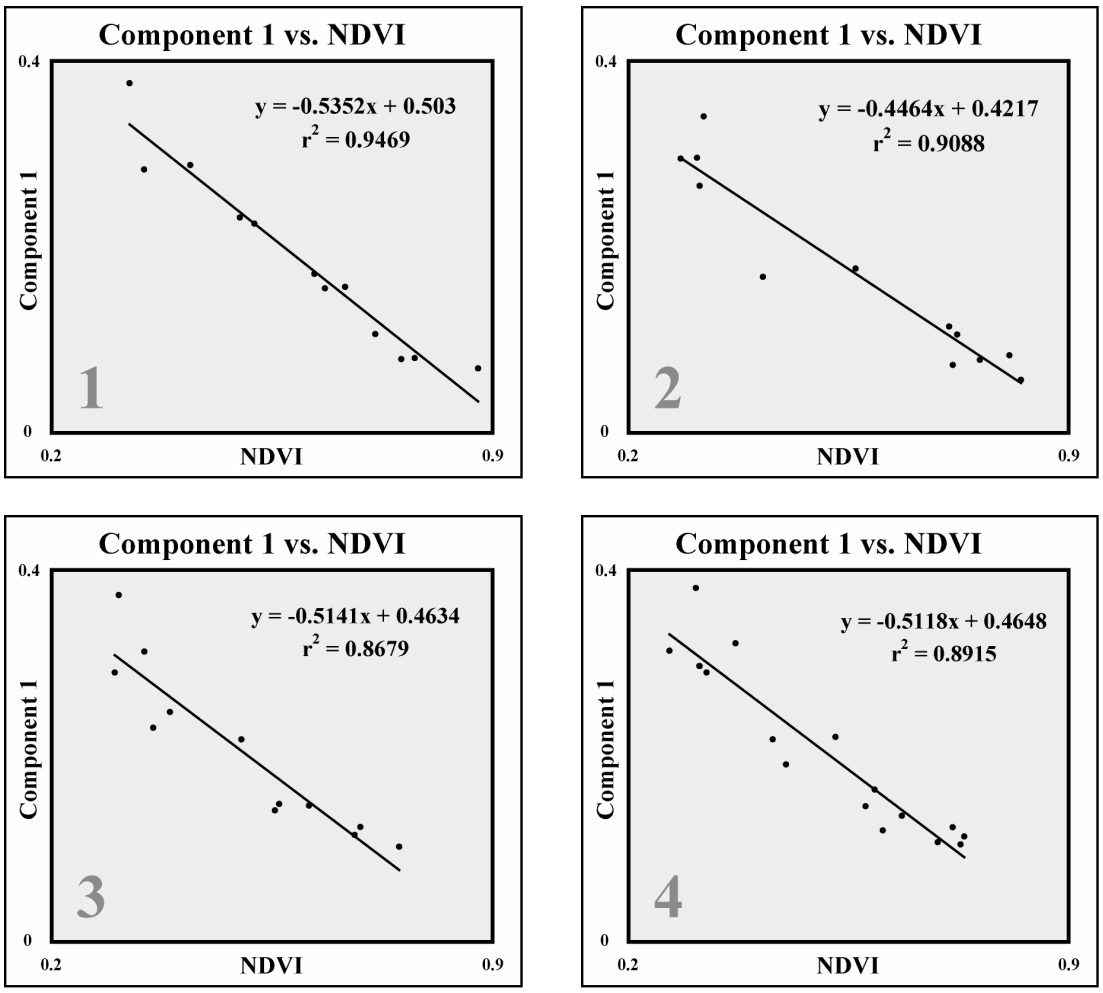

Figure 77 a / b / c / d. Correlation plots of PC 1 vs. NDVI: .a The top left plot shows Grassland sample 1 .b The top right plot shows Grassland sample 2 .c The bottom left plot shows Grassland sample 3 .d The bottom right plot shows Grassland sample 4

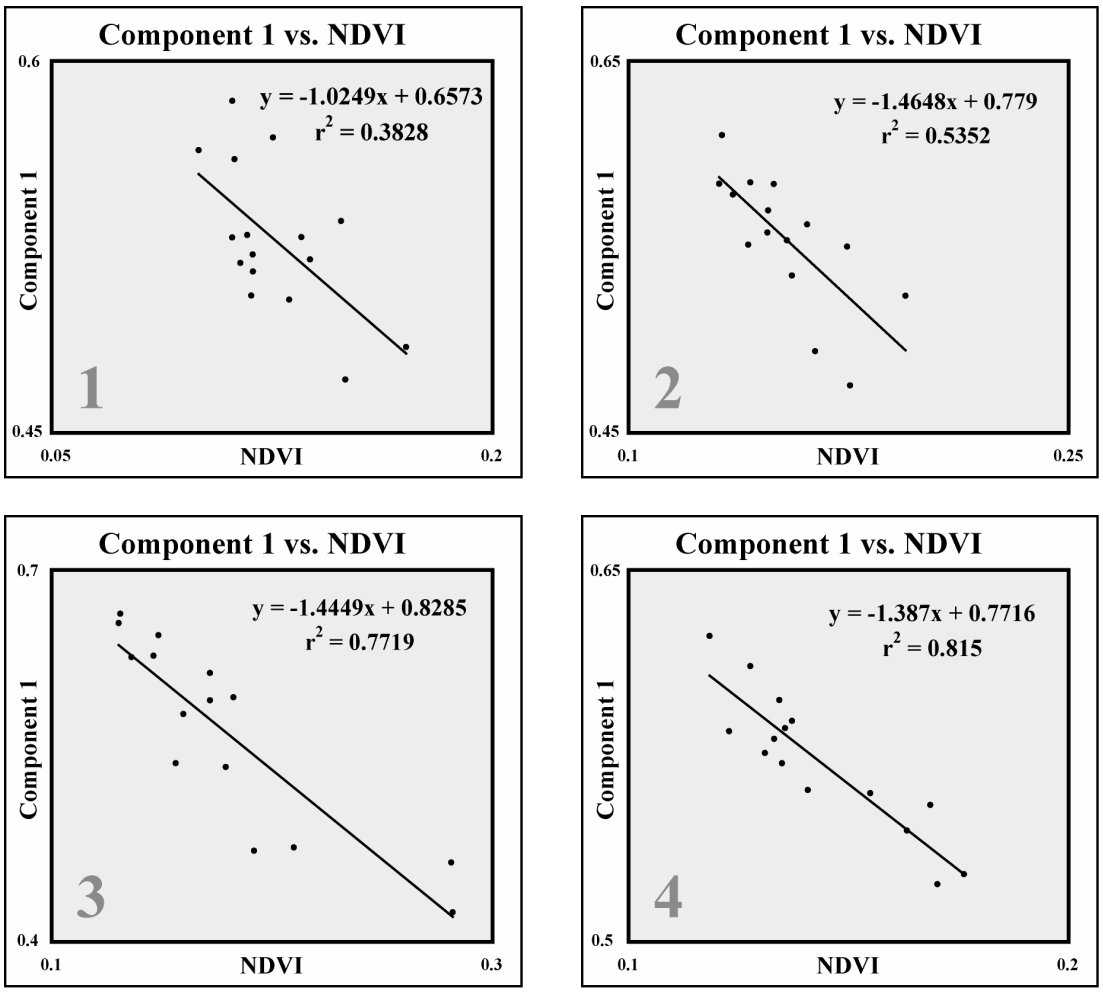

Figure 78 a / b c / d. Correlation plots of PC 1 vs. NDVI: .a The top left plot shows Shrubland sample 1 .b The top right plot shows Shrubland sample 2 .c The bottom left plot shows Shrubland sample 3 .d The bottom right plot shows Shrubland sample 4

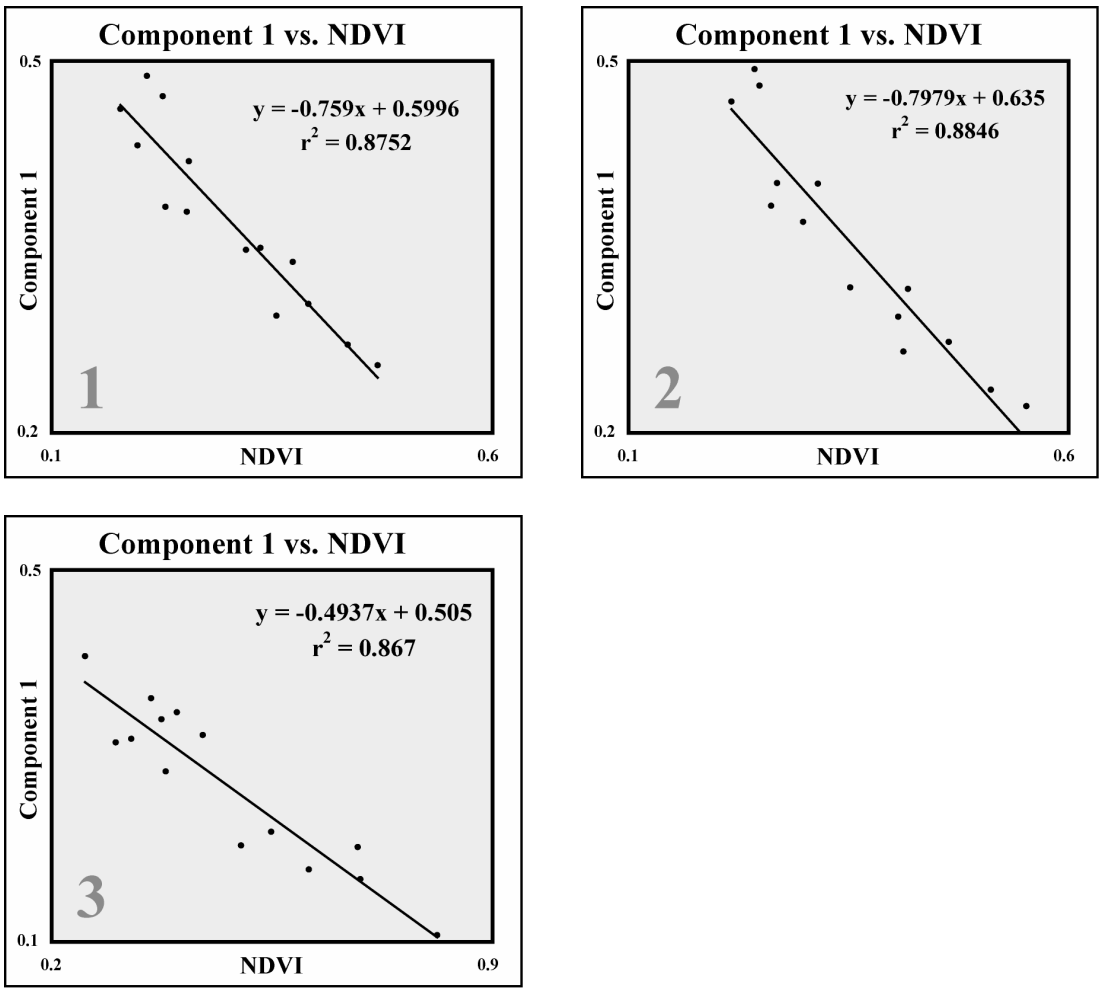

Figure 79 a / b / c. Correlation plots of PC 1 vs. NDVI: .a The top left plot shows Agriculture sample 1 .b The top right plot shows Agriculture sample 2 .c The bottom left plot shows Agriculture sample 3

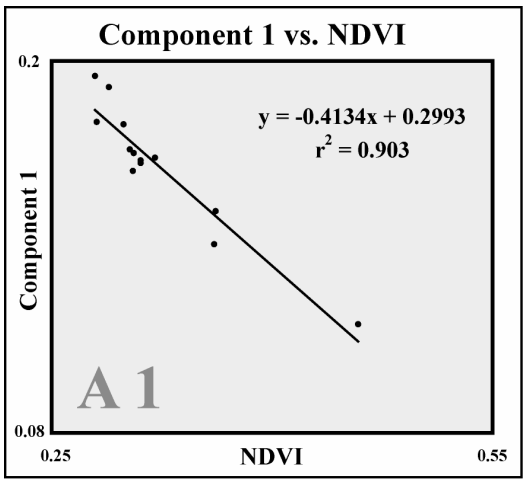

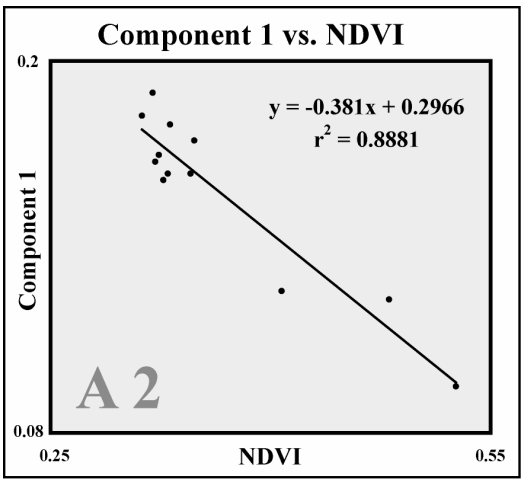

Figure 80 a / b. Correlation plots of PC 1 vs. NDVI: .a The left plot shows Western Juniper – A1 .b The right plot shows Western Juniper – A2

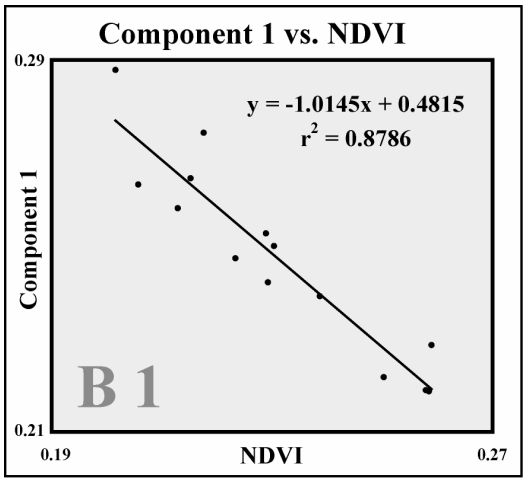

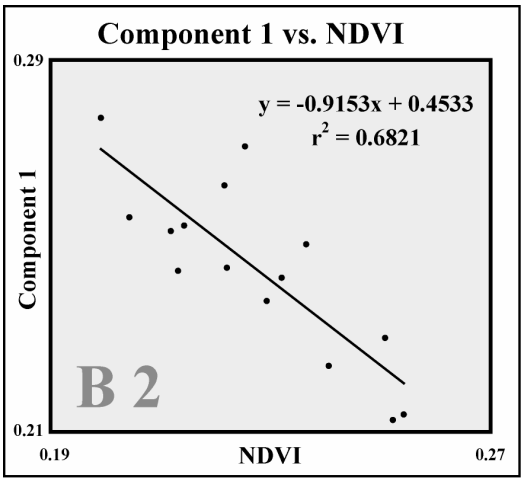

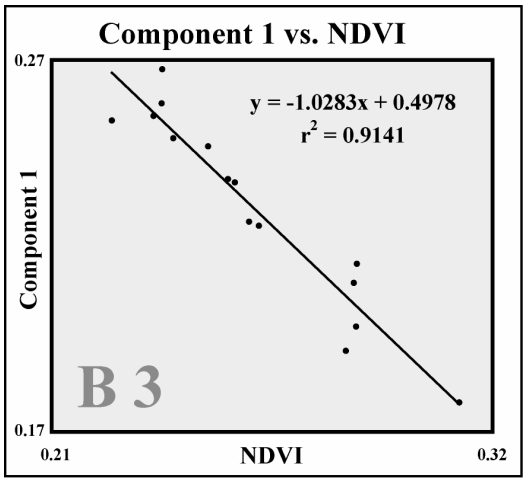

Figure 81 a / b / c. Correlation plots of PC 1 vs. NDVI: .a The top left plot shows Western Juniper – B1 .b The top right plot shows Western Juniper – B2 .c The bottom left plot shows Western Juniper – B3

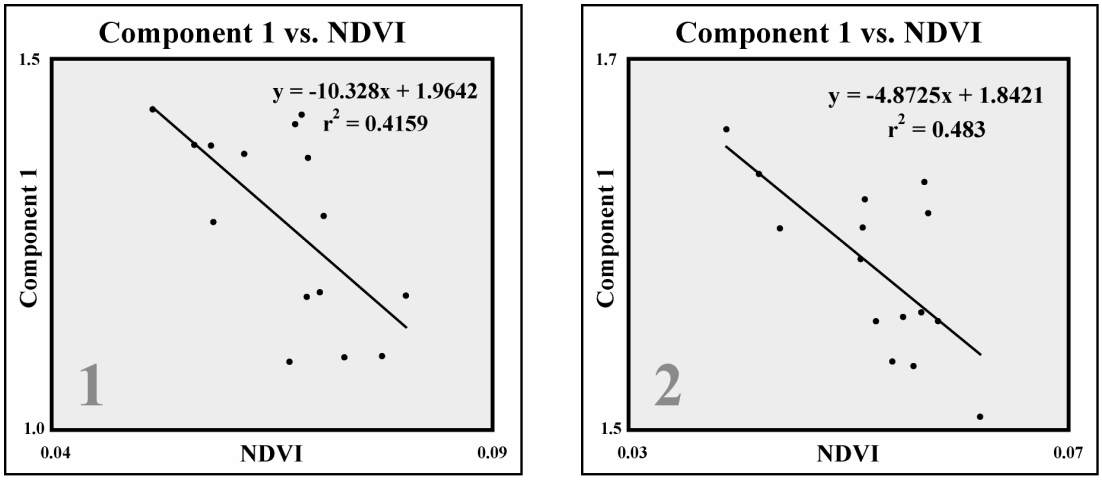

Figure 82 a / b. Correlation plots of PC 1 vs. NDVI: .a The left plot shows Gypsum Sands sample 1 .b The right plot shows Gypsum Sands sample 2

APPENDIX C: Correlation Plots: Principal Component 2 vs. Solar Zenith Angle

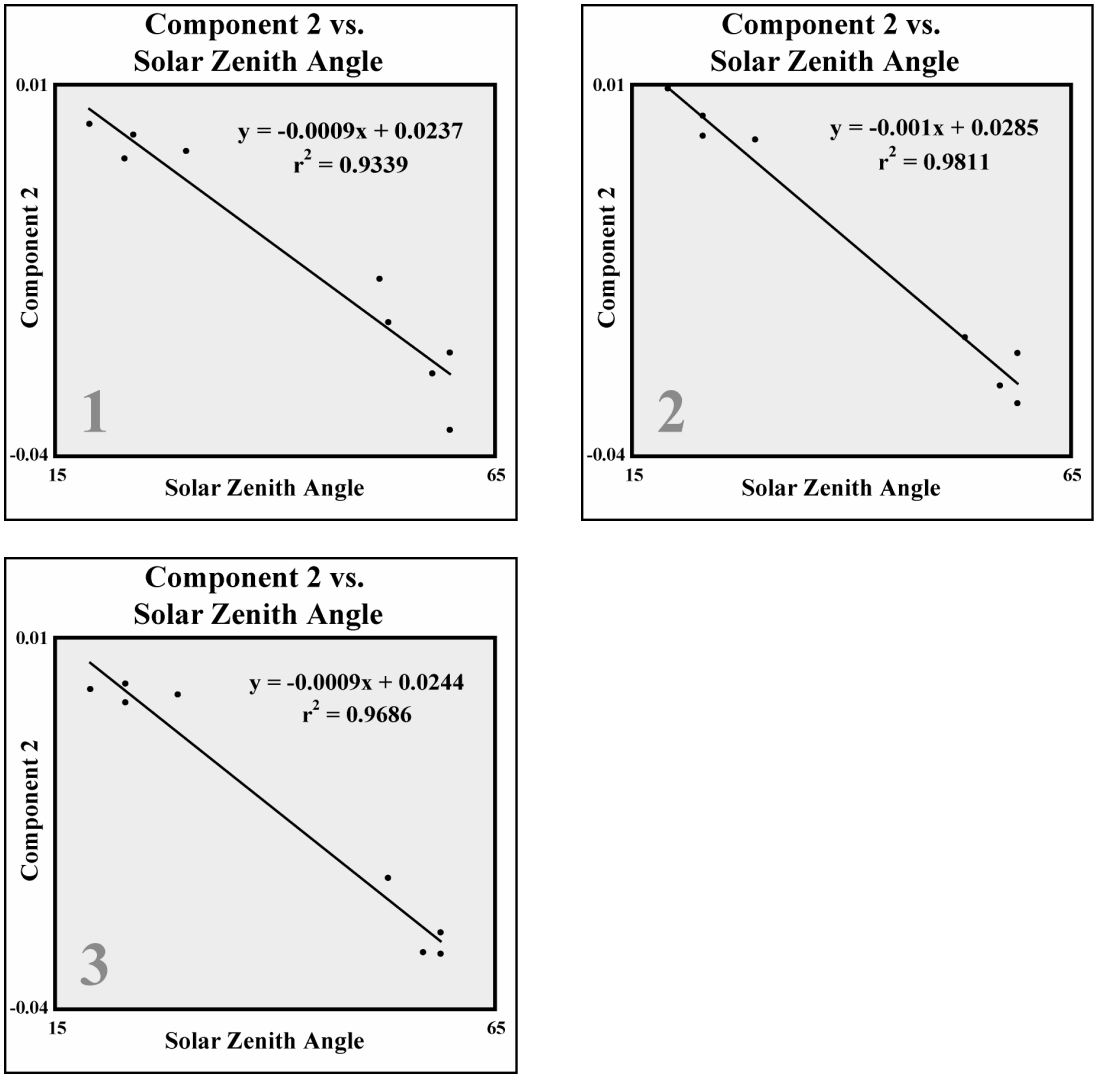

Figure 83 a / b / c. Correlation plots of PC 2 vs. solar zenith angle: .a The top left plot shows Deciduous sample 1 .b The top right plot shows Deciduous sample 2 .c The bottom left plot shows Deciduous sample 3

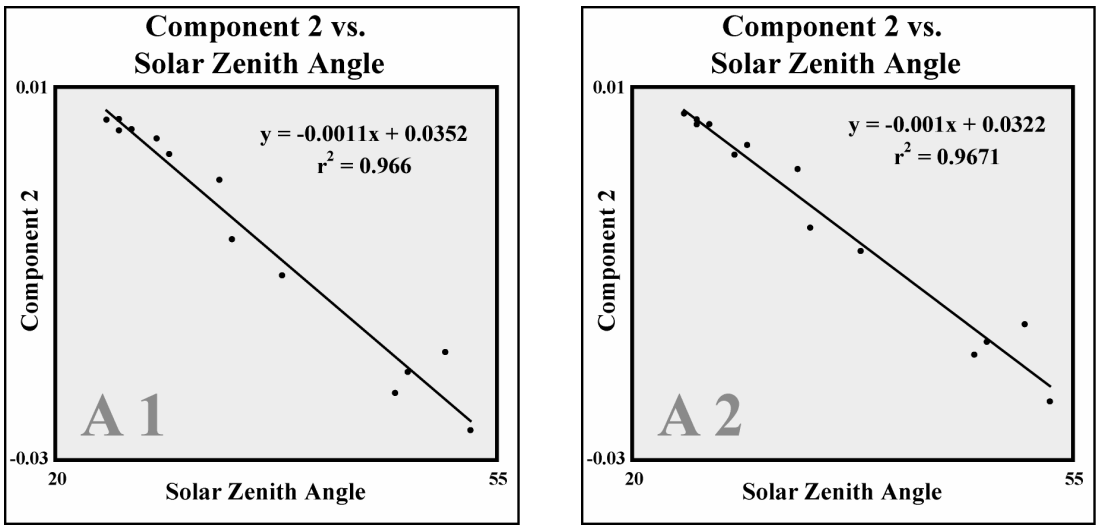

Figure 84 a / b. Correlation plots of PC 2 vs. solar zenith angle: .a The left plot shows Evergreen – A1 .b The right plot shows Evergreen – A2

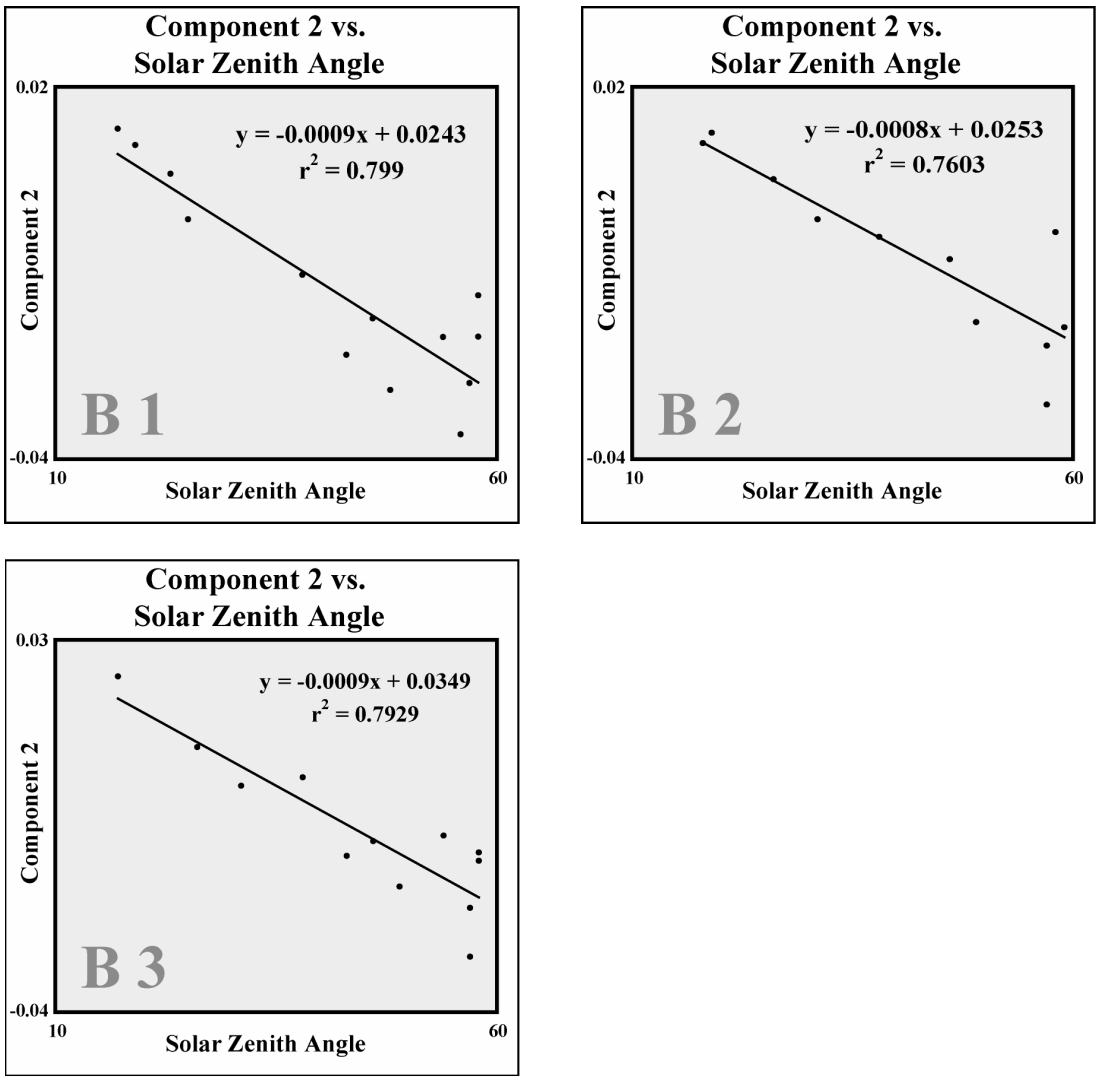

Figure 85 a / b / c. Correlation plots of PC 2 vs. solar zenith angle: .a The top left plot shows Evergreen – B1 .b The top right plot shows Evergreen – B2 .c The bottom left plot shows Evergreen – B3

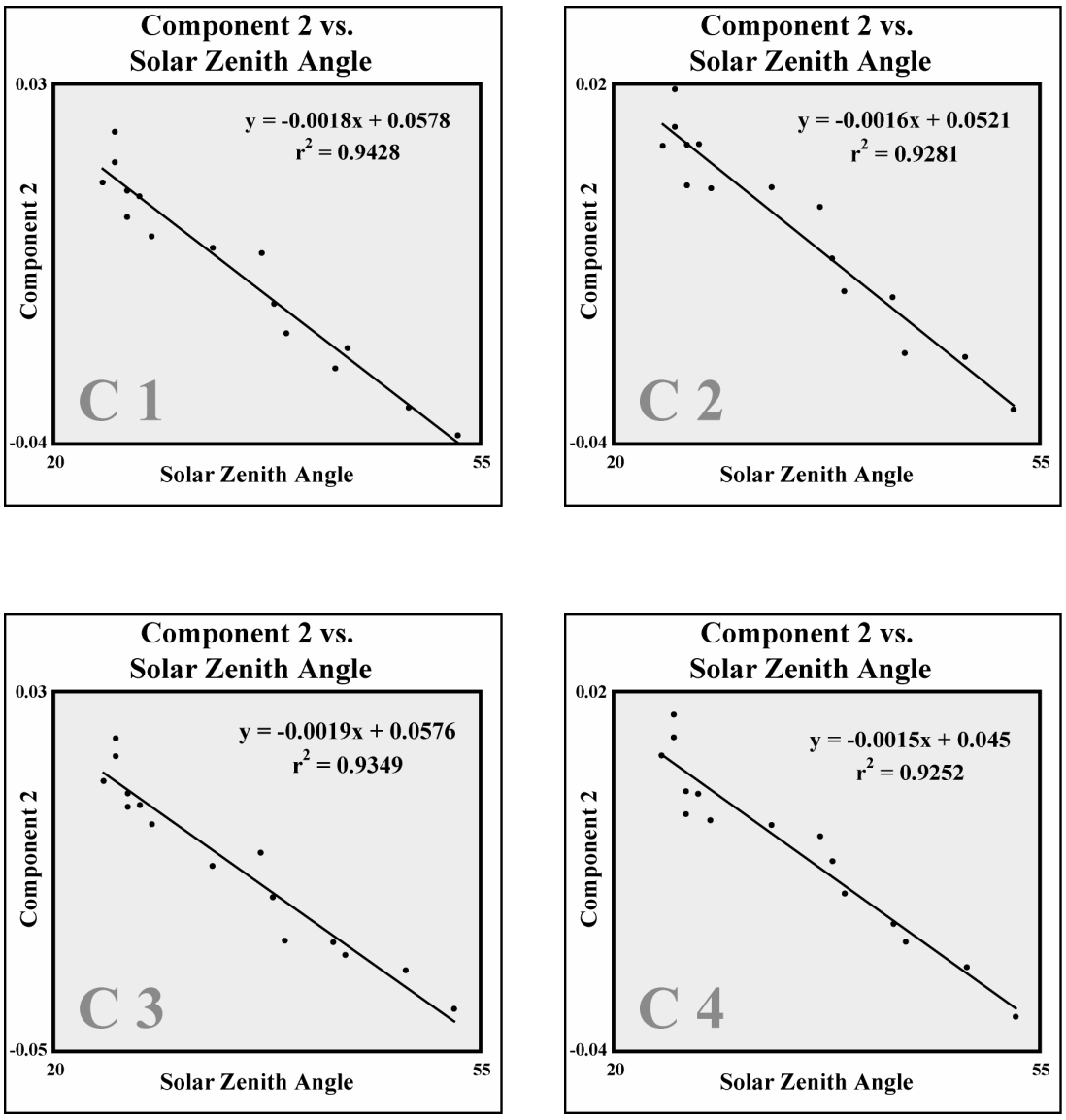

Figure 86 a / b / c / d. Correlation plots of PC 2 vs. solar zenith angle: .a The top left plot shows Evergreen – C1 .b The top right plot shows Evergreen – C2 .c The bottom left plot shows Evergreen – C3 .d The bottom right plot shows Evergreen – C4

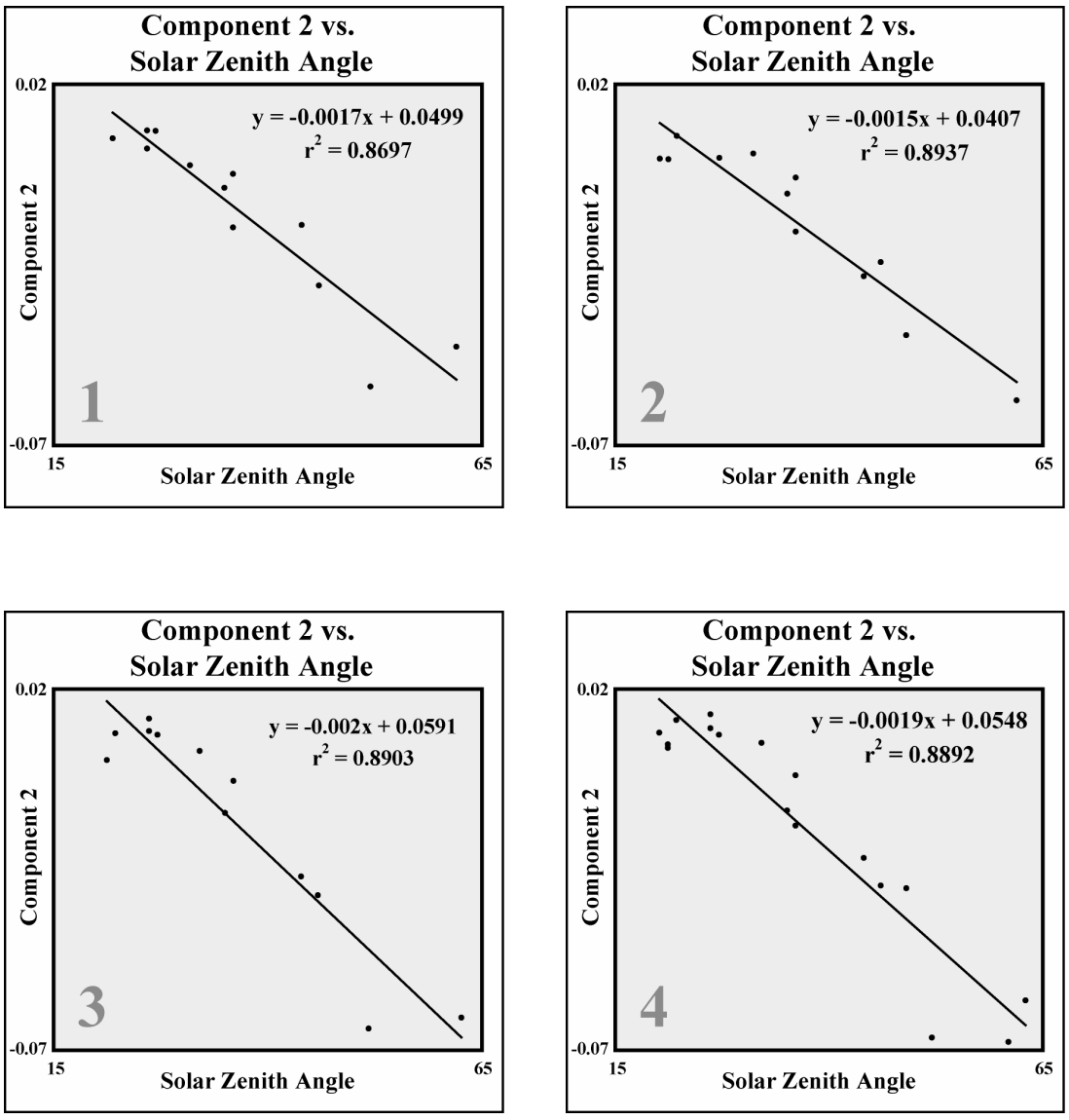

Figure 87 a / b / c / d. Correlation plots of PC 2 vs. solar zenith angle: .a The top left plot shows Grassland sample 1 .b The top right plot shows Grassland sample 2 .c The bottom left plot shows Grassland sample 3 .d The bottom right plot shows Grassland sample 4

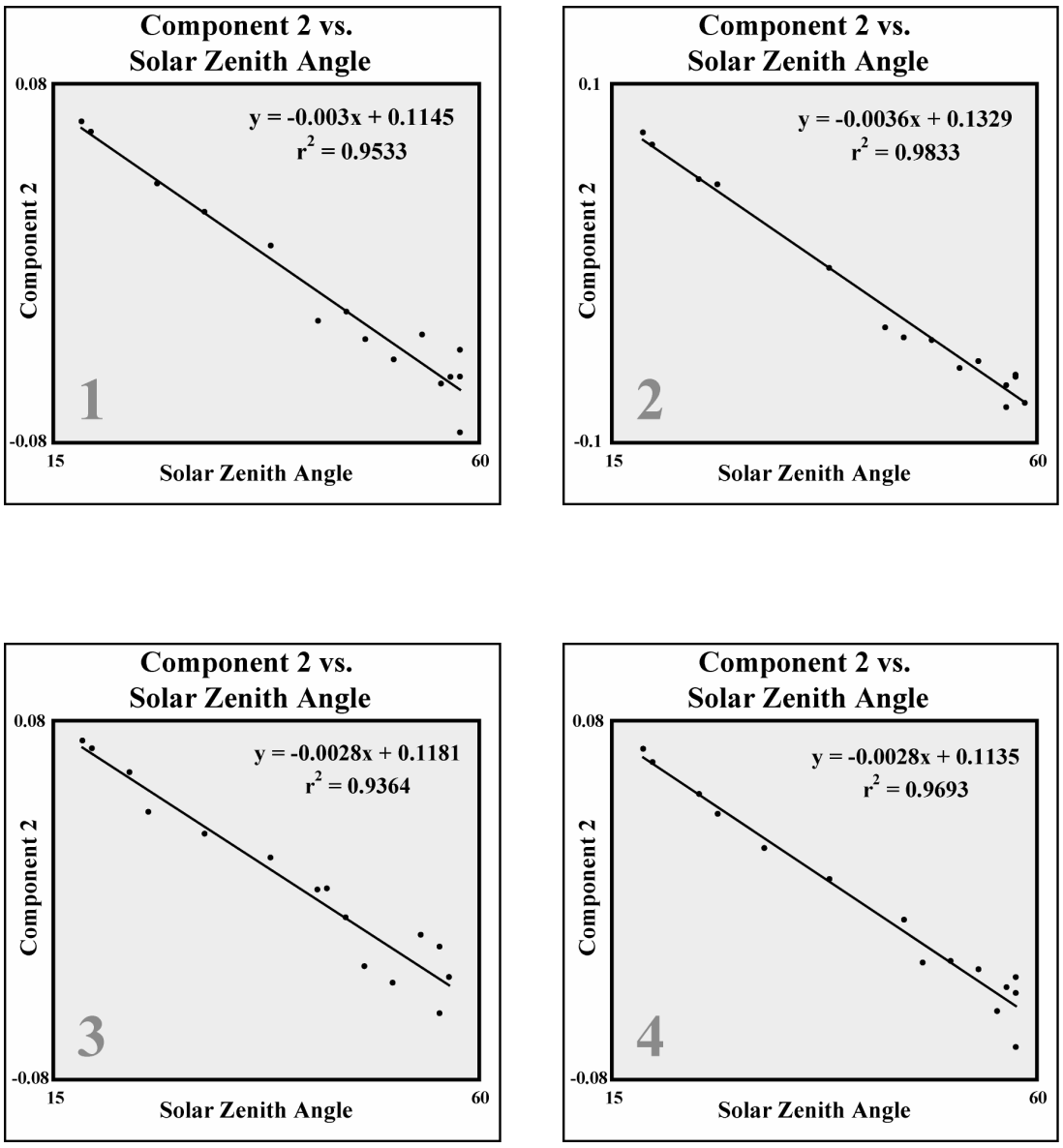

Figure 88 a / b / c / d. Correlation plots of PC 2 vs. solar zenith angle: .a The top left plot shows Shrubland sample 1 .b The top right plot shows Shrubland sample 2 .c The bottom left plot shows Shrubland sample 3 .d The bottom right plot shows Shrubland sample 4

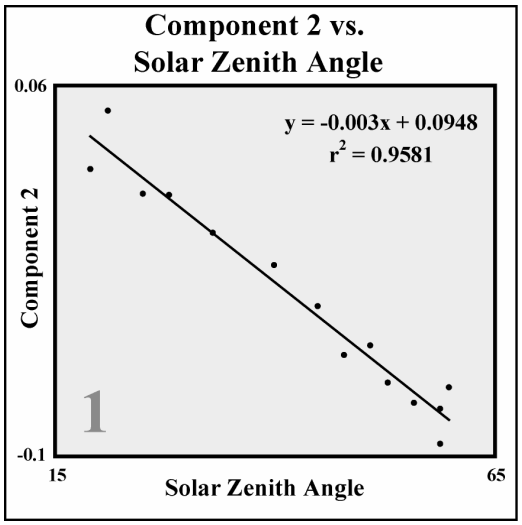

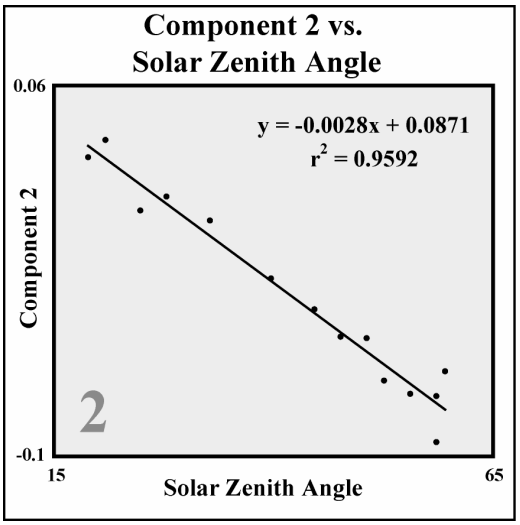

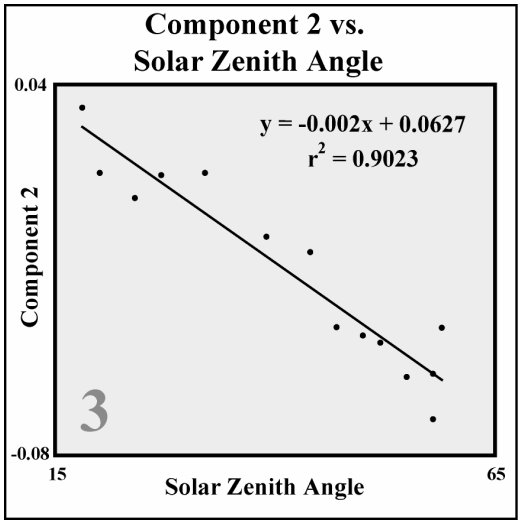

Figure 89 a / b / c. Correlation plots of PC 2 vs. solar zenith angle: .a The top left plot shows Agriculture sample 1 .b The top right plot shows Agriculture sample 2 .c The bottom left plot shows Agriculture sample 3

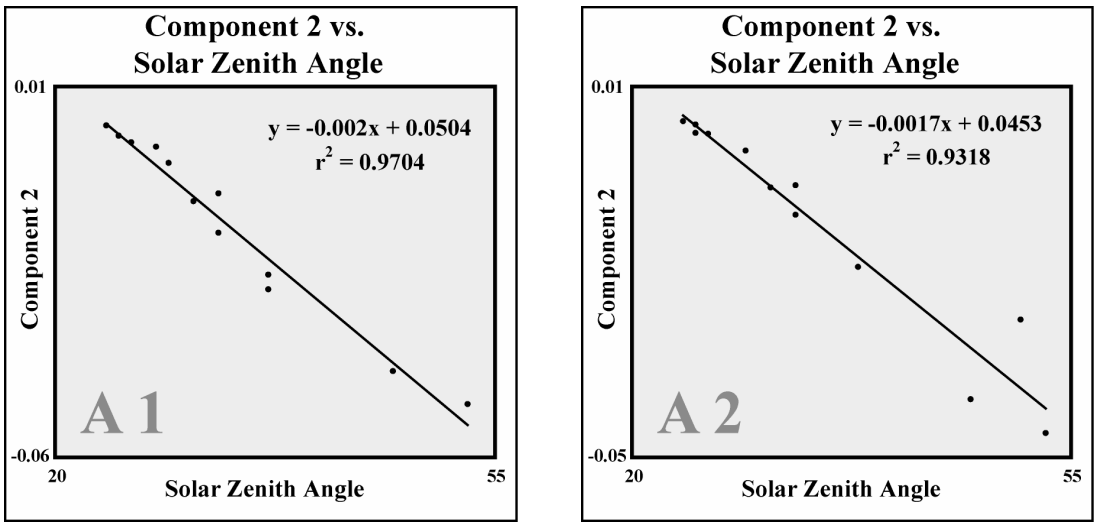

Figure 90 a / b. Correlation plots of PC 2 vs. solar zenith angle: .a The left plot shows Western Juniper – A1. .b The right plot shows Western Juniper – A2

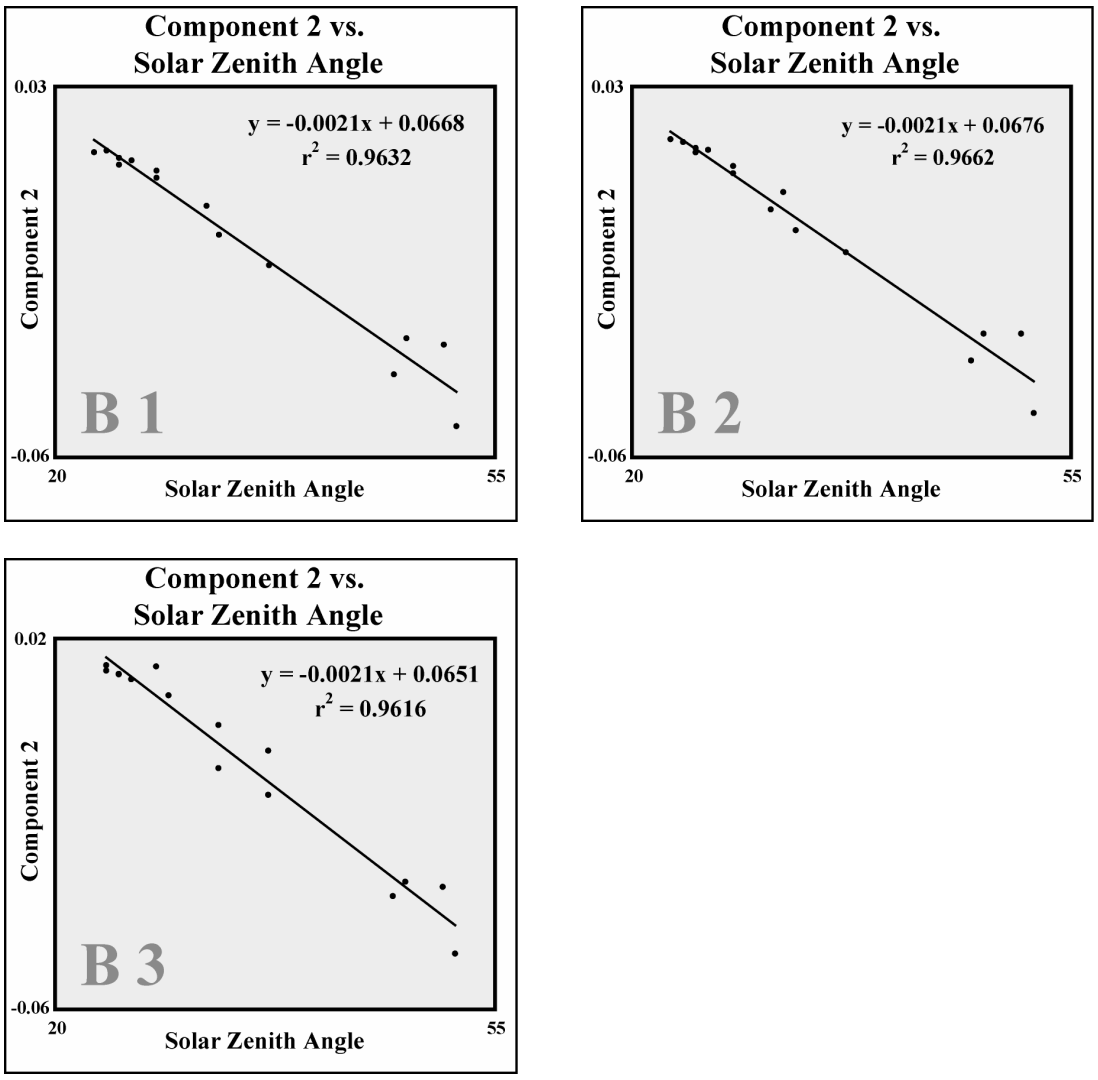

Figure 91 a / b / c. Correlation plots of PC 2 vs. solar zenith angle: .a The top left plot shows Western Juniper – B1 .b The top right plot shows Western Juniper – B2 .c The bottom left plot shows Western Juniper – B3

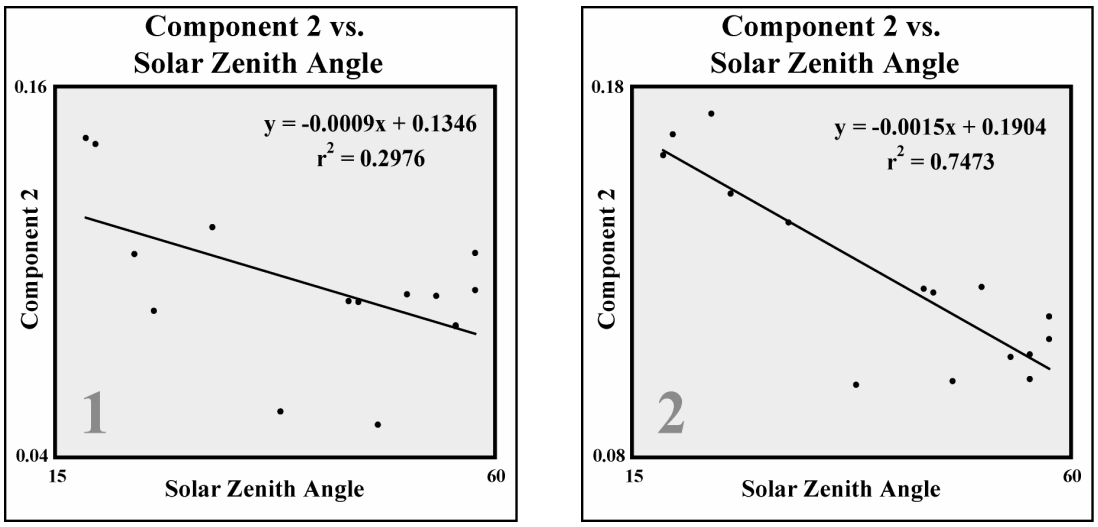

Figure 92 a / b. Correlation plots of PC 2 vs. solar zenith angle: .a the left plot shows Gypsum Sand sample 1 .b The right plot shows Gypsum Sand sample 2

APPENDIX D: Correlation Plots: Principal Component 2 vs. Relative Azimuth Angle

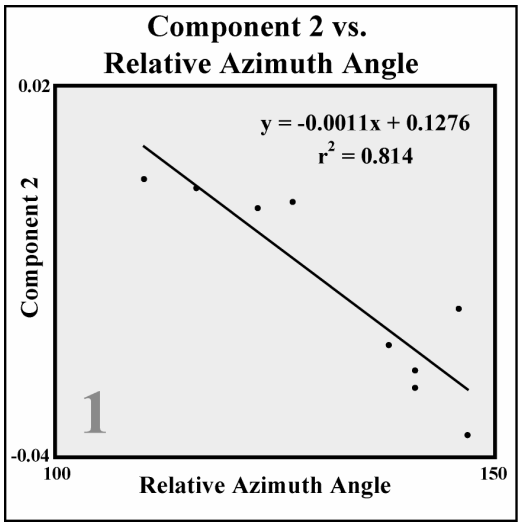

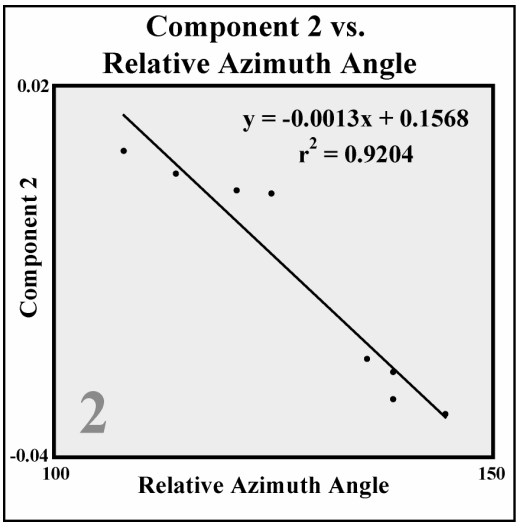

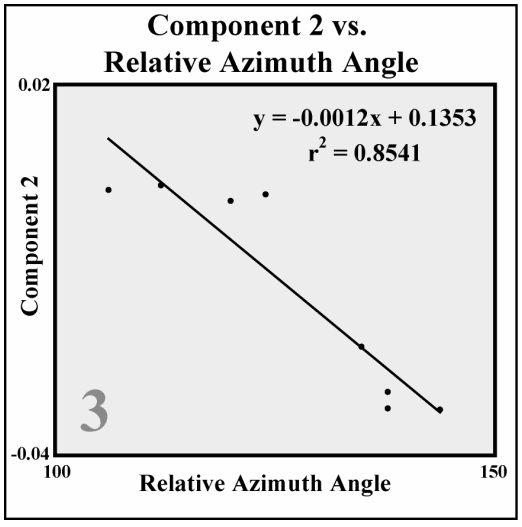

Figure 93 a / b / c. Correlation plots of PC 2 vs. relative solar azimuth angle: .a The top left plot shows Deciduous sample 1 .b The top right plot shows Deciduous sample 2 .c The bottom left plot shows Deciduous sample 3

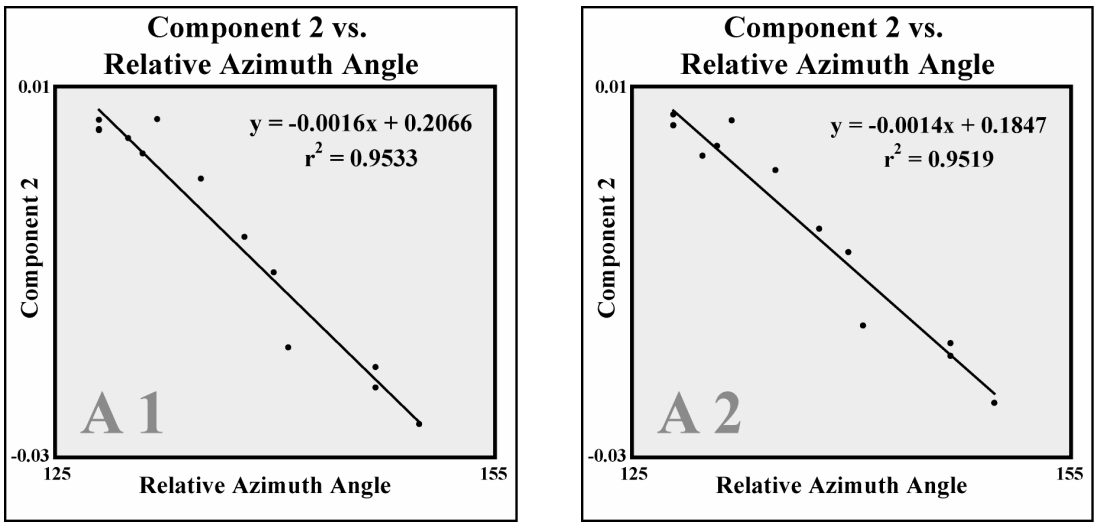

Figure 94 a / b. Correlation plots of PC 2 vs. relative solar azimuth angle: .a The left plot shows Evergreen – A1 .b The right plot shows Evergreen – A2

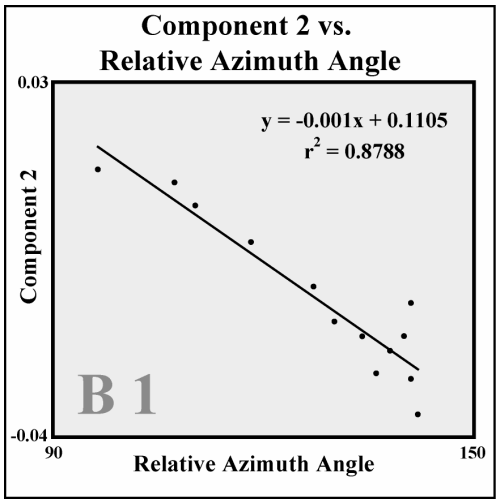

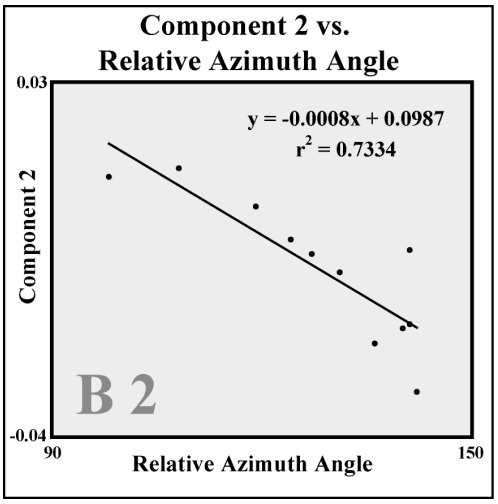

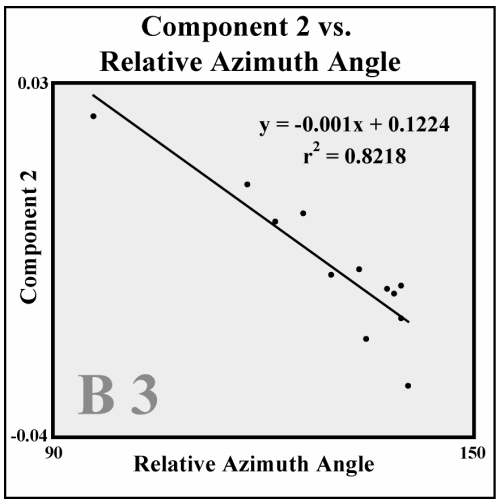

Figure 95 a / b / c. Correlation plots of PC 2 vs. relative solar azimuth angle: .a The top left plot shows Evergreen – B1 .b The top right plot shows Evergreen – B2 .c The bottom left plot shows Evergreen – B3

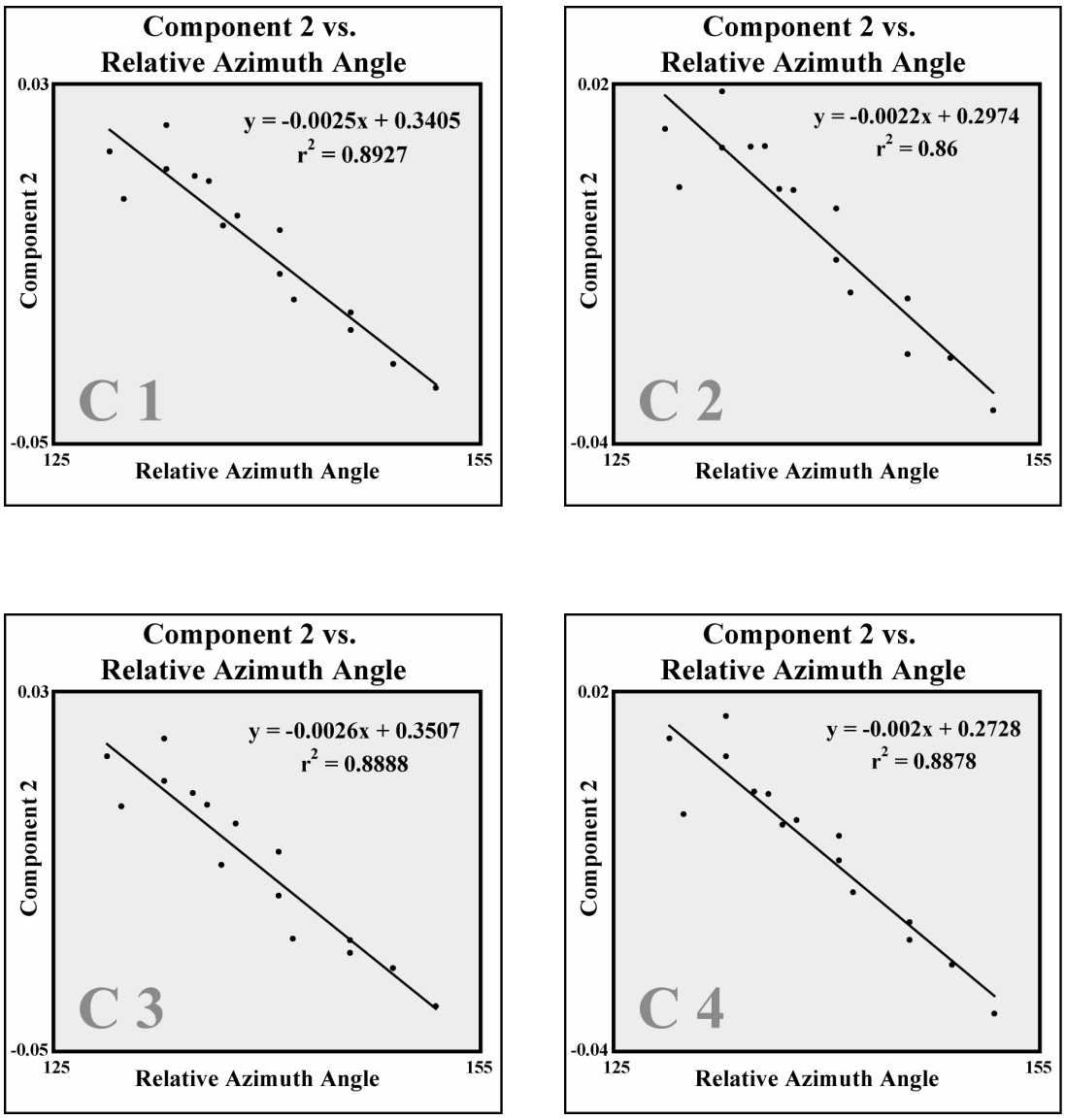

Figure 96 a / b / c / d. Correlation plots of PC 2 vs. relative solar azimuth angle: .a The top left plot shows Evergreen – C1 .b The top right plot shows Evergreen – C2 .c The bottom left plot shows Evergreen – C3 .d The bottom right plot shows Evergreen C4

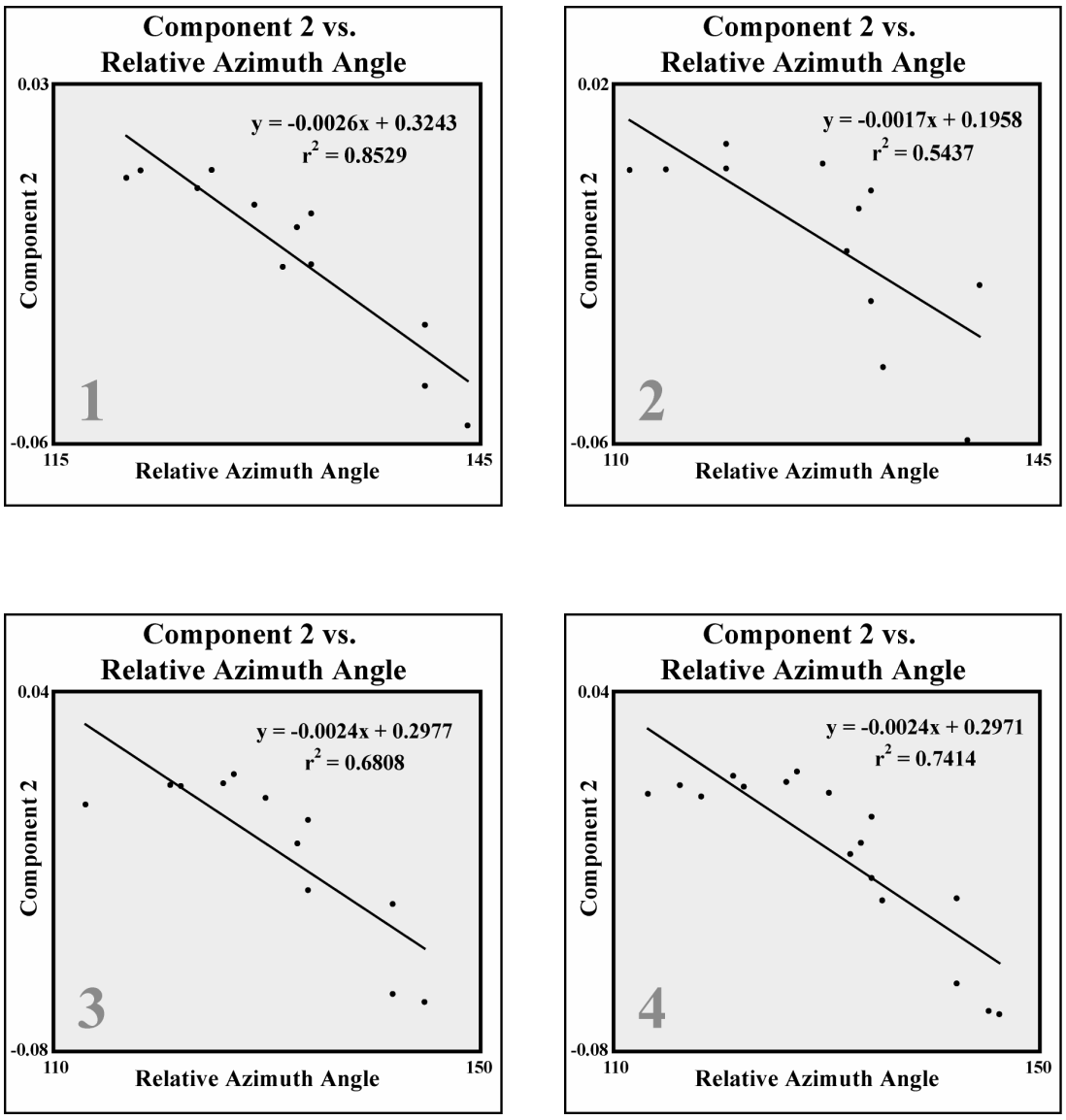

Figure 97 a / b / c / d. Correlation plots of PC 2 vs. relative solar azimuth angle: .a The top left plot shows Grassland sample 1 .b The top right plot shows Grassland sample 2 .c the bottom left plot shows Grassland sample 3 .d The bottom right plot shows Grassland sample 4

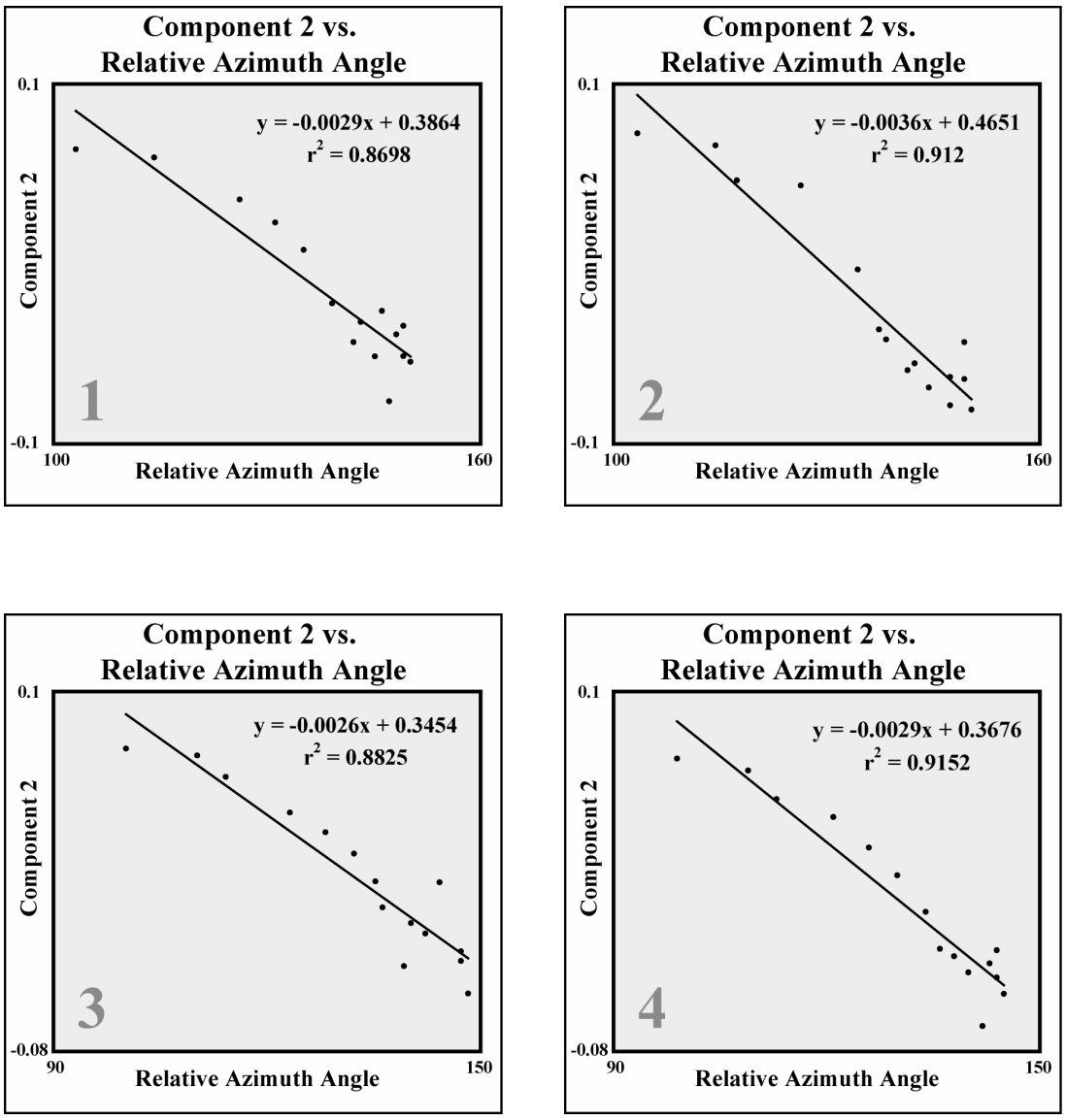

Figure 98 a / b / c / d. Correlation plots of PC 2 vs. relative solar azimuth angle: .a The top left plot shows Shrubland sample 1 .b The top right plot shows Shrubland sample 2 .c The bottom left plot shows Shrubland sample 3 .d The bottom right plot shows Shrubland sample 4

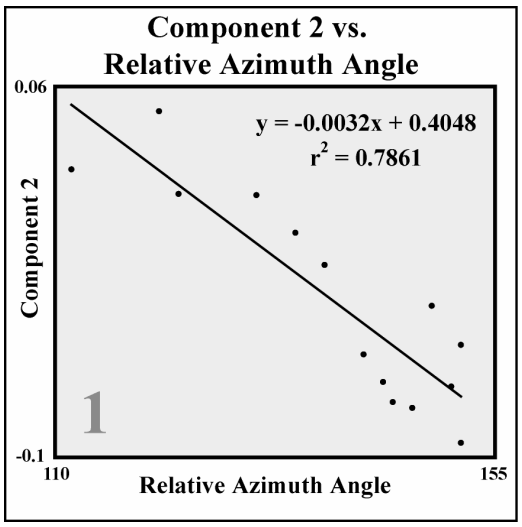

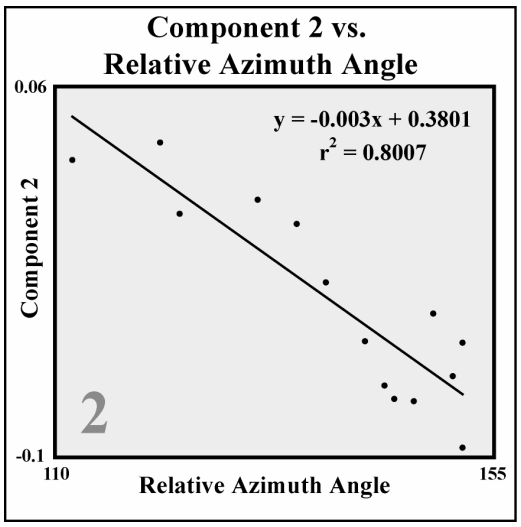

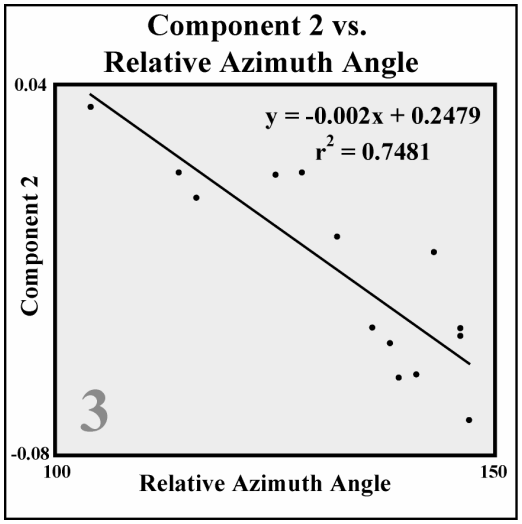

Figure 99 a / b / c. Correlation plots of PC 2 vs. relative solar azimuth angle: .a The top left plot shows Agriculture sample 1 .b The top right plot shows Agriculture sample 2 .c The bottom left plot shows Agriculture sample 3

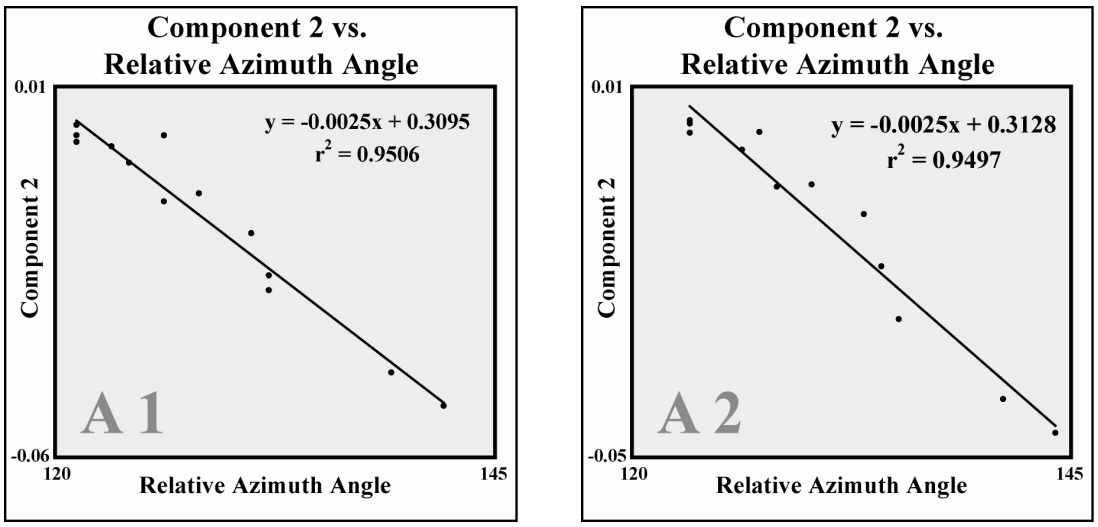

Figure 100 a / b. Correlation plots of PC 2 vs. relative solar azimuth angle: .a The left plot shows Western Juniper – A1 .b The right plot shows Western Juniper – A2

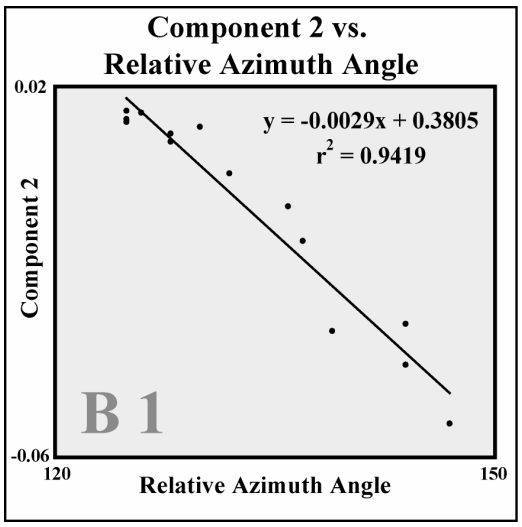

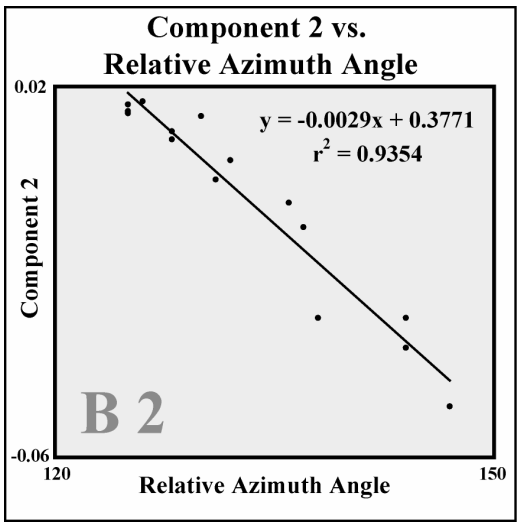

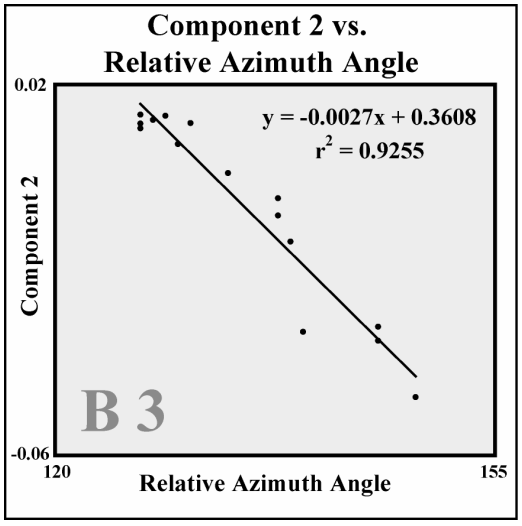

Figure 101 a / b / c. Correlation plots of PC 2 vs. relative solar azimuth angle: .a The top left plot shows Western Juniper – B1 .b The top right plot shows Western Juniper – B2 .c The bottom left plot shows Western Juniper – B3

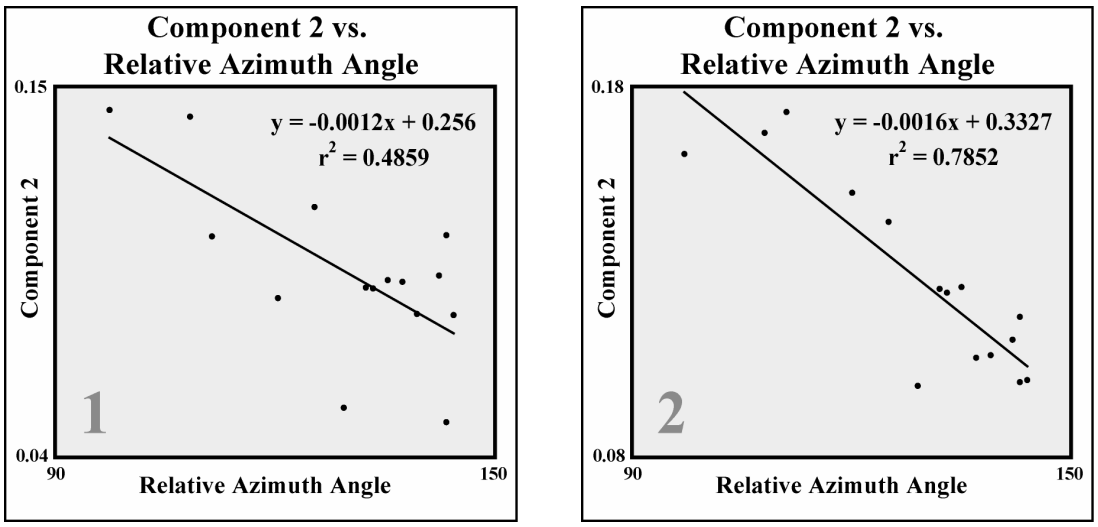

Figure 102 a / b. Correlation plots of PC 2 vs. relative solar azimuth angle: .a The left plot shows Gypsum Sand sample 1 .b The right plot shows Gypsum Sand sample 2

APPENDIX E: Tables

Table 12. 1992 NLCD land cover classifications

CLASS NUMBER	CLASS NAME	CLASS NUMBER	CLASS NAME
11	Open Water	51	Shrubland
12	Perennial Ice / Snow	61	Orchards / Vineyards
21	Low Intensity Residential	71	Grasslands / Herbaceous
22	High Intensity Residential	81	Pasture / Hay
23	Commercial / Industrial / Transportation	82	Row Crops
31	Bare Rock / Sand / Clay	83	Small Grains
32	Quarries / Strip Mines, Gravel Pits	84	Fallow
33	Transitional	85	Urban / Recreational Grasses
41	Deciduous Forest	91	Woody Wetlands
42	Evergreen Forest	92	Emergent Herbaceous Wetlands
43	Mixed Forest		

Table 13. Coefficients of rotation for the MISR 'M-Cone' PCA

	PC 1	PC 2	PC 3	PC 4	PC 5	PC 6	PC 7
Cf	0.959388	0.170115	0.211747	0.069790	0.031056	0.000756	0.002979
Bf	0.970334	0.206714	0.092332	-0.052116	-0.064322	-0.019085	0.007761
Af	0.972458	0.221522	-0.024749	-0.037919	0.021436	0.041740	-0.031972
An	0.970978	0.207378	-0.105795	-0.010254	0.038324	-0.013387	0.036990
Aa	0.992456	0.023865	-0.102397	0.045973	-0.017704	-0.028118	-0.028937
Ba	0.975896	-0.208664	-0.031666	0.026381	-0.031524	0.033100	0.018890
Ca	0.936879	-0.343856	0.043407	-0.034385	0.026766	-0.015209	-0.006158